OUKA
The University of Osaka
Institutional Knowledge Archive

Title	Study on spin-related transport in few-electron lateral quantum dots for the photon-spin interface using a (110) GaAs quantum well
Author(s)	中川, 智裕
Citation	大阪大学, 2023, 博士論文
Version Type	VoR
URL	https://doi.org/10.18910/92155
rights	
Note	

The University of Osaka Institutional Knowledge Archive : OUKA

https://ir.library.osaka-u.ac.jp/

The University of Osaka

Doctoral Dissertation

Study on spin-related transport in few-electron lateral quantum dots for the photon-spin interface using a (110) GaAs quantum well

(110)GaAs量子井戸を用いた光子-スピンインターフェースに向けた少数電子横型量子ドットにおけるスピンに関係した伝導の研究

Tomohiro Nakagawa

Graduate School of Science,
Osaka University

Supervisor: Professor Akira Oiwa

February 2023

Abstract

With the progress of micro-fabrication and measurement technologies and the increased activity of quantum computers in the past few years, the technologies of accurate controls and precise detections of the transport and spin states of a few electrons in semiconductor quantum systems at low temperature have been developed considerably. Lateral quantum dots (QDs) that are formed in a zero-dimensional confinement induced by a surface gate voltage in a two-dimensional electron layer at a hetero-interface have attracted interests as a candidate for a qubit. In addition, the detection of the spin of a single photo-electron generated by a single photon illumination into a GaAs QD and demonstration of the quantum state conversion from a single photon polarization state to a single electron spin states in the GaAs QD have attracted much attention to a quantum interface between single photons and single electron spins. This technology has been developing by combining nano-photonics with quantum transports to contribute to the quantum repeaters for long distance quantum communication.

In the conventional studies on the quantum state conversion, lateral QDs formed in quantum wells (QWs) grown on a (001) GaAs substrate have been used. In this case, the excitation of a light hole state with a low transition probability is needed for the quantum state conversion. On the contrary, in (110) substrate, the quantum state conversion using a heavy hole state with a transition probability higher than that the light hole state is expected to be possible, making the QD formed in a (110) QW suitable materials system for the quantum state conversion. However, while there are many works on the spin relaxation mechanism in (110) QWs, few works on the formation of gate-defined quantum devices including lateral QDs have been reported and the spin physics originated in the unique spin-orbit interaction on the (110) plane have not yet been well studied.

In this work, we design GaAs QWs on a (110) substrates and gate-defined lateral QD structures, then fabricate the QD devices. Finally, in the transport measurements at low temperature, we succeed, for the first time, to form QDs in the (110) QW

substrates. Moreover, we reach to a few electron regime in the QDs and observe Pauli spin blockade in a two electron region. From the QD current behaviors in the Pauli spin blockade region, we estimate the in-plane g-factors of electrons in the QDs. These results are important achievements for the quantum state conversion from single photon polarization states to single electron spin states in QDs. In addition, toward development of quantum state conversion and its application to quantum repeaters, a precise imaging method based on a scanning optical fiber by piezo-stage at low temperature has been established as a sophisticated method of precise photon illumination to a QD device at low temperatures as a fundamental technology for quantum state conversion experiments. The results presented in this thesis suggest a way to realize efficient quantum repeaters and a technical breakthrough for the advanced experiments of the quantum state conversion from a single photon polarization state to a single electron spin state in the QD.

Acknowledgments

Any results presented in this Ph.D. dissertation would never be provided without positive corporation and warm encouragement of many people I have related through my master and doctor courses.

First and foremost, I would like to express my deep gratitude to my supervisor, Prof. Akira Oiwa. When I joined the Oiwa group, it was the second year since the laboratory had been renewed. There were no seniors who address on the similar research theme with mine. Under such situations, however, Prof. Oiwa not only gave me good advice but also visited the experiment room and engaged in the experiments together. I remember repeating the discussion using the white-board there. Invaluable experiences to enrich my life more afterward had been given through the research days at the laboratory. I can't help but feel grateful for his kind words and his help with me.

Prof. Haruki Kiyama taught us the fundamental knowledge about this field. He made sharp comments on the experimental results and my considerations at the weekly meetings and so on. He also made a great contribution to the setting up of our experiment environment.

After Prof. Fujita Takafumi joined in the Oiwa laboratory, my experiments greatly accelerated. With his sophisticated research experiences and overflowing ideas, he supported strongly in constructing the experiment equipment leading to the results in this paper. I cannot help but feel grateful for his kind words and his help with me in many cases.

Dr. Yuji Sakai taught me a lot of things as a laser expert and a familiar researcher working with me, and showed me what I should learn. I felt very reassuring as someone like a senior who I could easily consult in the student room with something about

the research life.

Prof. Shigehiko Hasegawa had me deepen the insight on papers by asking me some questions at the Journal Club, and Dr. Hiroki Shioya always gave me positive words.

Interacting with many colleagues had been a great support in continuing my research. Especially, Dr. Rio Fukai was a special supportive colleague in my research life. What impressed me most was the discussion about the construction of the complicated measurement system and the sensitive lithography conditions. His determination and words to work hard with me to obtain Ph.D remain in my mind.

Dr. Julian Ritzmann, Prof. Arne Ludwig and Prof. Andreas D. Wick in Ruhr University Bochum made great efforts on the deposition process of our substrates. With respecting on our ideas, they found the growth conditions even on a specific crystal orientation different from the conventional one, and provided us good quality quantum well substrates, which let us operate the (110) quantum dots.

During the short stay at RIKEN, Prof. Tomohiro Ohtsuka and Dr. Takashi Nakajima taught me a lot of important knowledge while preparing for the measuremnets, and their experiment setup there stimulated me to come up with the idea to establish the measurement system shown in this paper. I also would like to thanks to Prof. Seigo Tarucha for receiving me in the laboratory.

While I stayed at NRC in Canada, I was able to spend research days happily because many people treated me very kindly. Dr. Louis Gaudreau and Dr. Sergei Studenikin gave me practical measurement knowhow and discussed the strategy of my experiments with me. Mr. Jason Phoenix contributed mostly to the scanning measurements by telling me the measurement program and the setup. I was moved with seeing the very clear scanning images with him at midnight. Dr. David Guy Austing not only gave me excellent research advice, but also helped me with my life in Canada in general. Daily lunch with him energized my mind. I greatly appreciate kindness by Dr. Andrew Sachrajda who let me spend the wonderful time at NRC.

Last, but not least, I would like to dedicate this work to my family. Here again, I would like to thank them all.

February 2023

Tomohiro Nakagawa

Contents

Abstract i

Acknowledgments iii

Intoroduction 1

1 Background 7

1.1 Physics of Two Dimensional Semiconductors 7

1.1.1 Semiconductor physics 7

1.1.2 Two-dimensional Electron Gas 10

1.1.3 Quantum Hall effect 12

1.2 Spin Orbit Interaction 15

1.2.1 Spin Relaxation Mechanism 15

1.3 Physics of Zero-dimensional Electrons 19

1.3.1 Single Quantum Dot 21

1.3.2 Double Quantum Dot 22

1.4 Pauli Spin Blockade 26

1.5 Quantum State Conversion 32

1.5.1 Theory of Quantum State Conversion using Quantum Well Substrate 32

1.5.2 Quantum State Transfer in an Ensemble 34

1.5.3 Single Photon and Single Electron Spin Interface 36

2 (110) Quantum Well Design and Characterizations 38

2.1 Quantum State Conversion using (110) substrates 38

2.2 Substrate Layer Design 42
2.3 Evaluation by Quantum Hall Effect 43

3 Quantum Dot Formation in (110) quantum wells 45
3.1 Device Design and Fabrication 47
3.2 Measurement Setup 49
3.2.1 Cold Finger 49
3.2.2 Low Pass Filter 51
3.3 QD Formation in (110) QWs 52
3.3.1 Quantum Dot Operation in the Many-Electron Region 53
3.3.2 QD Operation in the Few-electron Region 55
3.3.3 "Quasi" DQD operation and Real-Time Measurement 59

4 Pauli Spin Blockade and g-factor Estimation 62
4.1 New Design of the Electrode Patterns of QD Devices 63
4.1.1 Device Structures for in-plane Anisotropy Studies 64
4.2 Measurement Setup 69
4.2.1 Dilution Refrigerator Setup 69
4.2.2 Sample Stage Setup 70
4.3 Pauli Spin Blockade in Many-electron Region 72
4.4 Pauli Spin Blockade in a Few Electron Region 76
4.4.1 g-factor Evaluation in a Few Electron Regime 79

5 Optical Fiber Scanning Over the Device in Dilution Refrigerator 84
5.1 Setup 85
5.1.1 Sample Holder 85
5.1.2 Optical Setup 86
5.1.3 Photo-mask and Aperture 87
5.1.4 Measurement Procedure 89
5.2 Scanning at Room Temperature 90
5.2.1 Imaging by Different Wavelength 90
5.2.2 Imaging by Reflection and Photo-induced Current 92
5.3 Scanning at Low Temperature 95

5.3.1 Finding the Target Area on the Sample 96
5.3.2 Device Pattern Focusing 97
5.3.3 High Resolution Scan of the Aperture 99

6 Summary **101**

Intoroduction

The concept of superlattice proposed by Esaki and Tsu at IBM in 1970 ' s [43] has led technologies to detect and control charge and spin of single electrons in quantum devices along with the development in semiconductor microfabrication technologies. In contrast to the development of the present semiconductor electronic devices that have been increasing functionality by advancing the integration of devices for a few decades, this device research actively utilizes the advantages of quantum mechanical properties that remarkably emerge at nano-scale.

On the other hand, as a next-generation communication technology which takes the advantage of the quantum mechanical properties of single photons, quantum (cryptographic) communication is also under development and is close to practical use. However, as with the conventional optical communication through optical fiber networks, there is a problem that the communication distance is limited less than 100 km due to losses of photons (light) in the optical fiber. Technical breakthrough for long-distance quantum communication and for construction of global quantum networks is an urgent issue. Quantum repeaters have been proposed to extend the transmission distance of quantum information. In this scheme, the transmission distance of each photon is reduced to approximately 100 km or less by dividing the total distance between the sender and receiver into multiple nodes. By performing entanglement distribution between the nodes, repeatedly performing Bell measurements, and thus applying entanglement swapping to the transmitted entangled states at each node, an entanglement state can be shared between two neighbor nodes and separated over 100km. Elemental technologies for quantum repeaters include interfaces that connect single photons, as a communication medium, to single quantum systems in solid states as quantum memories. While cold atoms

and diamond NV centers have been proposed as candidates of quantum systems for quantum repeaters, in this study, we focus on electron spins in gate-defined lateral quantum dots (QDs) since it is one of the suitable qubits of quantum computers. Indeed, the electron spins in the QDs are known to possess several advantages for the realization of the quantum repeaters: (I) good compatibility with the communication telecomwavelength, (II) scalability for large scale quantum systems for introducing a quantum error correction scheme to the quantum communication in future, and (III) relatively long spin coherence time[6] . Therefore, to realize the above-mentioned quantum interface, the quantum state conversion from photons to electron spins with preserving the coherence of the photon states is needed[1].

Preceding works on quantum state conversion from photon polarizations to electron spins

In 2001, based on the well-established optical selection rule of the interband transition in semiconductors, Vrijen and Yablonovitch proposed the theory of quantum state transfer from photon polarizations to electron spins using quantum wells (QWs) [73], which is expected to be applied on QDs system. Later, quantum state transfer [2] from light i.e. -many photons to many electron spins in ensemble was experimentally demonstrated by Kosaka et al.[39, 38]. Since the quantum state of an individual single photon has to be discriminated in the entanglement distribution, the ensemble quantum state conversion cannot be used as a quantum interface. The quantum state conversion from a single photon polarization state to a single electron spin state has to be realized. As for the research on the single-photon-electron spin quantum interface, QDs that can manipulate and detect single electron spins is a promising platform. Detection of single photoelectrons generated by single photon absorption in a QD has been demonstrated using nearby charge sensors, which is well established as a fundamental technology for spin qubit operations [42, 60]. Fujita *et al.* has reported[20] that they have succeeded in the detection of electron

[1]It should be noted that the phase coherence of electron spins, commonly called "quantum coherence", is fundamentally different from the more commonly known laser coherence.

[2]While the word "Quantum State Transfer" is used in early papers, we use "Quantum State Conversion" in this paper.

spin states (up or down) excited by circularly polarized photons, which is called angular momentum transfer. The single photoelectron spin detection has been realized using two electron spin correlation, namely Pauli exclusion principle, between the initially-loaded electron spin and the photoelectron spins in a double QD (DQD). This experiment was demonstrated by exciting heavy-hole states that have three times larger transition probability than light hole states. Generally, the efficiency of the photon absorption is associated with the density of states of the valence band state. This correspondence has been experimentally examined from the wavelength dependence of single photoelectron detection probability in a QD [49].

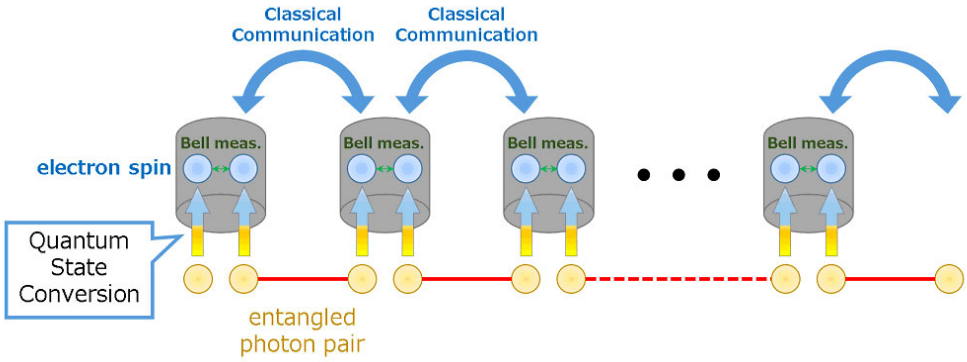

Fig. 0.0.1: Schematic of the quantum repeater

(110) Quantum Wells

The growth direction of GaAs QWs is conventionally along [001] direction and it is well investigated for the characteristics of spin orbit interaction or g-factor in (001) QWs[76, 24, 65, 35]. Since the quantum state conversion requires a large Zeeman splitting of hole states under an in-plane magnetic field, the quantum state conversion is possible only for light hole states that has a finite in-plane g-factor and is impossible for heavy hole states that has near zero in-plane g-factor in conventional (001) QWs. However, in the QWs grown on different crystal orientation like (110) heavy hole states can have a non-zero g-factor for in-plane external magnetic field[78, 22]. It is expected that selective excitation of one of Zeeman split levels of heavy hole enables more efficient quantum state conversion utilizing transition

probability three times higher than light hole states. Moreover, the different crystallographic orientation changes the anisotropy of spin-orbit interaction induced by bulk-inversion-asymmetry (BIA) in two-dimensional systems. Since the spin-orbit interaction is a major cause of the spin relaxation in QWs, the QWs grown on a different orientation provides different spin relaxation process. Spin relaxations and spin transports in (110) QW have been well studied [54, 2, 8, 28]. Indeed, the elongation of spin relaxation time by suppressing the random presessional motion of electron spins under an effective spin-orbit field perpendicular to the (110) plane has been realized in (110) GaAs QWs [54].

Purpose and contents of this thesis

We expect that the low-dimensional systems using (110) QW substrate will bring many possibilities for basic physics and application to quantum information related to specific spin-orbit interactions and anisotropy of electron and hole g-factors. Lateral QDs are a most useful device to explore the properties of a few electron in low dimensional structures because of the high electrical controllability of quantum states in the QDs. However for (110) QW substrates, almost no study using gate-defined QDs have been reported to the best of our knowledge.

Moreover, efficient photon illumination technology is essential for the research on photon-electron spin quantum interface. In previous experiments, line-of-sight light delivery system was used to directly illuminate QD devices at low temperature through an optical window at room temperature on a dilution refrigerator. The receiving efficiency of photons into the dot area is limited by the size of the laser spot, which causes terrible loss of photons on each illumination trial. Optical fiber delivery system using low temperature piezo-stages is proposed at NRC, but the application of the low temperature optical system to the photon-spin quantum interface based on a gate-defined QDs has not yet demonstrated.

The development of sophisticated semiconductor devices and revolutional communication technology is expected to proceeded dramatically within near generation period. In this thesis work, we aim to promote the development of next-generation semiconductor spintronics by deepening the understanding of the electron transport in low dimensional semiconductor structures. Additionally, we also aim to proceed

the experimental technology to explore the photo-excited quantum state by establishing the measurement system to irraidate suprer-small spot laser on a device held in low temperature where quantum phenomena is observable.

The results achieved in this thesis will contribute to realizing highly efficient quantum state conversion for a development of future quantum repeater technology and to understand the basic physics related to spin-orbit interaction and resultant spin manipulations in GaAs QD on (110) substrate.

This thesis is organized as follows.

In Chapter 1, we show the basic theories and previous experimental works as background necessary for the understanding of the achievement in this thesis.

In Chapter 2, we show the growth and basic characterizations of the (110) GaAs QW structure used in this thesis. The details in the layer profile and the growth in molecular beam epitaxy (MBE) are explained. The magneto-transport measurements are performed to estimate the carrier density and mobility at low temperature. We find that the mobility of the (110) QW is moderately high enough for the experiments conduction of gate-defined QDs.

In Chapter 3, we report, for the first time, the formations of QDs in a multi-electron regime and a few electron regime. Charge sensing is also demonstrated in the (110) QDs. During the formation of a DQD, we find that a unintentional QDs appear and sometimes couples to the other intentional dots. Finally, we could operate the devices as a DQD in a restricted few electron regime.

In Chapter 4, we start from explaining the device design modified for studying the influence anisotropies of spin-orbit interaction and g-factor. Details in the device fabrication procedure with an optical mask for quantum state conversion experiments is described. The setup in the dilution refrigerator, optimized for low-electron-temperature, mechanically adjustable, highly light focusing, and microwave-frequency compatible setup aimed for coherent conversion, is also shown. Then, we observe Pauli spin blockade (PSB) effect by measuring the magnetic field dependence of the transport triangles through the DQD in two different electron number regions. From the leakage current in the PSB region at low magnetic fields, we evaluate the in-plane g-factors of an electron and find that the value agrees to the value expected from the well width.

In Chapter 5, the sets up and operation scheme of the optical fiber delivery systems is discussed for the efficient photon illumination to QDs. The scanning images obtained by the photocurrent and photoreflectance measurements are discussed. By improving stability and resolution of the scanning system, we can recognize two tiny apertures of diameter of about 500 nm on the optical mask above the QDs clearly.

In Chapter 6, we summarize the results and discussion in this thesis and discuss the significance of our achievements and future prospects for the contributions to the future quantum technologies and quantum networks.

Chapter 1

Background

1.1 Physics of Two Dimensional Semiconductors

1.1.1 Semiconductor physics

At first, the most fundamental semiconductor properties related to our experiment is explained here.

GaAs

GaAs is a compound semiconductor consisted with gallium in group 3 element and arsenic in group 5 element in the periodic table , composited in the same ratio. Electrons conducting in GaAs have small effective mass and high mobility [1]. That is why it is used for High Electron Mobility Transistor (HEMT), Schottky diode (SD), and Heterobipolar Transistor (HBT). Moreover, it is also useful for emission diode or semiconductor laser of red or infrared light because of characteristics as optical direct-transition semiconductor.

Si and GaAs are distinguished in covalent bond crystal whose binding power derives from exchange interaction, which depends on electron spins and Coulomb force. Valence band structure of the GaAs crystal is more complicated than in Si consisted with single element semiconductors.

[1] You can find from the relationship $\mu = e\tau/m^*$ of that small effective mass can contribute to high mobility

In the case of Si, its electron structure is provided as $(1s)^2(2s)^2(2p)^6(3s)^2(3p)^2$. There are four valence electrons, two of which occupy s-orbitals, and the other two are in three p-orbitals that can accommodate up to six electrons. The covalent bond that is an orbital hybridization of the outermost electrons $(3s)^2$ and $(3p)^2$ constitutes four orbitals extending in a regular tetrahedral fashion, that is, sp^3 hybrid orbitals. As a result, each element connects with the adjacent element in the direction corresponding to the corner of the tetrahedron by sharing electrons with opposite spins, forming a diamond structure (diamond lattice) as a whole.

On the other hand, GaAs has a low symmetry in the crystal structure, so the transfer of electrons from As to Ga causes the electronic structure to change as follows:

$$\begin{aligned} \mathrm{Ga} : (3d)^{10}(4s)^2(4p)^1 &\rightarrow (3d)^{10}(4s)^2(4p)^2 \\ \mathrm{As} : (3d)^{10}(4s)^2(4p)^3 &\rightarrow (3d)^{10}(4s)^2(4p)^2 \end{aligned}$$

Then, Ga and As extend their bonds tetrahedral in the same way as Si, and form a zincblende structure by combining with different adjacent elements. Table 1.1.1 shows the energy gap E_g of GaAs[26].

Table 1.1.1: Energy gap of GaAs on temperature

–	E_g (0 K)[eV]	E_g (300 K)[eV]	E_g(T) [eV]
GaAs	1.519[a]	1.424[a]	$1.519 - 5.405 \times 10^{-4} \times \mathrm{T}^2/(\mathrm{T} + 204)$

[a] Experimental value.

In addition, ionic properties are added to the bond due to charge transfer during bonding. This weakens the hybridization and about -8 eV the valence band splits into a single band with s-orbital and a triple band with three p-orbitals.

AlGaAs

AlGaAs is a mixed crystal material of Al and GaAs. Fig. 1.1.1(a) shows the Al composition dependence of the energy gap at the Γ point, X point, and L point of

AlGaAs at room temperature. This energy gap is defined as the difference between the energies of the Γ point, X point, and L point of the lowest energy band of the conduction band and the upper end of the valence band (Γ point). Ref. [62] or [63] show the Al ratio dependence of these energy gaps by the following equations:

$$E_g(\Gamma) = 1.424 + 1.247x \qquad (0 \leq x \leq 0.45) \tag{1.1.1}$$

$$E_g(\Gamma) = 1.424 + 1.247x + 1.147(x - 0.45)^2 \qquad (0.45 \leq x \leq 1.0) \tag{1.1.2}$$

$$E_g(\mathrm{X}) = 1.708 + 0.642x \qquad (0 \leq x \leq 1.0) \tag{1.1.3}$$

$$E_g(\mathrm{L}) = 1.900 + 0.125x + 0.143x^2 \qquad (0 \leq x \leq 1.0) \tag{1.1.4}$$

Since the energy gap at each point changes depending on the composition of GaAs and Al, $\mathrm{Al}_x\mathrm{Ga}_{1-x}\mathrm{As}$ is a direct transition semiconductor as x below 45, and an indirect transition semiconductor as x above 0.45.

With referring the parameters in Ref. [3], the temperature dependence is calculated as follows[45],

$$E_{g\Gamma}(\mathrm{T}) = E_{g\Gamma}(0) - \frac{5.41 \times 10^{-4} \cdot \mathrm{T}^2}{\mathrm{T} + 204} \tag{1.1.5}$$

$$E_{g\Gamma}(0) = 1.519 + 1.155x + 0.37x^2$$

$$E_{g\mathrm{X}}(\mathrm{T}) = E_{g\mathrm{X}}(0) - \frac{4.6 \times 10^{-4} \cdot \mathrm{T}^2}{\mathrm{T} + 204} \tag{1.1.6}$$

$$E_{g\mathrm{X}}(0) = 1.981 + 0.124x + 0.144x^2$$

$$E_{g\mathrm{L}}(\mathrm{T}) = E_{g\mathrm{L}}(0) - \frac{6.05 \times 10^{-4} \cdot \mathrm{T}^2}{\mathrm{T} + 204} \tag{1.1.7}$$

$$E_{g\mathrm{L}}(0) = 1.815 + 0.069x.$$

Effective mass of electrons at the Γ-, X-, L- band are obtained as follows,

density of states effective mass	conductivity effective mass
$m_e(\Gamma) = (0.067 + 0.083x)m_0$	$m_e(\Gamma) = (0.067 + 0.083x)m_0$
$m_e(\mathrm{X}) = (0.85 - 0.14x)m_0$	$m_e(\mathrm{X}) = (0.32 - 0.06x)m_0$
$m_e(\mathrm{L}) = (0.56 + 0.1x)m_0$	$m_e(\mathrm{L}) = (0.62 + 0.14x)m_0$.

Additionally, effective mass of heavy hole m_{hh} and of light hole m_{lh} are given as

$$m_{hh} = (0.62 + 0.14x)m_0 \quad , \; m_{lh} = (0.087 + 0.063x)m_0.$$

The refractive index of AlGaAs decreases as the Al composition increases, and increases as the photon energy increases. The changes are shown in the Fig. 1.1.1(b). The peaks seen in the refractive index spectrum are due to excitons.

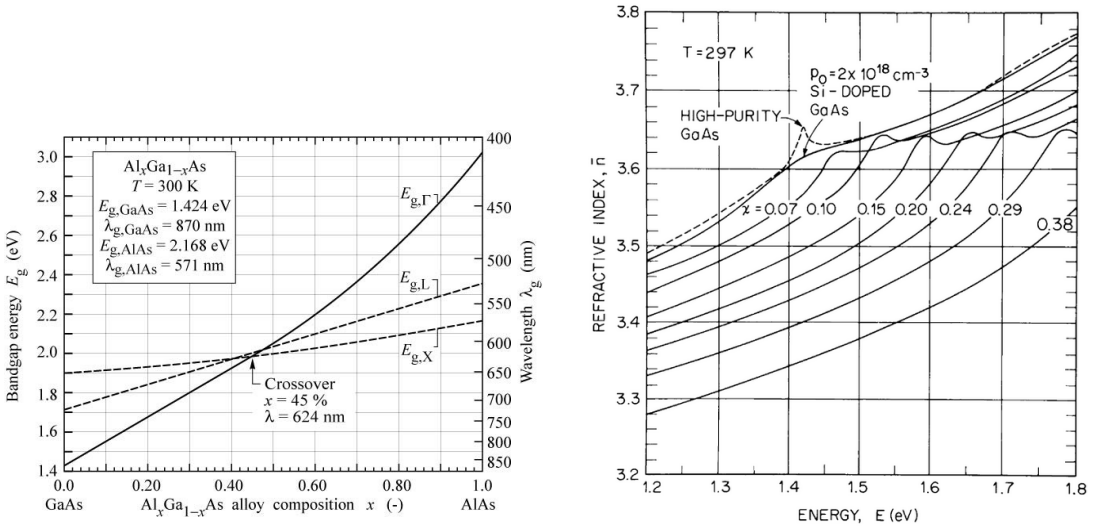

(a) E_g of AlGaAs atΓpoint、X point、or L pooint

(b) Al composition dependence of refractive index of AlGaAs

Fig. 1.1.1: Energy gap E_g and refractive index of AlGaAs[26][25]

1.1.2 Two-dimensional Electron Gas

Close lattice constants between GaAs and $Al_xGa_{1-x}As$ allow the epitaxial growth to form a very high quality interface which is flat in atomic level. Such an interface consisting with different kind semiconductor material is called heterointerface or heterostructure. The band gap energy of GaAs is 1.42 eV and the energy of $Al_xGa_{1-x}As$ is about 1.8 eV at room temperature which depends on the composition ratio of each materia., Electrons are confined in the GaAs layer in a sandwiched structure so-called "quantum well" composed with double $Al_xGa_{1-x}As$ layers and GaAs layers. If the thickness of the GaAs layer is comparable to the electron wavefunction, nano-scale confinement in the perpendicular direction to the substrate results in a quantum effect such as resolving degeneracy of heavy hole and light hole levels of the valence bands in GaAs. This effect is very useful for selective optical

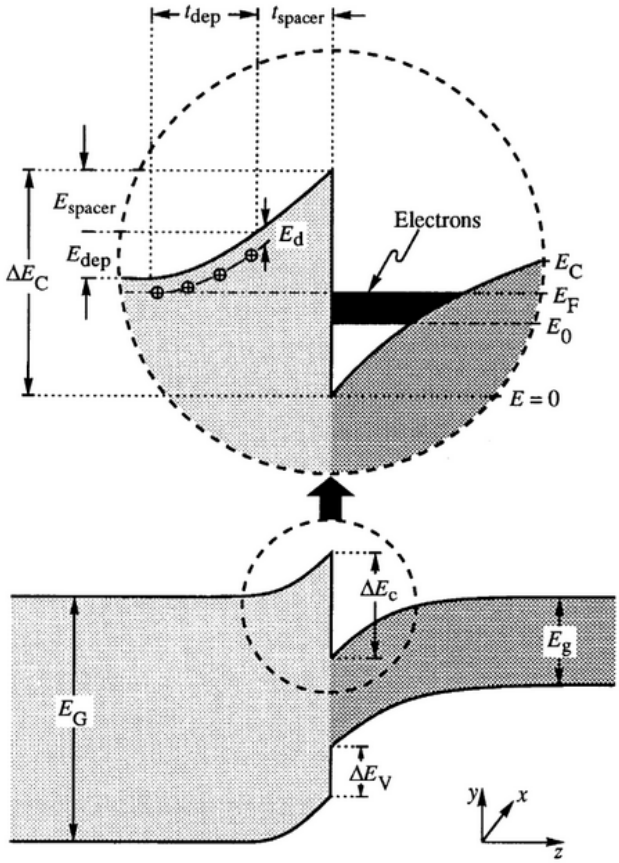

Fig. 1.1.2: The schematic band diagram of the selectively doped heterostructure[62]

excitation explained in Section 1.5.1.

Next, the confinement at the heterointeraface between a single GaAs layer and a single $Al_xGa_{1-x}As$ layer (not sandwich structure) is explained. Electron carriers are not confined at the interface of an undoped heterostructure. Almost no conductivity is observed because the Fermi level is below the conduction band. However, if selectively n-doped AlGaAs layer is inserted into the barrier layer of the undoped AlGaAs slightly separated from the interface, the carriers are induced at the interface. Figure 1.1.2 shows the schematic band diagram of the selectively doped heterostructure. The Fermi level of AlGaAs is higher than the level of GaAs due to the difference between the band gap energy. Carriers induced by the doping in AlGaAs barrier layer do not stay in the doped layer but move to the GaAs layer because of the difference of electron affinity between GaAs and AlGaAs ($\chi_{GaAs} = 4.07\,eV > \chi_{AlGaAs} = 3.5\,eV$).

Then the provided electrons from AlGaAs are captured in the GaAs layer of the conduction band step at the interface due to the resulting built-in electric field after the carries escape from the dopants. Thorough the above process, positively charged donors and negatively charged electrons are separated, which generates the electrostatic potential suppressing the electron transfer from AlGaAs to GaAs. As a result, conduction band shows the sharpen shape near the interface. Electrons are attracted to the AlGaAs side by the electric field generated between the separated charges, and are pressed on the interface in GaAs. Electrons are confined in the z-direction, perpendicular to the substrate, and can move freely in the x and y direction, in-plane of the substrate, which form the electrons sheet called two-dimensional electron gas. Z-direction confinement can be enhanced by combining the QW structure while sustaining the high mobility[2]. The advantage of such a doped structure is that electrons and doped impurities (donors) are separated. This makes the electrons less affected by the ionized impurity scattering, which provide high mobility to electrons. This design is called HEMT (high electron mobility transistor) structure. Furthermore, if an undoped AlGaAs layer is inserted between the n-AlGaAs and GaAs as an isolation layer (spacer), the separation of electrons and donors becomes more reliable, and the influence of scattering can be further suppressed. As a result, higher mobility is expected, but the electron density also decreases. Experiments in the field of physics often require high mobility, but in the field of engineering the electron density may be rather important, so a design according to the application is required.

1.1.3 Quantum Hall effect

Landau quantization

Here we will assume the situation when a perpendicular magnetic field is applied to the electrons in a two-dimensional system. Bloch electrons trapped in a periodic potential in a crystal can be treated as free particles by introducing the concept of effective mass. Now consider a two-dimensional free particle with mass m and

[2]Electrons feel fluctuation of the interface between GaAs and AlGaAs layers, so it is generally more difficult to get high mobility in the case of quantum well rather than HEMT structure.

charge $-e$ confined in a rectangle of $L_x \times L_y$.

By introducing the vector potential $\mathbf{A}$, the Hamiltonian of the two-dimensional system is,

$$H(p_x, p_y) = \frac{1}{2m}\left(\mathbf{p} - \frac{e}{c}\mathbf{A}\right)^2. \tag{1.1.8}$$

Furthermore, since the magnetic field is perpendicular to the z-axis direction, the Hamiltonian H is,

$$H(p_x, p_y) = \frac{1}{2m}\left[p_x^2 + \left(p_y - \frac{e}{c}Bx\right)^2\right]. \tag{1.1.9}$$

Since the position coordinate y is not included in the Hamiltonian H, p_y and H are commutative, so p_y is a conserved quantity. In other words, the wave function becomes a plane wave with respect to the y axis direction.

Replacing $p_y \to \hbar k_y$ changes the formula of H as below,

$$\begin{aligned} H(p_x, \hbar k_y) &= \frac{1}{2m}p_x^2 + \frac{e^2B^2}{2mc^2}\left(\frac{\hbar c k_y}{eB} - x\right) \\ &= \frac{1}{2m}p_x^2 + \frac{m\omega_c^2}{2}(x - X)^2 \end{aligned} \tag{1.1.10}$$

New variables of,

$$\omega_c \equiv \frac{eB}{mc} \tag{1.1.11}$$

$$X \equiv \frac{\hbar c k_y}{eB} = l_B^2 k_y \qquad \left(l_B = \sqrt{\frac{\hbar c}{eB}}\right) \tag{1.1.12}$$

are introduced.

Since the expression (1.1.10) has the same form as the Hamiltonian of the one-dimensional harmonic oscillator, it has a solution of the harmonic oscillator as a one-dimensional system with respect to x. Here, we focus on the energy eigenvalues derived in the same way of the case of harmonic oscillator. The energy eigenvalue is obtained as discrete values as,

$$E_n = \hbar\omega_c\left(n + \frac{1}{2}\right). \tag{1.1.13}$$

This is called Landau quantization. This quantized energy eigenvalues do not depend on the value of X, so it is degenerate by the number of possible X. Now the solution

corresponds to a plane wave along the y axis, and k_y is quantized in $2\pi m_y/L_y (m_y = 0, \pm 1, \pm 2, \dots)$. Therefore, X in (1.1.12) is also quantized.

From the form of the equation, X means the origin of the harmonic oscillator, but since the oscillating x can only be between 0 and L_x, the possible range for X, the origin of oscillation, is is limited to $0 \leq X \leq L_x$. This fact gives,

$$\begin{aligned} l_B^2 \left(2\pi/L_y\right) m_{max} &= X_{max} = L_x \\ \rightarrow m_{max} &= \frac{L_x L_y}{2\pi l_B^2}, \end{aligned} \tag{1.1.14}$$

which means that each Landau level is $m_{max}-$th degenerate.

Here, if the total number of electrons in the two-dimensional system under consideration is N_s, the filling factor ν can be defined as follows,

$$\nu \equiv \frac{N_s}{m_{max}} = 2\pi l_B^2 \frac{N_s}{L_x L_y} = 2\pi l_B^2 n_{2D}, \tag{1.1.15}$$

which represents the number of Landau levels occupied by an electron. This filling factor corresponds to the number of Landau levels completely filled by electrons at T=0 K. n_{2D} is the two-dimensional electron density.

Shubnikov-de Haas oscillations

Substitution of l_B^2 given by the (1.1.12) into (1.1.15) reveals the relationship between the filling factor and the magnetic field as,

$$\nu = 2\pi \frac{\hbar c}{eB} n_{2D} = \frac{n_{2D}}{eB/h}. \tag{1.1.16}$$

From this relation, it can be seen that the filling factor decreases continuously as the magnetic field increases. When ν is an integer, the Fermi energy is between the Landau gaps and the longitudinal resistance is minimal. Magnetic oscillations of resistance are thus observed. Such oscillations are called Shubnikov-de Haas oscillations. The electron density can be calculated from the period of this oscillation.

A qualitative description of the quantum Hall effect

The above explanation is about the formation of the Landau levels and the oscillation phenomenon of magnetoresistance associated with it. This is about the longitudinal

resistance ρ_{xx}, that is, the dissipative conductivity σ_{xx}. On the other hand, the Hall resistivity ρ_{xy} behaves differently. In the range where the dissipative conductivity σ_{xx} disappears, the Hall conductivity σ_{xy} is independent of the sample parameters, magnetic field, temperature, and other factors, and is a universal constant from only e and $\hbar$ shown as,

$$\sigma_{xy} = \frac{e^2 N}{2\pi\hbar}. \tag{1.1.17}$$

The lateral resistance ρ_{xy} is shown as below, which corresponds to the result of experiments,

$$\rho_{xy} = \frac{2\pi\hbar}{e^2 N}. \tag{1.1.18}$$

This formula 1.1.18 shows us that the highly accurate measurements of Hall conductivity in two-dimensional structures provides us an accurate value of e^2/h. Therefore, the quantum Hall effect is generally recognized as a method that can determine the fine structure constant $e^2/\hbar c$ with extremely high accuracy. Also, the quantity $2\pi\hbar/e^2$ found from the quantum Hall effect has the same dimension of resistance, and its value is about $25813\,\Omega$. Hence, a two-dimensional system giving a clear plateau structure is utilized as a resistance standard.

1.2 Spin Orbit Interaction

1.2.1 Spin Relaxation Mechanism

Compared to metal, longer spin relaxation time and coherent transport distances are reported in semiconductor materials[81, 4, 18]. Generally, spin relaxation mechanisms can be understood by the random fluctuation of effective field derived from spin orbit interaction explained here in section 1.2. Many effects of relaxation mechanisms are suggested [18]. One of the four representative spin relaxation mechanisms is shown below as a important mechanism in (110) QWs.

D'yakonov -Perel' Mechanism[16, 15]

D'yakonov -Perel' (DP) mechanism is dominant at room temperature in solids lacking spatial inversion symmetry of the crystalline structure, like zinc-blend. The group III-V compound semiconductor, GaAs is one of the most famous examples.

This symmetry breaking also known as bulk inversion asymmetry gives rise to Dresselhaus spin orbit interaction. Electrons also feel strong spin-orbit interaction under an externally applied electric field or a built-in electric field due to asymmetric quantum confinement or at the heterostructure interface. These asymmetric potential distributions known as structural inversion asymmetry gives rise to Rashba spin orbit interaction.

These interactions lift the degeneracy between up-spin and down-spin when the electrons are in the non-zero momentum state. Dresselhaus and Rashba interactions truly behave like effective magnetic fields B_{BIA} and B_{SIA}, since the lifting of the degeneracy corresponds to Zeeman splitting by an external magnetic field which is independent to the electron wave vector. Each electron feels effective fields $\vec{B}_{BIA}$ and $\vec{B}_{SIA}$ corresponding to the electron's velocity $\vec{v}$. The electrons undergo a Larmor precession whose axis is collinear with the effective field $\vec{B}(\vec{v}) = \vec{B}_{BIA} + \vec{B}_{SIA}$, and the precession frequency is $\Omega(\vec{v}) = g\mu_B B(\vec{v})/\hbar$.

Spin-orbit field $\vec{B}$ changes its direction by scattering, which changes the electron's wave vector. If the wave vector and the electron velocity $\vec{v}$, changes randomly with time by scattering, then different electrons will have different precession axes. In the case of an ensemble of electrons, spin polarization will be lost after time evolution. This is the basic concept of DP mechanism [16]. The motional narrowing effect and control of spin relaxation rate by engineering the devices geometries are demonstrated using 2D electron gas (quantum well structure with top gate)[61].

Spin relaxation time τ_s can be represented as,

$$\frac{1}{\tau_s} \sim \omega_{so}^2 \tau \tag{1.2.1}$$

in the case of non-magnetic materials like semiconductors having zero- or weak external magnetic field. The magnitude of $\omega_{so}^2\tau$ is the measure of the strength of the spin-orbit coupling. The spin relaxation rate is proportional to the momentum relaxation time. In other words, more frequent electron scattering causes less spin dephasing.

Electron spin relaxation time τ_s by the DP mechanism in quantum wells grown in the [001] direction can be represented as,

$$\frac{1}{\tau_s} = \frac{16 k_B T m^{*3} (\gamma E_{1e})^2}{\hbar^5} \tau_\nu \tag{1.2.2}$$

where k_B is the Boltzmann constant, T is the absolute temperature, m^* is the effective mass of electron, γ is the splitting factor, E_{1e} is the confinement energy, and τ_ν is the electron momentum relaxation time[5, 82]. In a high-quality well, the DP mechanism becomes remarkably small due to the suppression of scattering. In the narrower well structure, larger E_{1e} contributes to the DP mechanism.

Spn relaxation in GaAs (110) QW

DP mechanism is significant in GaAs QWs, therefore (110)-oriented QWs were exploited to lengthen the electron spin relaxation timeτ_s[15]. Ohno *et al.* reported long spin relaxation time on the order of a few ns at room temperature[54], which is longer by one order of magnitude than that of a (001) GaAs substrate[7, 48, 69]

In a (001) QW, $\vec{B}_{BIA}$ is generated in the in-plane direction, and the electron spin precess randomly against $\vec{B}_{BIA}$ on average, then spin polarization is disappeared. In a (110) QW, $\vec{B}_{BIA}$ is generated at out-of-plane, and $\vec{B}_{BIA}$ does not cause precession for electron spins polarized perpendicular to the substrate. In a (110) GaAs QW, in which DP mechanism is suppressed, the BAP mechanism must be dominant from room temperature to low temperature. Exciton states, in which electron-hole exchange interaction is enhanced, could be generated easily at low temperature, so it is said that the relaxation time τ_s in (110) QWs is longer at room temperature[54].

By n-type doping in the GaAs (110) QW and suppressing electron-hole interaction, about 20 ns relaxation time τ_s is shown[1]. Localized electrical field by impurity ions generate an effective random field through spin orbit interaction. The limitation of relaxation time τ_s is also reported[50, 66] under the environment where both of DP and BAP mechanism is suppressed.

In symmetric GaAs (110) QWs, the D'yakonov-Perel' term mainly comes from the Dresselhaus term, and which can be written as,

$$g\mu_B\Omega_x^{nn'}(\mathbf{k}) = \gamma_D[-(k_x^2+2k_y^2)\langle n|\,k_z\,|n'\rangle + \langle n|\,k_z^3\,|n'\rangle], \tag{1.2.3}$$

$$g\mu_B\Omega_y^{nn'}(\mathbf{k}) = 4\gamma_D k_x k_y \langle n|\,k_z\,|n'\rangle\,, \tag{1.2.4}$$

$$g\mu_B\Omega_z^{nn'}(\mathbf{k}) = \gamma_D(k_x^2-2k_y^2-\langle n|\,k_z^2\,|n'\rangle)\delta_{nn'}. \tag{1.2.5}$$

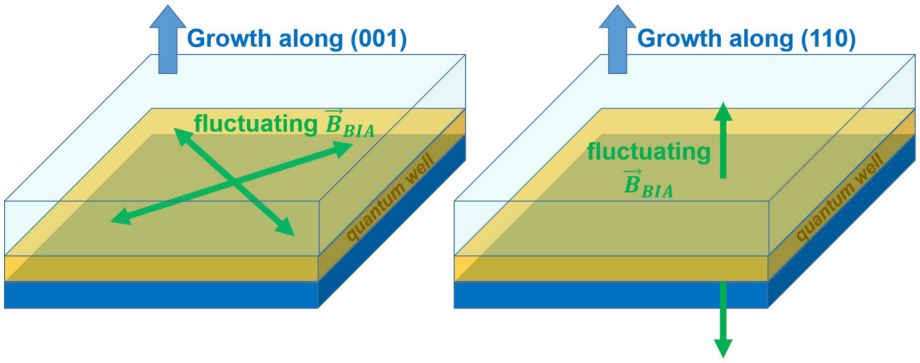

Fig. 1.2.1: $\vec{B}_{BIA}$ in (001) QW and (110) QW

Electrons transporting in the quantum well feel the effective magnetic field, following this formula[79]. Different from the (001) QW or the (111) QW, the effective Dresselhaus magnetic field direction is perpendicular to the plane. Then, the spin polarization perpendicular to the substrate have no spin torque from BIA. Longer ensemble spin relaxation time is reported demonstrating this phenomena[1, 64, 72]. If the k-direction is limited parallel to [001], the effective magnetic field deriving from spin orbit interaction is only in-plane direction, and if right angle direction to [001] as well as $[11\bar{1}]$, the field is maximized. Spin manipulation utilizing such characteristics is reported[11, 12, 28].

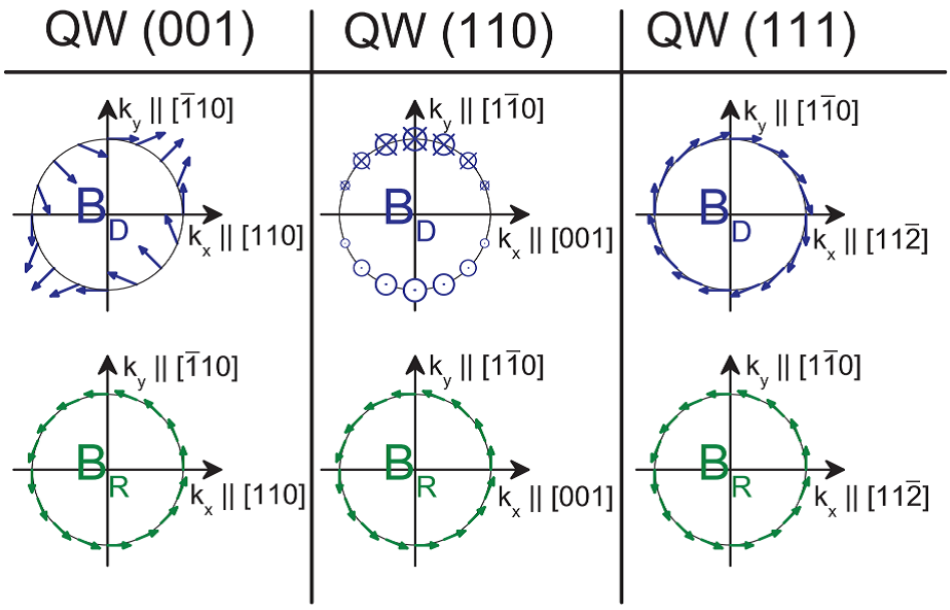

Fig. 1.2.2: Effective magnetic field direction by spin orbit interaction on each crystal orientation quantum well as (001), (110) and (111)[28].

1.3 Physics of Zero-dimensional Electrons

Development of high quality semiconductor substrates engineering, and nano-scale device fabrication technology enabled us to locally confine and control few carriers in semiconductor devices. Especially, quantum dots (QDs), often referred to as "artificial atoms", are a critical technology to access the charge and spin states of electron/hole to investigate quantum mechanics in solid. Charge and spin states in QDs can be detected by electrical transport combined with low-temperature electronics technology.

Various kinds of device structures have been proposed theoretically and demonstrated experimentally. In this thesis we focus on gate-defined QDs, which is constructed with a high quality two-dimensional electron sheet, nano-scale fine gates on the surface of the substrate, and ohmic contacts *etc.* Fig 1.3.1 shows the simplified device structures and SEM images from the top. As explained in section 1.1.2, at the hetero-interface between layers of different kinds of semiconductor materials, carriers are confined due to the band bending and doping. Carriers underneath

the electrode gates are depleted due to the difference of work functions between the metal and semiconductor, and the applied negative (or positive) voltages that extend the depleted regions around the gates. Appropriately designed gates allow to confine carriers locally, forming QDs, controlling the number of carriers, and tunneling rate between the QDs and the reservoir. Locally confined carriers by the electrical potential of gate voltages follow the discrete energy levels, and each carriers' charge and spin states are resolved by the QD coupling to the reservoir through tunnel barriers. The spin state of the carriers are strongly affected by the coupling state and controllable by tunnel barriers. Furthermore, scalable structure is achieved by coupling more than two dots via tunnel barriers, which is referred to as "artificial molecules" (see 1.3.1 (c)).

In this section, fundamental properties of the single and multiple QDs are outlined.

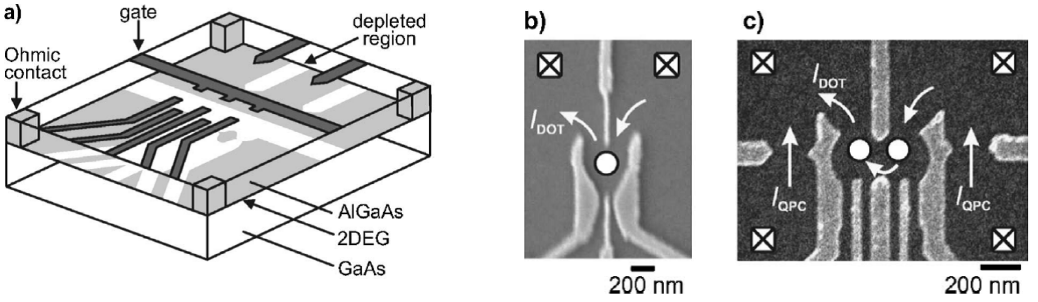

Fig. 1.3.1: Lateral quantum dot devices[27]. (a) Simplified illustration of gate-defined lateral quantum dot devices. Fine-gate patterns are delineated by using the EB lithography system, and the gates are fabricated by deposition of metals such as titanium and gold. Two-dimensional electron gas (2DEG), electrons confined in a sheet structure, is formed at the hetero-interface or the quantum well layer. The depleted area can be controlled by applying proper negative voltage on the gates. Ohmic contacts are electrically conductive regions from 2DEG to the outside ,which is formed using AuGe and Ni diffusion. (b),(c) Scanning electron micrograph (SEM) images of a single and double quantum dot sample. The white patterns correspond to fine gates and the black bordered white painted circles show the place where QDs should be formed.

1.3.1 Single Quantum Dot

In the gate-defined QDs, electrons are confined by the electrical potential created by the gate voltages. The QDs are coupled to leads, which connects the system through ohmic contacts for transport measurements. The leads work as electron reservoirs, provider of electrons into QDs. The strength of coupling between the QDs and the leads (thus the tunneling rate) can be controlled by the barrier gate voltage. Each electron confined in QDs follow the discrete energy levels and the number of electrons occupying in the QD is determined by the chemical potential, which is capacitively controlled with the gate voltage. Through the observation of dot current I_{dot} and changing the gate voltage together with the chemical potential, periodic sharp peaks can be observed. This characteristic transport phenomenon is called Coulomb oscillation and can be explained by the constant interaction (CI) model[27].

In order to get the total energy $U(N)$ where the QD contains N electrons, the model must be based on important two assumption:

(i) The Coulomb interactions of an electron on the dot with all other electrons, both inside and outside the dot, are parametrized by a constant capacitance C.

(ii) The discrete, single-particle energy spectrum, calculated for non-interacting electrons, is unaffected by the interactions.

It is not easy to calculate the Coulomb energy between electrons exactly, so in the first assumption, constant capacitance C independent with the number of electrons is used. The capacitance is given by $C = C_S + C_D + C_G$, where C_S, C_D,and C_G are the capacitance between dot-source, dot-drain, and dot -gate respectively. Then the total ground state energy of the QD containing N electrons is represented as follows,

$$U(N) = \frac{[-|e|(N_0^N - C_G V_G)]^2}{2C} + \sum_{n=1}^{N} E_n, \tag{1.3.1}$$

where $N_0 e$ is an off set charge derived from ionized donors in semiconductors, V_G is the voltage applied to the gate [3], and E_n is the energy of the zero-dimensional

[3] $C_G V_G$ corresponds with the continuous charge induced by gate voltage in QD.

quantum confinement level, which means the last term of (1.3.1) is the summation of energy when adding N electrons in order from the one-electron level. Real electron number N in the QD and dot current I_{dot} depend on the relative relationship between electrochemical potential $\mu(N)$ and source-drain electrode chemical potential μ_S, μ_D. $\mu(N)$ is defined as,

$$\mu(N) \equiv U(N) - U(N-1) \tag{1.3.2}$$

$$= (N - N_0 - \frac{1}{2})E_C - \frac{E_C}{e}C_G V_G + E_N, \tag{1.3.3}$$

with $E_C = e^2/C$ being a charging energy, If the applied dot bias $V_{sd} = \mu_D > 0$, only the electron in the transport window between μ_S and μ_D contributes to the net current through the QD[4]. When μ_N is under and μ_{N+1} is above the transport window, the additional energy,

$$E_{add} = \mu_{N+1} - \mu_N = E_C + \Delta E(N), \tag{1.3.4}$$

is needed in order to add an electron from the source lead to the dot or to extract an electron from the dot to the drain lead. $\Delta E(N) \equiv E_{N+1} - E_N$ is the splitting width of quantum levels, and $\Delta E(N) = 0$ when the $N+1$ electron fill the same orbit of the N electron due to the spin degeneracy, which means that additional energy E_{add} is equivalent to one charging energy. Electron conduction thorough the dot should be prevented if E_{add} is much larger than $k_B T$, the Fermi level blur due to thermal broadening and the tunnel couplings of the dot. This conduction prevention is called Coulomb blockade, and the number of electrons is fixed under this condition. The charging energy of GaAs QDs are generally about 1 meV, so Coulomb blockade can occur when cooled down under a few K.

1.3.2 Double Quantum Dot

Single QDs called as “artificial atoms” are explained in the previous section 1.3.1. It is natural to have an idea forming double quantum dots (DQDs) so-called “artificial molecule” by combing two dots[71]. Each dot state in the DQD can be controlled

[4]Assumed that V_{SD} is smaller than charging energy E_C

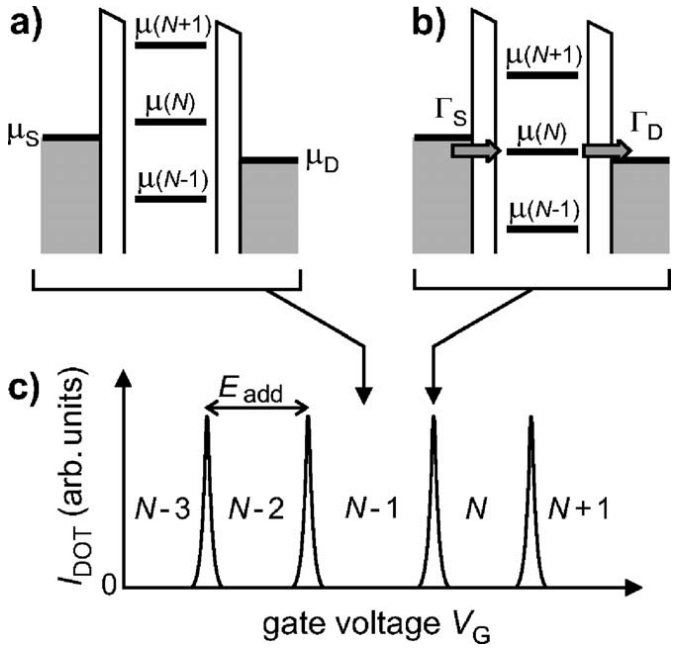

Fig. 1.3.2: Schematic energy spectrum and dot current[27]. (a) If no level of the electrochemical potential of the dot is set within the transport window between the Fermi levels μ_S and μ_D, the number of electrons is fixed due to the Coulomb blockade. (b) Chemical potential $\mu(N)$ is in the transport window, current through the QD so-called single electron current appears, when the number of electrons in the dot changes between $N-1$ and N. (c) Schematic plot of the dot current I_{dot} and gate voltage V_G. The gate voltage V_G can control the chemical potential of the dot, and the Coulomb peak where current flow and the electron number corresponding to (a) and (b) is indicated.

independently, which allows us to investigate the interesting physical features different from the real molecule. We investigated some aspects of transport of the DQDs in the special case.

Stability diagram of double dot

In the case of a single QD, capacitance between the dot and leads, and the dot and gates were assumed. Here, the classical model of a series double quantum dot involving the inter-dot capacitance C_m is introduced. Each dots is denoted as dot1

and dot2, containing the electron number N_1 and N_2 respectively. Moreover, each electron number can be tuned by gate voltages V_{G1} and V_{G2} independently.

$\mu_1(N_1, N_2)$ is defined as an electrochemical potential when the N_1 th electron is added to the dot1 while dot2 has N_2 electrons, then,

$$\mu_1(N_1, N_2) \equiv U(N_1, N_2) - U(N_1 - 1, N_2) \tag{1.3.5}$$

$$= (N_1 - \frac{1}{2})E_{C1} + N_2 E_{Cm} - \frac{C_{G1}V_{G1}E_{C1} + C_{g2}V_{G2}E_{Cm}}{e}. \tag{1.3.6}$$

Similarly, $\mu_2(N_1, N_2)$ is defined as an electrochemical potential when the N_2 th electron is added to the dot2 while dot1 has the N_1 electron, then,

$$\mu_2(N_1, N_2) \equiv U(N_1, N_2) - U(N_1, N_2 - 1) \tag{1.3.7}$$

$$= (N_2 - \frac{1}{2})E_{C2} + N_1 E_{Cm} - \frac{C_{G1}V_{G1}E_{Cm} + C_{G2}V_{G2}E_{C2}}{e}. \tag{1.3.8}$$

E_{C1} and E_{C2} indicate the charge energies of dot1 and dot2, respectively, and E_{Cm} is the electrostatic coupling energy. Here cross-capacitance between dot1(2) and $V_{G2}(V_{G1})$ are ignored to construct the simple model.

Fig. 1.3.3 is the charge stability diagram which shows the pair of the electron numbers contained in each dot as a function of V_{G1} and V_{G2}. When two dots are completely decoupled with each other ($E_{Cm} = 0$, $C_m = 0$), the diagram looks as Fig. 1.3.3(a). One of the gates $V_{g1(2)}$ change the electron number of dot1(2) without affecting the charge state of the other dot. If the coupling is enhanced($E_{Cm} > 0$, $C_m > 0$), the diagram becomes the honeycomb structure due the the inter-dot electrostatic coupling. For example $\mu_1(N_1, N_2)$ shifts to higher energy state as E_{Cm} compared to $\mu_1(N_1, N_2 - 1)$, and the domain which can contain stably the charge state (N_1, N_2) becomes hexagonal (Fig. 1.3.3(b)).

At the crossing point of three lines, called as "triple point", such as $\mu_1(0, 1) = \mu_2(1, 0)$, both dots, Coulomb blockade is lifted. Finite dot current can bes seen only near a triple point in the low-bias dot. At the triple point, $\mu_1(0, 1) = \mu_2(1, 0)$, electrons are carried from the source lead to the drain lead through the transition $(0, 0) \to (1, 0) \to (0, 1) \to (0, 0)$.

In the few electron regime of a double dot, the number of electrons trapped in two dots are counted from (0,0) charge state where no more charge transition lines

appear even when more largely negative voltage applied on gate electrodes. Stability diagram at few electron regime obtained by charge sensing method is shown at Fig. 1.3.4. In the bottom-left region, no more transition lines are observed, which means all electrons in dots are dispelled to the leads by negative gate potential.

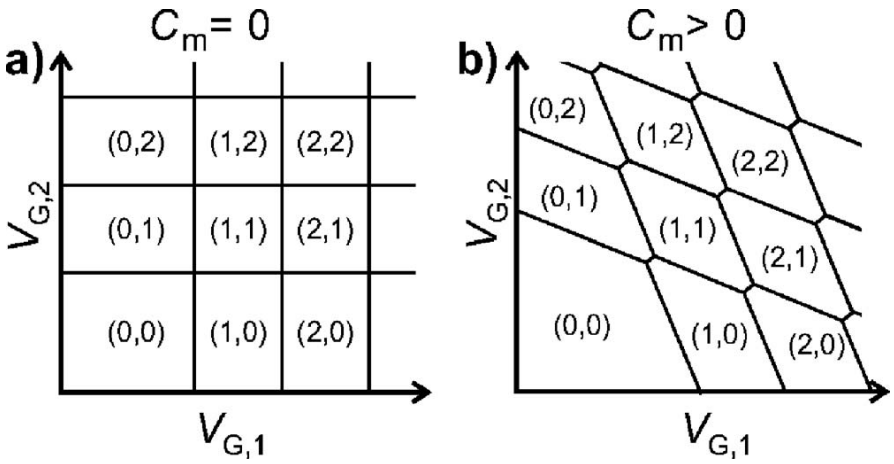

Fig. 1.3.3: Schematic stability diagram of the double quantum dot system in few electron regime. In the case of (a) small and (b) intermediate inter-dot coupling. The equilibrium electron number of each dot in each domain is denoted as (N_1, N_2).

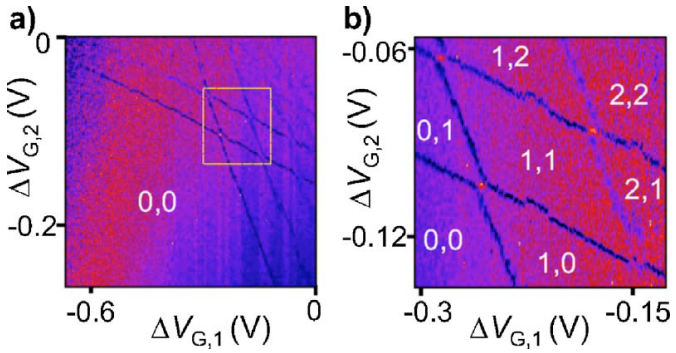

Fig. 1.3.4: Charge sensing data of the double quantum dot in the few electron regime.[17] Electron number in each quantum dot changes by crossing a dark signal line.

Bias triangle on a triple point

The low bias is assumed in the previous discussion of the double dot stability diagram which includes the transition lines to count the electron numbers detected by the charge sensing method. Net current through the dot I_{dot} is observed only at the triple points in a dot current measurement. High bias of the dot extend the transport region like a triangle shape as Fig. 1.3.5 which shows the schematic diagram of the "bias triangle", electrochemical potential state for each dots, and the Fermi levels of the source and drain leads. The bottom line of the triangle which is also the border between the domains $(0, 1)$ and $(1, 0)$ shows the resonance of the chemical potential levels for each dots as $\mu_1(1, 0) = \mu_2(0, 1)$. The contrast in the bias triangle shows the difference of dot current value, and the lines parallel to the bottom one in the triangle region indicate the contribution of the excited levels to the dot transport. Note that the left side triangle in the diagram can be interpreted as single electrons transport thorough the dots. On the other hand, two electron transport or hole charge transport can give the explanation of the right side triangle.

1.4 Pauli Spin Blockade

In the transport measurement through QDs in series under the certain condition, rectified conduction coming from Pauli exclusion principle[5] can be observed. Selective spin transport deriving from Pauli spin exclusion principle through multi quantum dots is called Pauli spin blockade.

Basic transport model of Pauli spin blockade

One of the simplest systems of Pauli spin blockade is a double quantum dot, and the basic mechanism is explained[33] as follows.

In this dot system, no orbit degeneration and only spin degeneration is assumed under the sufficiently stronger quantum confinement effect than that of electron temperature. Consider the double dot consist with dot1 and dot2 with chemical

[5]The rule of that one orbital state can only be occupied by two electrons with different spin state

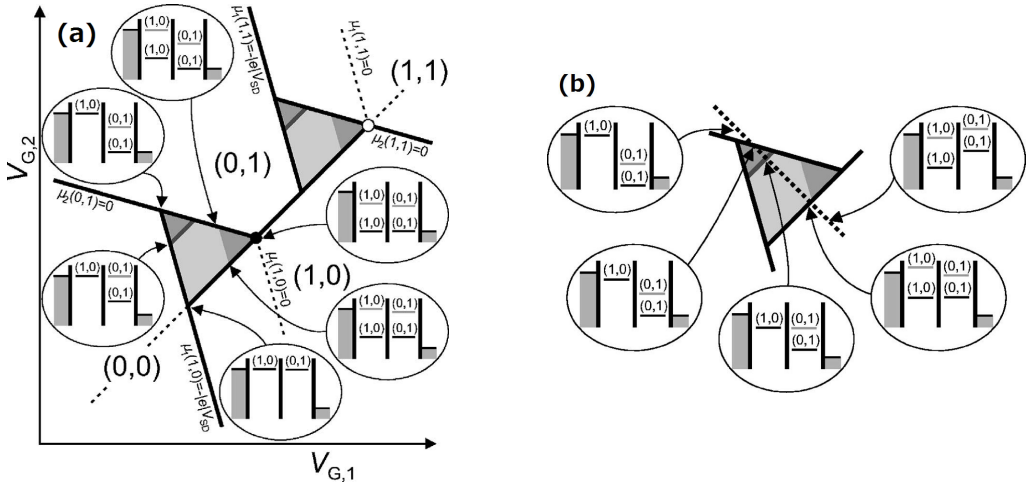

Fig. 1.3.5: (a) Drawings at the triple point under a finite source-drain bias. Within the triangles, charge transport thorough the dot is energetically allowed. Color contrast of gray and black shows current difference of current flowing through the dot. Gray lines correspond to excited-state levels. (b) Diagram of a bias triangle at the triple point for the single electron tunneling case detuning ϵ, and state levels for each dot (dot1 and dot2).

potential of μ_{N_1} and μ_{N_2} for the electron number N_1 and N_2 respectively. The electron number is noted like (N_1, N_2). The gate and bias voltage are tuned to realize the μ_{N_1}, μ_{N_2} and Fermi level like Fig. 1.4.2(a)[6] It is also assumed that energy levels of μ_{N_2} and μ_{N_2+1} are degenerated in the dot2 and that orbit levels are occupied up to μ_{N_1} and the upper different orbit level is filled for μ_{N_1+1}. The probable conduction cases are represented like below with chemical potential of each dots:

1 One electron moves from the lead to the dot1.
(μ_{N_1+1} and μ_{N_2})

2 The electron at the top level of orbit in the dot1 move to the dot2.
(μ_{N_1} and μ_{N_2+1})

[6]In this figure, the electrons which do not contribute to the dot current directly are dismissed. The simplest two electron system can be explained by substituting 0 and 1 in N_1 and N_2.

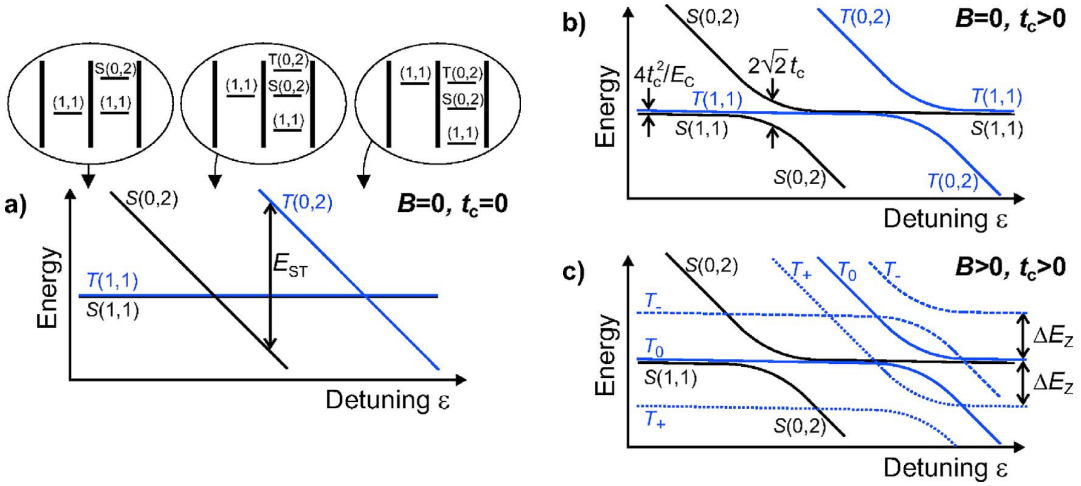

Fig. 1.3.6: Energy state of two electron spins in singlet ant triplet state confined in double quantum dots as a function of detuning ϵ for (a) $B = 0$ and negligible tunnel coupling t_c, (b) $B = 0$ and a significantly high t_c, and (c) non-zero B and significantly high t_c. The splitting energy ΔE_z correspond to the Zeeman energy.

3 The electron go through to the lead coupling with dot2.
(μ_{N_1} and μ_{N_2})

4 Back to the first step. (one electron moves into dot1)
(μ_{N_1+1} and μ_{N_2})

In the case of two electron system ($N_1 = 0$ and $N_2 = 1$), electron number under transport can be represented as (0,1) → (1,1) → (0,2) → (0,1).

The first demonstration of Pauli spin blockade is reported in a vertical double quantum dot system[55]. electron spin states and orbit in QDs can be observes.

Resonance tunnel / Spin blockade

Quantum dot transport characteristics during finite bias application is explained in Section 1.3.2, in which electron spin behavior, Pauli repulsive principle, is neglected. And, in the just previous section, simple model which explain the asymmetric current behavior for each bias so-called 'rectifying characteristics' under Pauli spin blockade condition is introduced. The rectifying characteristics of Pauli spin blockade can be also seen in the stability diagram plotted in dot current for double quantum dot

under bias. If reverse bias is applied for stability diagram shown in Fig. 1.3.5(b), bias triangle should appear in opposite direction in the case of without considering Pauli spin blockade. On the other hand, conduction through dot is forbidden in the most of triangle region under reverse bias in the case of with considering Pauli spin blockade.

The measurement examples reflecting on Pauli spin blockade are shown in Fig. 1.4.1 a) to d). In this measurement, the number of electrons in the quantum dot is counted up from zero electron utilizing the charge sensor method. The inverted triangle pattern reflecting symmetric $I - V$ characteristics appears for reverse bias around the transition region of the total electron number change as $0 \rightarrow 1$. In contrast to that, triangle pattern for reverse bias does not appear at the region of $1 \rightarrow 2$ due to the Pauli spin blockade.

Fig. 1.4.1 e) shows the diagram for convenience of electrochemical potential for two dots in the above situation. Circles filled with blue show electron charge state of the dots and the height of horizontal dotted lines correspond to position of chemical potential. At the side edge of the triangles in Fig. 1.4.1 d) ,one of which indicated by the mark of ★, dot current can be seen. Spin blockade is lifted in this region because (triplet) state in the left dot.

Fi.g.1.4.3 shows the triangle plotted by charge sensor in the MOS Si DQDs. The energy splitting of singlet and triplet for the dot bias was evaluated[31].

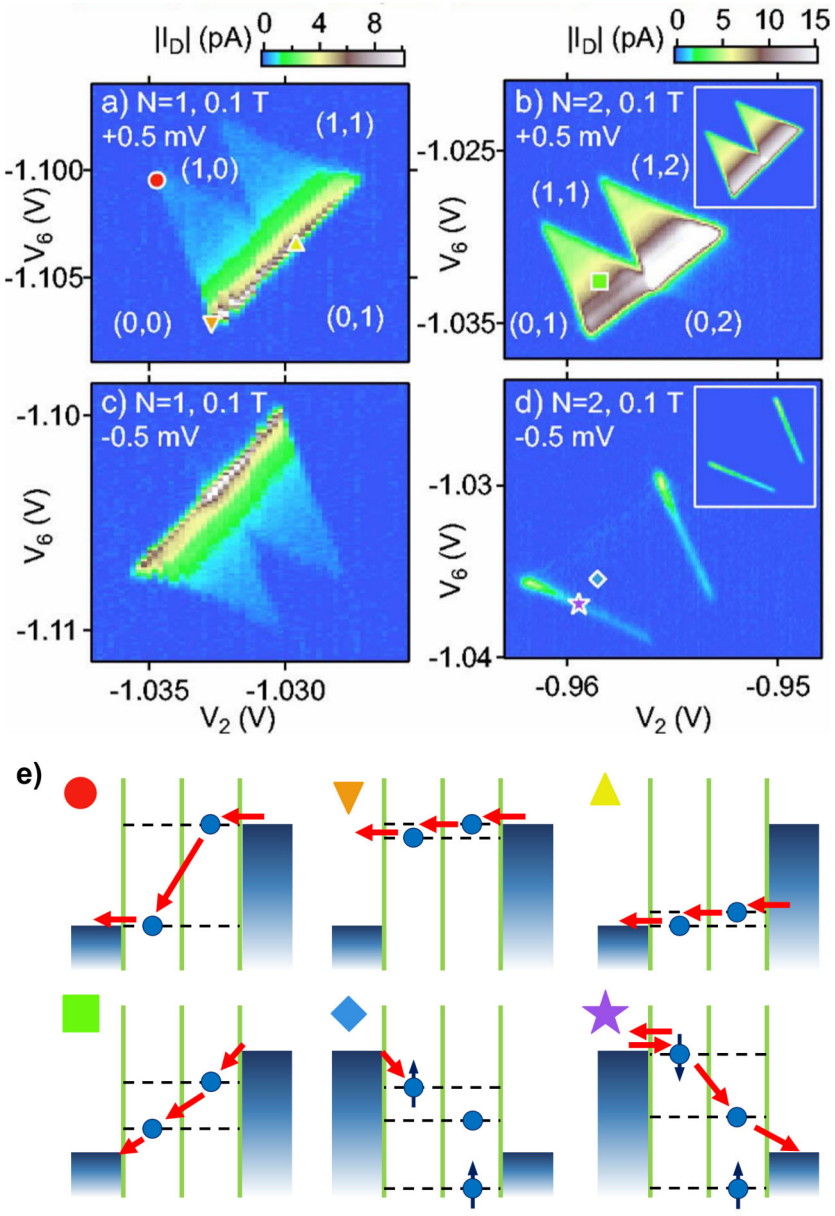

Fig. 1.4.1: Color plot against gate voltage V_2 and V_6 of the absolute dot current through the linear double quantum dot applied ±0.5 mV dot bias[31, 34]. a), c): Conduction when total electron number N in two dots change between 0 and 1. Inversion of dot bias V_{sd} causes symmetric bias triangle patterns. b), d): Conduction under the condition of N = 1 or 2 under the external in-plane magnetic field 0.1 T. Spin blockade is caused when voltage level of right dot connected to the earth is set between the two chemical potential levels deriving from the singlet state. Representative blockade point is shown as ◆ in Fig. (d).

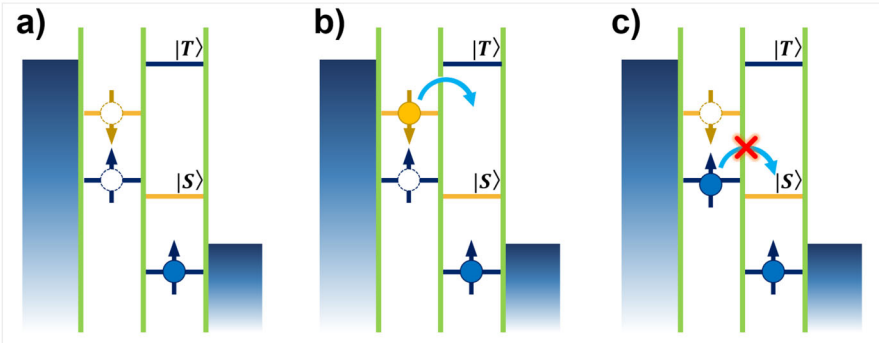

Fig. 1.4.2: Schematics of electrochemical potential considering singlet and triplet state in double dot[75]. a)Initial state as one electron occupied in the right dot, and each chemical potential levels are tuned. Panel b) and c) represents the different situations. Electrons conduction through the dot depends on the electron spin state which transits in the left dot. b)Down spin can go through from the left dot to the right dot and the lead. c)Up spin electrons are blocked due to Pauli repulsive by forming triplet state.

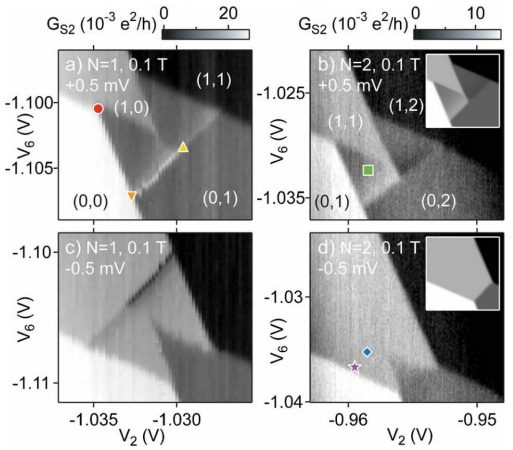

(a) GaAs double QD

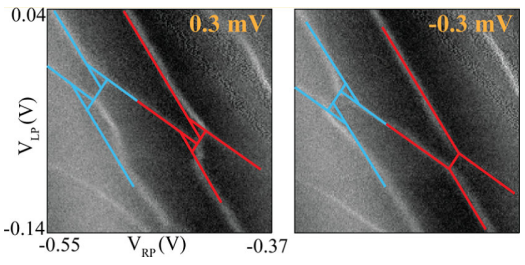

(b) MOS Si double QD

Fig. 1.4.3: Stability diagram at Pauli spin blockade region detected by charge sensor. Clear rectifying action is shown by the existence of a triangle[31].

1.5 Quantum State Conversion

In this section, I shortly summary the theory and early experiment about quantum state conversion using quantum well substrate.

1.5.1 Theory of Quantum State Conversion using Quantum Well Substrate

Vrijen and Yablonovitch proposed in 2001 the theory of superposition state transfer from photons to electron spins.

Optical selection rule and excitation preserving quantum state

In a valence band of GaAs, electrons have orbital angular momentum $L = 1$, and have all angular momentum $J = L+S = \frac{3}{2}$ by adding electron spin. Right circularly polarized photons σ^+ have angular momentum $+1$ and can excite electron spins to conduction band whose total z-component of angular momentum $m_j = -\frac{1}{2}$ from valence band, $m_j = -\frac{3}{2}$. It is possible to do such a selective optical excitation of electron spins in GaAs because of its band structure. This characteristic, however, is useless for transfer of superposition state. When you excite electron spins in GaAs by irradiating the superposition state of photons

$$|\phi_{\mathrm{ph}}\rangle = \alpha\,|\sigma^+\rangle + \beta\,|\sigma^-\rangle \tag{1.5.1}$$

and then each polarization states of photons access different excitation levels. As a result, the final state of hole-electron spin pairs excited by state in 1.5.1 is

$$|\psi\rangle_{\mathrm{eh}} = \alpha \left|m_j = -\frac{2}{3}\right\rangle_{\mathrm{h}} \otimes \left|m_j = -\frac{1}{2}\right\rangle_{\mathrm{e}} + \beta \left|m_j = \frac{2}{3}\right\rangle_{\mathrm{h}} \otimes \left|m_j = \frac{1}{2}\right\rangle_{\mathrm{e}} \tag{1.5.2}$$

This shows that electron spin states and hole spin states are entangled with each other. This excitation process is desirable for application of quantum state because both state of electron spins and hole spins must be preserved to sustain the superposition state of photons. Even if one of the spins of electrons or holes lose coherent state [7] , then you can get the eigen state of only one of two term in (1.5.2) , and

[7] It is said that hole spin state relax soon because hole has strong interaction with the outer environment

destroy the superposition state of (1.5.1).

All information must be removed from hole spins to prevent this decoherence. Details of lift the entanglement between electron spin and hole spin is explained in next section.

Excitation of Zeeman levels of light hole under in-plane field

Light hole state and heavy hole state degenerate around Γ point in bulk GaAs. However, the degeneracy lifts in quantum well structure by confinement effect. The narrower well width generate the bigger energy splitting between heavy hole and light hole. So you can excite the hole state selectively, light hole or heavy hole, each of which have different angular momentum, then more pure polarized electron spins can be induced by optical pumping in quantum well.

Light hole levels show Zeeman split states under in-plane field due to non-zero g-factor.

$$|\psi^+\rangle = \frac{1}{\sqrt{2}}\left\{ \left| m_s = -\frac{1}{2} \right\rangle + \left| m_s = \frac{1}{2} \right\rangle \right\} \tag{1.5.3}$$

$$|\psi^-\rangle = \frac{1}{\sqrt{2}}\left\{ \left| m_s = -\frac{1}{2} \right\rangle - \left| m_s = \frac{1}{2} \right\rangle \right\} \tag{1.5.4}$$

If you excite $|\psi^+\rangle$ selectively as a first state, one of the basis of polarization state of photons $|\sigma^+\rangle$ can provide angular momentum $L = +1$ to $m_s = -\frac{1}{2}$, and the other basis $|\sigma^-\rangle$ can provide $L = -1$ to $m_s = \frac{1}{2}$. Moreover, if electron g-factor in conduction band is as small as you cannot distinguish Zeeman states in energy by irradiated laser spectrum width, $|\sigma^+\rangle$ can access both of Zeeman splitted electron states from $|\psi^+\rangle$.

As in the previous subsection, preparing the superposition state photon

$$|\phi_{\mathrm{ph}}\rangle = \alpha\,|\sigma^+\rangle + \beta\,|\sigma^-\rangle \tag{1.5.1}$$

, and if you excite the first state $|\psi^+\rangle$,

$$\begin{aligned} |\psi\rangle_{eh} &= \alpha\,|\psi^+\rangle_h \otimes \left| m_s = -\frac{1}{2} \right\rangle_e + \beta\,|\psi^+\rangle_h \otimes \left| m_s = \frac{1}{2} \right\rangle_e \\ &= |\psi^+\rangle_h \otimes \{\, \frac{\alpha}{\sqrt{2}}(\,|\,0\rangle + \,|\,1\rangle) + \frac{\beta}{\sqrt{2}}(\,|\,0\rangle - \,|\,1\rangle)\,\}_e \end{aligned} \tag{1.5.5}$$

then entanglement between hole spin and electron spin lifts like above. I notate the electron spin state;

$$|0\rangle = \sqrt{\frac{1}{2}}\{\ |\ m_s = -\frac{1}{2}\rangle - \ |\ m_s = \frac{1}{2}\rangle\ \} \tag{1.5.6}$$

$$|1\rangle = \sqrt{\frac{1}{2}}\{\ |\ m_s = -\frac{1}{2}\rangle + \ |\ m_s = \frac{1}{2}\rangle\ \} \tag{1.5.7}$$

Confined electron wave functions in the GaAs well layer interacts with the AlGaAs barrier layer, allowing engineering of the electron g-factor[24] by control the GaAs well width. As a result, this quantum state conversion scheme from photons to electron spins in quantum well becomes feasible. In the case of using a heavy hole, hole g-factors for in-plane magnetic field in a quantum well substrate grown in [001] crystalline direction, which is conventional crystal alignment, is almost zero. It becomes impossible to demonstrate the above mentioned conversion.

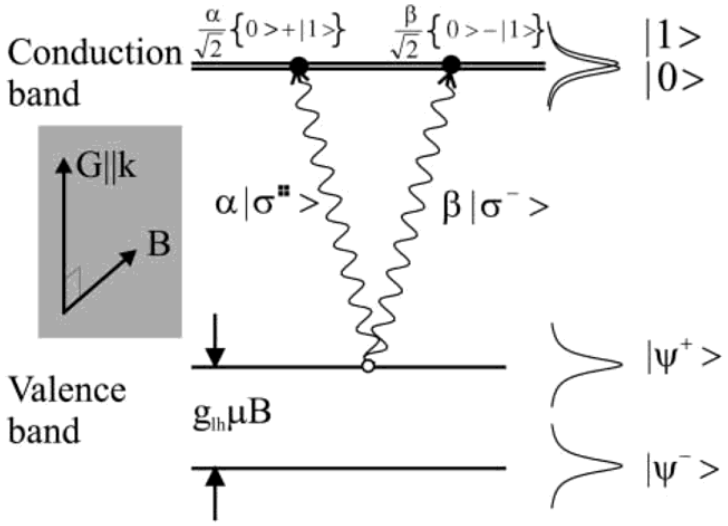

Fig. 1.5.1: The excitation of a coherent superposition state of conduction band spin states after an absorption of a photon in an identical superposition of polarization states. This figure is cited from [73].

1.5.2 Quantum State Transfer in an Ensemble

The theory of the quantum state transfer suggested by Vrijen and Yablonovitch was demonstrated by a time resolved Kerr rotation(TRKR). Fig. 1.5.2 shows the

experiment results on GaAs/AlGaAs (001) quantum well[40]. Ensemble spins were excited by a laser as an ensemble photons satisfying the conditions of the preservation of quantum superposition state. Circularly or linearly polarized pump laser was irradiated on the substrate, and the Larmor precession of polarization basis of the probe laser, giving information of the initial spin state upon irradiation[8]. External magnetic field was applied 7 T in a direction parallel to the H-polarization. The quantum well is designed such that the electron g-factor in the well is small enough for satisfying the quantum state transfer, which means that the energy spectrum of the excitation laser is larger than the Zeeman splitting energy of the electrons, but the g-factor value is not completely zero(g=0.2) used to measure the spin state coherence. Electron spin Larmar precession is shown in Fig. 1.5.2(c) for the light hole excitation, and Fig. 1.5.2(e) for heavy hole excitation.

Oscillation signals with maximum amplitude can be seen when electrons are excited with circular polarization light in the both cases, which correspond to the spin polarized excitation with the angular momentum conservation, same as the traditional optical experiments. On the other hand, only in case of light hole excitation, oscillation behavior with a $\pi/2$ phase shift compared to above can be observed when electrons are excited with linearly polarized light such as D^+/D^-, which means that the linearly polarization light, superposition state of σ^+ and σ^- is projected on the electron spin state conserving the superposition information.

However, electrons excited with heavy hole have no such oscillation (Fig. 1.5.2(e)) in short no electron spin polarization is detected, which indicates that the superposition state in the basis of σ^+ and σ^- is lost during the optical excitation. This is because the heavy hole in (001) quantum wells have almost zero g-factor. The experimental result suggests that the hole spin states with no Zeeman splitting excites electron spins entangled with holes, as a result, causing electron spin relaxation predicted from theory.

[8]Based on Polar Kerr effect, magnetization or electron spin distribution within the optical penetration depth.

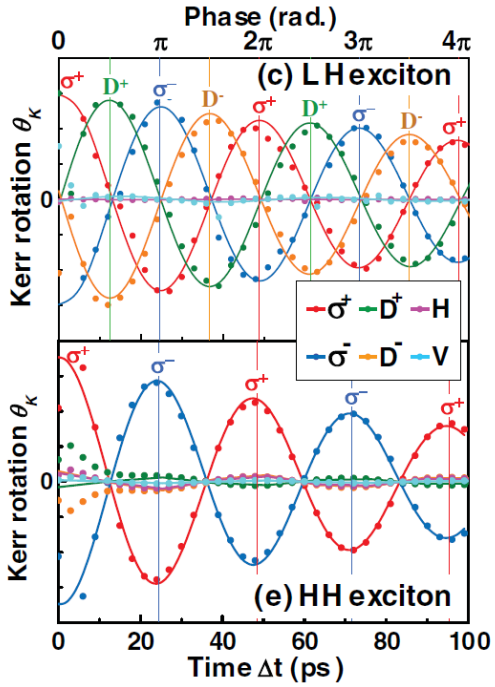

Fig. 1.5.2: Time resolved Kerr rotation of electron spin excited as quantum state transfer.

1.5.3 Single Photon and Single Electron Spin Interface

Quantum state conversion between single photons and single electron spins not in an ensemble is an essential technology to consist in a quantum repeater. Spin polarized transfer in other words angular momentum transfer between single photons and electrons is demonstrated in experiments[20].

Single electron spin detection

Double lateral quantum dot as Fig. 1.5.3 formed on GaAs/AlGaAs quantum well is used to detect the single electron spin. In double quantum dot, confinement potential areas are coupled with each other with some degree of tunneling rate which can generally be tuned by plunger gate voltage. Electrons can quickly hop between them as

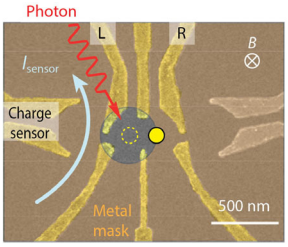

Fig. 1.5.3: SEM image of lateral quantum dot[20]

resonance transition when chemical potential is tuned at the same level, and then the electron exit to the reservoir probabilistically. Additionally, under perpendicular external magnetic field, electron spin state can be detected by Pauli spin blockade by tuning the other dot energy as electron spin state in up spin state in energetically low. When single electron spin excited at the receiver dot (left dot in Fig. 1.5.3), transition probability is much different on the excited spin state by Pauli spin blockade. That behavior can be sensitively detected charge sensor near the dot. This is the technique to detect the single electron spin state excited electron spin.

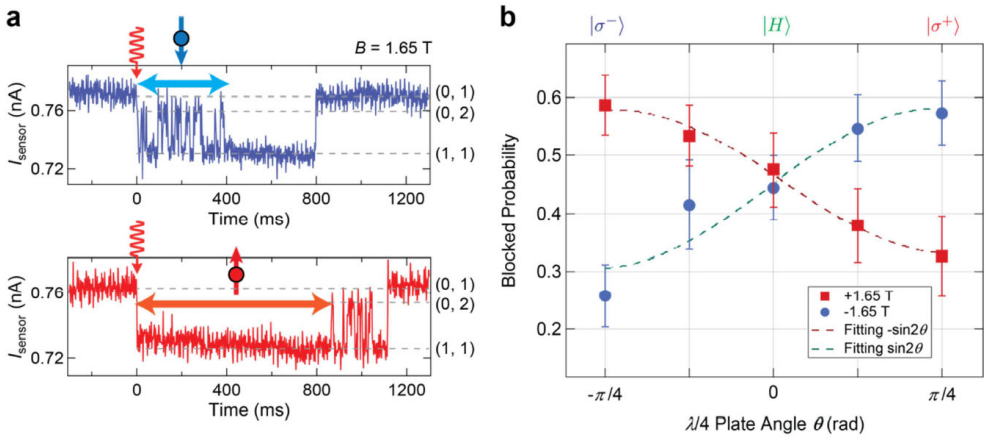

Fig. 1.5.4: The probability of parallel spin detection.[20] Horizontal axis is the exciting photon polarization state.

Base on the technique of single electron spin detection, excited electron spin state is estimated statistically. Blocking electron spin is hold as up state at right dot under polarized under perpendicular magnetic field as 1.65 T. Clear correspondence between photon polarization and electron spin polarization can be seen. However, the fact must be emphasized that heavy hole level is excited in this experiment and only angular momentum not superposition state of photon polarization is converted into electron state. The distribution can be fitted with sine curve, and symmetric structure for polarization angle of exciting photons.

Chapter 2

(110) Quantum Well Design and Characterizations

2.1 Quantum State Conversion using (110) substrates

The theoretical proposal of quantum state conversion is explained in section 1.5 by following the original paper. Some basic conditions are required for quantum state conversion: (I) Zeeman splitting of hole state (II) indistinguishable Zeeman splitting energy of the electron spin respect to the laser spectrum, (III) the QW along the in-plane external magnetic field. It is well known that the electron g-factor value can be tuned by engineering the QW structure such as by well width and the ratio of GaAs and AlAs in the barrier layers[65, 24]. Meanwhile, only the light hole has a finite g-factor for an in-plane magnetic field, while the heavy hole has almost zero value in traditional (001) QW . Therefore, the light hole ,although having a smaller state density, is discussed in the theoretical paper[73]. However, the situation can be different in QWs grown in the (110) crystal orientation.

Concept of coherent transfer

To discuss the implications for (110) QWs, the coherent transfer is described again but in a more intuitive way. Photon polarizations are spin-1 quantum states, and

the z component of the spin angular momentum takes $S_z = -1, 0, 1$. However, since there is no longitudinal wave component of $S_z = 0$ in vacuum, the photon can describe its polarization state by a two-level system. When this polarization state is described by Stokes parameter coordinates, it is the Poincaré sphere visually expresses this vector space in an easy-to-understand manner. On the other hand, the electron spin is originally a two-level system, and its state is represented by the Bloch sphere. However, the status must be pure in order to express the state on the surface of this sphere. At this point, the Poincaré sphere and the Bloch sphere can be treated equivalently mathematically. In other words, the above-mentioned state transfer from light to electrons ideally realizes a unitary transformation between the SU(2) state spaces (Fig. 2.1.1).

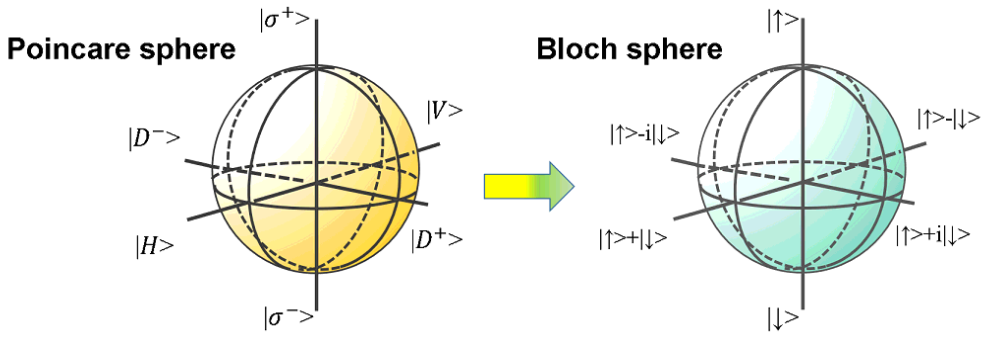

Fig. 2.1.1: The correspondence of quantum state between photon polarization state and electron spin state.

The energy of a photon is always constant regardless of its polarization state. In order to convert this state into an electron spin state, the electron spin must also have the same energy. However, a magnetic field must be applied to define the spin phase[1]. Therefore, it is necessary to prevent energy differences from occurring due to Zeeman splitting. This is the reason why the electron spin g-factor is required to be small. On the other hand, with respect to holes, in the absence of a magnetic field, that is, without Zeeman splitting, electron spins and holes excited by photons in the polarization-superposed state become entangled and lose quantum coherence due to

[1]By applying a magnetic field, a stationary electron can define the spin orientation with respect to the direction of the magnetic field, and accordingly the phase can be defined.

the rapid relaxation of the hole spin state. Therefore, the holes are split by Zeeman splitting by applying an in-plane magnetic field. At this condition, the holes form a mixed ground state called a bonding state and an antibonding state. This state allows electrons to transition to both up-spin and down-spin. Therefore, when one hole is selectively excited by light in a state of superimposed polarization, a direct product state of electrons and holes is generated, and entanglement between holes and electron spins can be removed. This results in the preservation of the quantum phase during the photon-to-electron transfer. The problem is the Zeeman splitting of holes, but heavy holes do not split due to the symmetry of the wavefunction in the quantum well substrate. However, it is expected that even heavy holes can be split in quantum well substrates with a broken symmetry (110) growth direction.

In summary, in order to transfer the photon state of the two-level system, which is the basis of the polarization state, to the two-level system of electron spins, including the quantum coherence, that is, the superposition state, it is necessary to focus only on the energy conservation and electron spins. Therefore, it is necessary to control the Zeeman splitting width of each level.

1. The g factor for the in-plane magnetic field of heavy holes in the valence band is sufficiently large.

2. Sufficiently small g factor for the in-plane magnetic field of electrons in the conduction band [2].

Coherent transfer exciting heavy hole

Light hole in (001) QWs satisfies the condition of coherent transfer. However, as is well known in the field of semiconductor optical physics, the excitation efficiency of light holes is about one-third of that of heavy holes due to the difference in density of states. It has been confirmed experimentally that the difference of excitation efficiency is also seen in the case of single-electron excitation by single photons as shown in Fig. 2.1.2. Therefore, if heavy holes can be used for quantum state conversion, it is expected to improve the theoretical limit of absorption efficiency.

[2] "Sufficiently large (small)" means a state that is large (small) relative to the linewidth of the laser, that is, a state in which the energy levels of Zeeman-split up-spin and down-spin can be distinguished (not) when viewed from the laser.

Winkler suggested the high anisotropy of heavy hole g-factor in GaAs quantum wells[78]. Dependence of in-plane g-factor of heavy holes in GaAs QWs is also shown experimentally[22], which demonstrates the theoretical proposal. From the results, QWs grown in (110) crystal orientation has finite heavy hole g-factor against in-plane magnetic field. In other words, appropriately designed (110) substrates, including the well width, will enable excitation in the manner shown in Fig. 2.1.3, leading to the realization of highly efficient quantum state transitions.

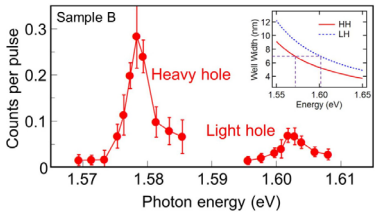

Fig. 2.1.2: Photon counting probability in exciting heavy hole and light hole[49].

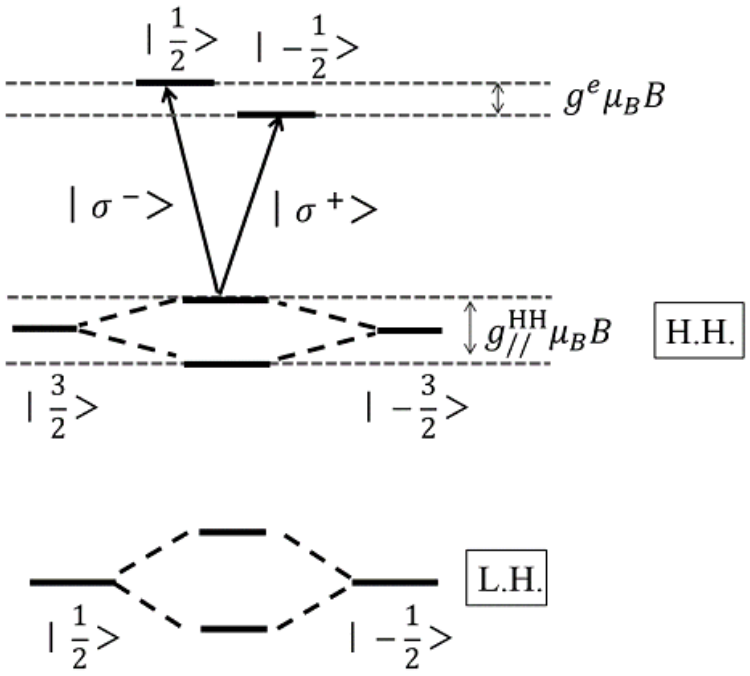

Fig. 2.1.3: The excitation of a coherent superposition of conduction band using heavy hole spin states, after absorption of a photon in an identical superposition of polarization states. Finite hole g-factor induce the Zeeman splitting of the hole spin state, which enable the excitation of the superposition of an electron spin.

2.2 Substrate Layer Design

In advance of experiments with (110) QWs, we started with the design of the substrate structure.

At the first experiment, we requested the growth of a substrate with a well width of 7.5 nm for the purpose of minimizing the g-factor of electrons, and started evaluation. It was confirmed to have a small g-factor by time-resolved Kerr rotation measurements. However, it has been difficult to fabricate stable devices for exploring low-dimensional physics. Moreover the lack of accumulation of knowledge on growth recipes in molecular-beam epitaxy made it difficult to obtain good quality substrates.

Reflecting on the results, we re-designed the substrate structure for the experiment this time. Complete demonstration of quantum state conversion requires tomography measurements of excited electron spins. This requires electron spin state manipulation such as ESR[36], which is difficult if the electron g-factor is too small. We decided to widen the well width so that the g-factor of electrons becomes large within the range that satisfies the conditions of quantum state conversion. We considered the fact that the 2DEG layer felt a larger interface fluctuation due to the narrow well width was one of the factors that reduced the electron mobility. Based on previous research[29, 22], we decided to widen the well width to 12 nm, where the electron g-factor is less than 0.2 and the hole g-factor is about 0.4.

Growth conditions

Designed well structure is shown in Fig. 2.2.1. The (110) QW was grown and provided from a joint research institute of Ruhr-Universität Bochum, Germany. We conveyed information of the desired structure such as width and depth of the QW layer, and detailed growth conditions are optimized by members of Ruhr University Bochum.

Each layer is grown at 515 °C and 6.0×10^{-8} torr. GaAs and AlAs layers are repeatedly grown to enhance the morphology of the inter-facial layer that forms the channel. The GaAs well layer 12 nm is sandwiched with barrier layers of $Al_{0.33}Ga_{0.67}As$. A doped layer, $Al_{0.33}Ga_{0.67}As$:Si is grown close to the surface.

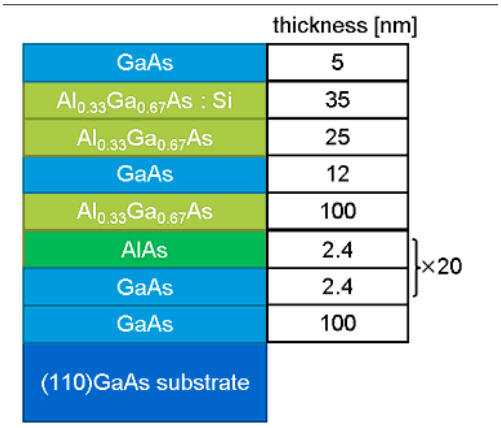

Fig. 2.2.1: Substrate layer information. The thin film layers are grown on a (110) GaAs substrate.

A typical (001) substrate has cleavage planes in the perpendicular direction, but in the case of (110) substrates, the cleavage planes are oriented at 60 degrees to each other. It was reported that the optimum deposition temperature for obtaining good quality (110) QW layers was different from that for (001)[30].

Around the edge of the board we got this time, there was lines running diagonally at 60 degrees that could be seen with the naked eye. We cut out chips from around center of the wafers not to include the lines into the conduction path of the QD devices.

2.3 Evaluation by Quantum Hall Effect

As mentioned in Section 1.1.3, the quality of 2DEG electron transport can be evaluated by the Hall measurements. MESA pattern of the Hall bar is fabricated by dilute sulfuric acid etching, and the size of measurement area is designed as 70 μm $\times$ 210 μm and the ohmic contacts are annealed at 450 °C. Figure 2.3.1 shows the result of the Hall measurement. Generally, a mobility about 100 times larger is expected for evaluation measurements of ballistic conduction.

The fridge in this measurement has an optical window, and the light that can excite carriers can be guided to the sample from room temperature. Since light was

irradiated during the measurement, the induction of persistent photo-carriers was confirmed.

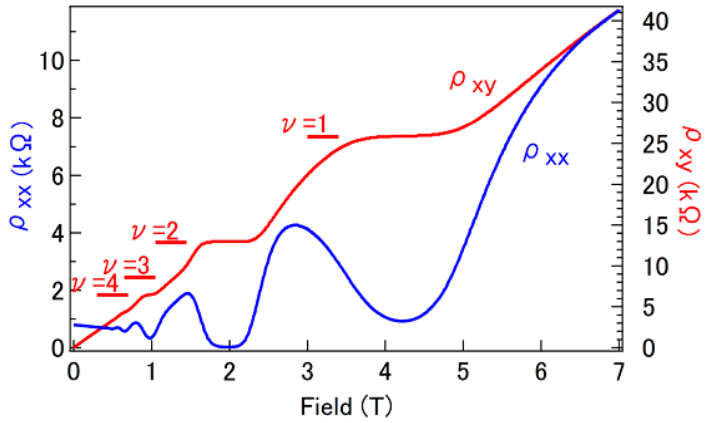

Fig. 2.3.1: Quantum Hall effect characteristics of the (110)-oriented GaAs QW with 12 nm width. The longitudinal resistivity (ρ_{xx}) and the transverse resistivity (ρ_{xy}) are measured in the dark at 1.5 K. ρ_{xx} at 0 T is 790 Ω. The carrier density and mobility, respectively, are $9.3 \times 10^{10}\,\mathrm{cm}^{-2}$ and $8.5 \times 10^{4}\,\mathrm{cm}^2/\mathrm{V}\cdot\mathrm{s}$.

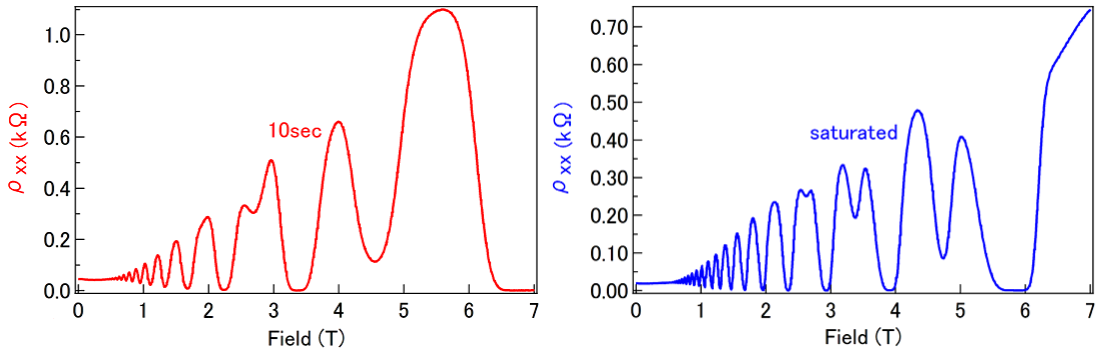

(a) Illumination for 10 sec.

(b) Illumination for long time.

Fig. 2.3.2: Quantum Hall effect characteristics after illumination. Ambient light is illuminated to the sample by just opening the optical window of the fridge. The window was closed during measurement. The carrier density is $3.2 \times 10^{11}\,\mathrm{cm}^{-2}$ after 10 sec illumination, and $5.6 \times 10^{11}\,\mathrm{cm}^{-2}$ after long time illumination until the density saturation.

Chapter 3

Quantum Dot Formation in (110) quantum wells

Purpose of the Experiment

Here, we would like to refer the purpose of the experiment in this chapter.

One of the solutions to enhance the efficiency of photon polarization to electron spin quantum state conversion is to utilize the heavy hole state which is not available in (001) QWs for the quantum state conversion. In a (110) QWs, the non-zero heavy hole g-factor is expected to contribute to the heavy-hole spin splitting. In order to realize the elemental technologies for photon-spin quantum state conversion using (110) QWs, we have to follow the steps of experiments established in (001) QWs.

On the other hand, studies on (110) QWs have focused on experimental and theoretical aspects of in-plane anisotropic g-factor and long spin relaxation times in QWs because of the suppression of D'yakonov Perel mechanism. Thus, no micro device fabrication technology has been fully applied to the (110) substrate, and the physics of the zero-dimensional confinement of electrons or holes has not been investigated sufficiently in experiments to the best of our knowledge.

To open the path for photon-spin quantum state conversion, we have to demonstrate several steps by following the achievements in gate-defined QDs formed in a (001) QW. The outline of the steps is discussed below:

1. Quantum dot formation

Following the basic evaluation of (110) QWs, an appropriate gate-electrode design of QDs is needed to construct working devices for a cryogenic environment. Then, the QD devices are fabricated with an established recipe following that for conventional GaAs gate-defined quantum devices. Of course, constructing the measurement set up is also very important. The formation of single and multiple QDs is examined at low temperatures.

2. Real-time measurements of dot states

   Dot current can show the zero-dimensional confinement of electrons, but this type of detection is not sufficient to detect the dynamics of single quantum states in the dots. Controlling the number of electrons in the few-electron region and real time detection of the quantum state are critical techniques also for photon-spin quantum state conversion experiments. First, detection and counting of the electron number in QDs in single-electron or few-electron number regimes has to be achieved using a charge sensor. Developing this measurement technology enables us to monitor the energy levels in the dots in real-time.

3. Electron spin state detection

   The detection of not only the electron number but also the electron spin state is very useful. Basically, repeated measurements of single electron spin state with different measurement bases can provide the spin state tomography. There are some type of state detection such as Elzermann readout and Pauli spin blockade (PSB). PSB is the candidate for real-time measurement. In this paper, PSB transport through double QDs and electron spin states in (110) QWs is discussed.

4. Device operation with a photo-mask

   A QD device has many constituent parts: the confinement space, the reservoirs, the charge sensor, and so on. Primarily, the electron spin excited in the dot space should be detected, but photons can also be absorbed in the area surrounding the QD and this could hinder the stability of the target QD and the sensor QD. Carriers or ionized impurities generated at the sensor or

unintended area could cause problems for accurate detection. A metal cover with a center aperture just above the dot can suppress the unintended photon illumination in the device except at the target QD. The top gate on the insulator with a small aperture is called a photo-mask[1]. The details of this structure are mentioned in chapter4.

5. Photon illumination on dot region

   Photon illumination system is one of the required measurement setup for the photon-spin quantum state conversion experiments. However, the free-space injection method has an inherent difficulty in the alignment between an objective lens and the QD at low temperature. As a result, the spot size unavoidably becomes large compared to the dot size or aperture size of the photo-mask, which strongly reduces the conversion efficiency. In addition, the misalignment of the spot position and the sample tilt for the laser incident reduces the transmission of photons to the QD.

   Laser light guided into the fridge with fibers and micro lenses can reduce the spot size significantly. A practical interface between laser light and semiconductor devices should be constructed with such a design.

Points 4 and 5 are disucssed in chapter5.

3.1 Device Design and Fabrication

As mentioned in Sec.1.3, lateral quantum dots (QDs) are formed by lateral confinement of a two dimensional electron gas (2DEG). The confinement potential is established by electric fields formed by nano-scale Schottky electrodes deposited on the surface of the substrate. The field area can be tuned by voltages applied to each electrode, but the design of the Schottky gate electrodes is very important to form a proper confinement potential. Moreover, the gap between the electrode, which usually works as a tunnel barrier must be designed in order to adjust the tunnel coupling between the confined electrons and the reservoir.

[1]This is not the same as the photo-mask in photo lithography used to transfer the micro patterns onto wafers.

Compared with the high mobility 2DEG in (001) substrate widely used for GaAs QDs, (110) QWs tend to have a lower mobility as shown in chapter2.

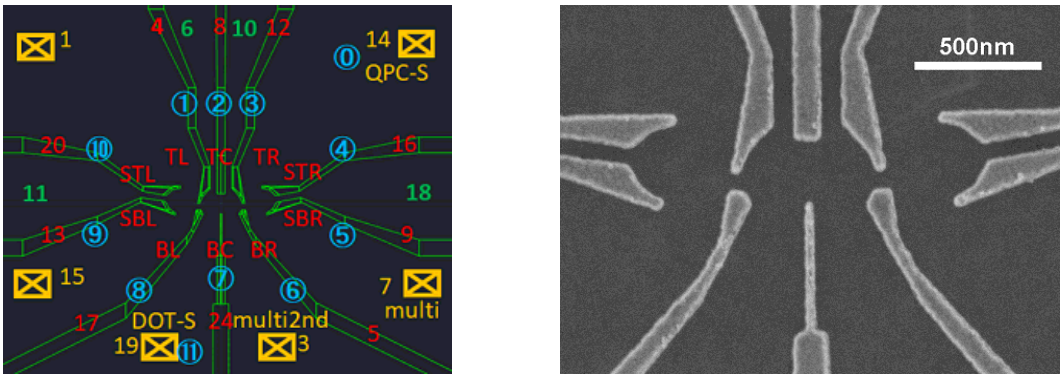

(a) CAD image of the gate pattern. (b) SEM image of the gate pattern.

Fig. 3.1.1: (a) CAD design patterns for the metal gates. The name of each gate is indicated by red letters. (b) SEM image of the gate pattern.

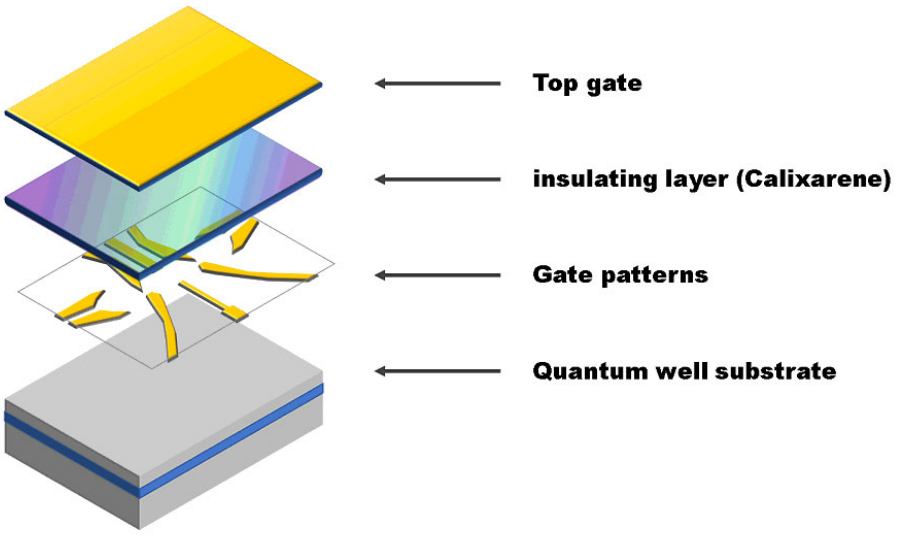

Fig. 3.1.2: Schematic figure of the device structure.

3.2 Measurement Setup

We set-up a new dilution fridge, and the wire lines and filter components are fabricated by ourselves.

3.2.1 Cold Finger

Figure 3.2.1 shows the cold finger and noise filter components constructed by ourselves. The cold finger is made of oxygen-free copper which has a higher thermal conductivity than normal copper especially at low temperature, which can fully conduct the cooling capacity of the MXC plate cooled down to less than 10mK. The large bulk structure of Cu induces eddy currents which can generate heat in the metal when the magnetic field is swept, but cools back when it is at a steady state. Components of the filter and device wires are connected with Cu wires covered by a metal mesh. The RC filter is set as a low-pass filter designed with resistive and capacitance elements selected for purpose depending on the gate electrodes.

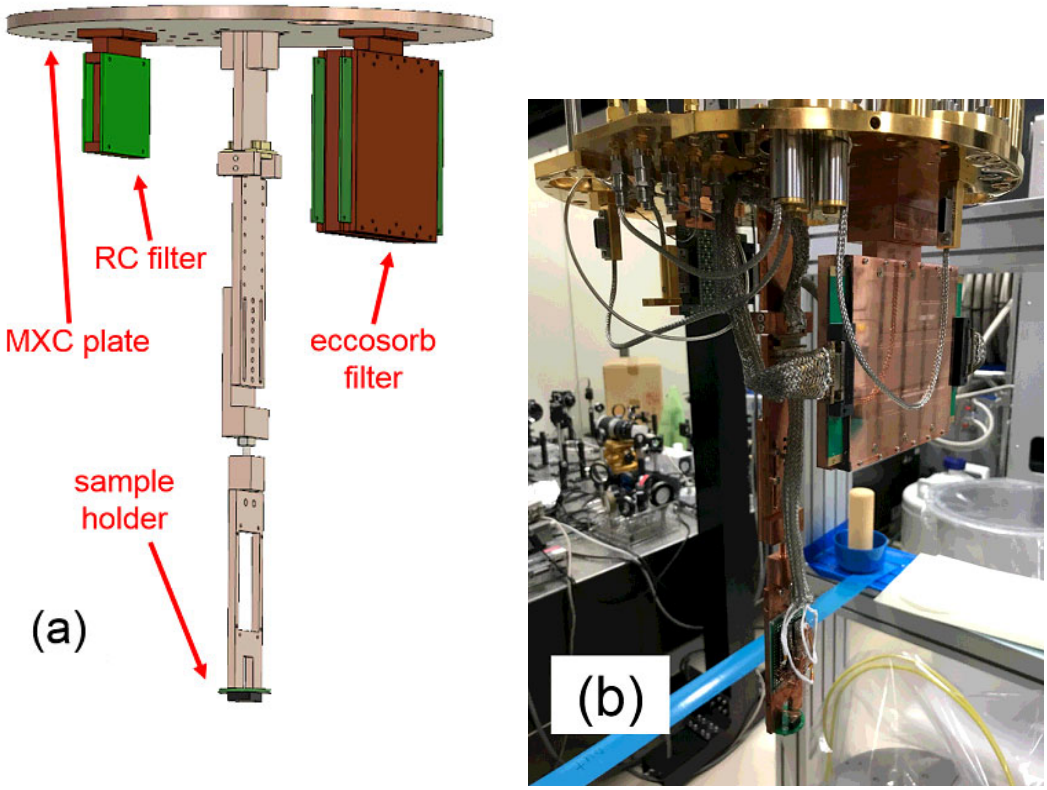

Fig. 3.2.1: (a) 3D CAD design of the cold finger. (b) Photograph of the cold finger attached to the mixing plate of the fridge.

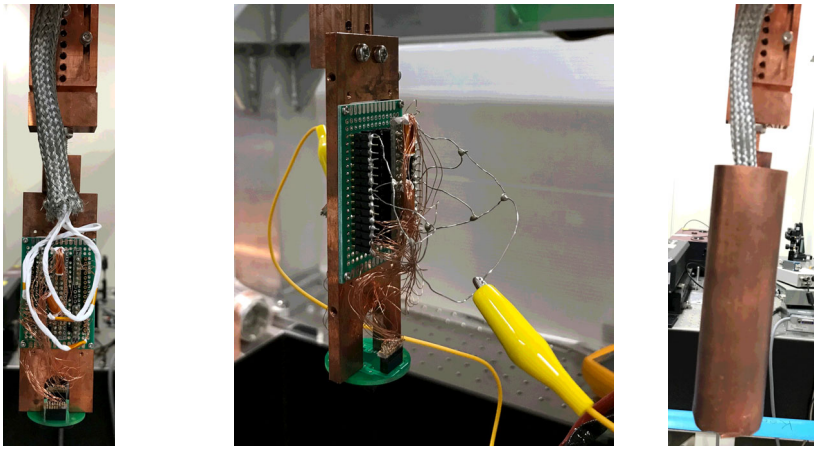

(a) Front side. (b) Sample on GND. (c) covered sample.

Fig. 3.2.2: Cold finger CAD design and photograph.

3.2.2 Low Pass Filter

Eccosorb filter

ECCOSORB® is a commercial product which is used for absorbers, attenuators, and terminations of waveguides and coaxial lines. It is designed for high-loss microwave absorbers, and enables the conversion of RF energy into heat. A simple RF filter can be constructed just by covering the wiring line with this product. Eccosorb® is supplied as a two-component product consisting of resin and catalyst. The two components are mixed together in a beaker and heated by a hot plate just before pouring into the filter box. In order to increase the thermal conductivity of the mixture, it is placed in a vacuum vessel and oxygen is removed. The meander line structure is designed following Ref. [68].

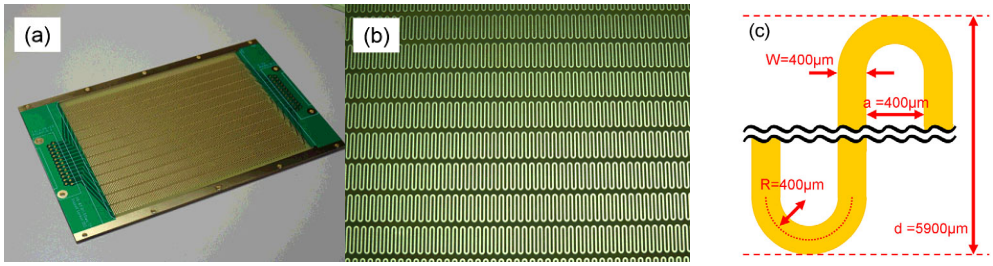

Fig. 3.2.3: Pictures of meander PCB. (a)Picture of whole PCB (b)Enlarged meander pattern (c)Design of meander pattern.

RC filter

In order to adjust the threshold and rise time in the desired way, the RC components are connected in series with two stages. The special PCB for RC elements bonding is designed by ourselves using CAD software and its manufacture is outsourced. The R_1 and C_1 elements in the first stage and the R_2 and C_2 elements in the second stage are selected respectevely as, $R_1 = 1\,\mathrm{k}\Omega$, $C_1 = 1\,\mathrm{nF}$, $R_1 = 1\,\mathrm{k}\Omega$, and $C_1 = 1\,\mathrm{nF}$ (fc =159 kHz) for the gate lines, and $R_1 = 200\,\Omega$, C_1 = NO, $R_1 = 200\,\Omega$, and C_1=100 pF (fc =4 MHz) for the ohmic lines.

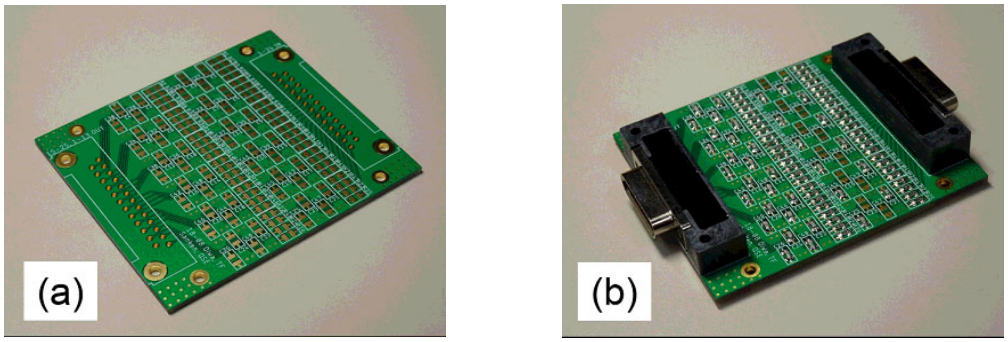

(a) PCB before RC mounting. (b) RC filter after assembly.

Fig. 3.2.4: Pictures of PCBs for RC filters.

3.3 QD Formation in (110) QWs

The device configuration and measurement setup are explained in the previous sections. Now the electrical measurements of the QD device are described.

After cooling to 4K, the first test of the device state is to check the quantum point contact (QPC) behavior for each pair of electrodes. The fabrication recipe has been established through many trials on dummy wafers and a part of the real (110) wafers. SEM imaging of the fine gate electrode patterns and QPC measurement with a simple electrode structure have been done before introducing the QD device in this experiment. We have therefore improved the yield of the device fabrication, but sometimes unavoidable problems arise with the chip. For example, floating electrodes or electrodes peeling off are often observed and caused by resist residue. Similar problems on the gate electrodes can happened if nitrogen gas blowing during the fabrication is too strong. Low adhesion of metal patterns prevents the application of the desired electric field to the 2DEG and so we cannot control the electron population or distribution over the 2DEG sheet. Electrode explosion[2] by electrostatic discharge can happen during the wire bonding step and final attachment of the device mounted on PCB to the cold finger. Since the distance between the patterns is sometimes less than 100 nm, a huge instantaneous electric field can be generated there which can damage the fine patterns and 2DEG beneath. The similar pinch-off voltages are expected when the QPC is formed between electrodes

[2]It is not an exaggeration. After the explosion, the electrode metal looks like a splash of liquid.

with the same gap designed.

3.3.1 Quantum Dot Operation in the Many-Electron Region

The QPC works properly at 4K during the first test, and then the mixing chamber is cooled down to less than 10 mK for the QD operation. The first working device did not provided information of voltage on each electrode.

The pinch-off voltage of the QPCs is the most informative data for forming QDs. In the QD operation, the confinement potential in the dot region defines the energy levels and tunnel barriers. However it is very difficult to detect the exact electron number confined in the QD directly. Transport though the QD and changes in the number of electrons offer information about the energy states in the QD. Therefore, the gate voltages have to be tuned to give the appropriate coupling between the dot and the reservoir to give finite conductivity through the QDs.

As the gate voltages applied to the QPC gate electrodes change, the QPC current in a high mobility substrate shows plateaus with a height matching to $2e^2/h$ reflecting the sub-band structure formed in one-dimensional conductors. This is a signature of low-scattering transport of electrons, and the gate voltage at the onset of the first plateau gives the set points for the charge sensing.

In the (110) QW used in this experiment, no clear plateau could be seen in the QPC measurements due to the electron scattering in the 2DEG with a mobility of $8.5 \times 10^4 (\mathrm{cm}^2/\mathrm{V} \cdot \mathrm{s})$. We set the gate voltage of the barrier potential in the vicinity of the pinch-off voltage where the electrical current drops off.

A charge stability diagram measured by the dot current is shown in Fig. 3.3.1. Even though the center gate voltage was tuned to a relatively small voltage to form a single quantum dot in the central region, the diagram shows a honeycomb pattern indicating the formation of an unexpected double quantum dot with very strong coupling between the two QDs. This suggests that unexpected potentials are created in the dot area without applying an intentional electric field to the surface electrodes.

Figure 3.3.1b is the diagram after applying a positive voltage on the plunger

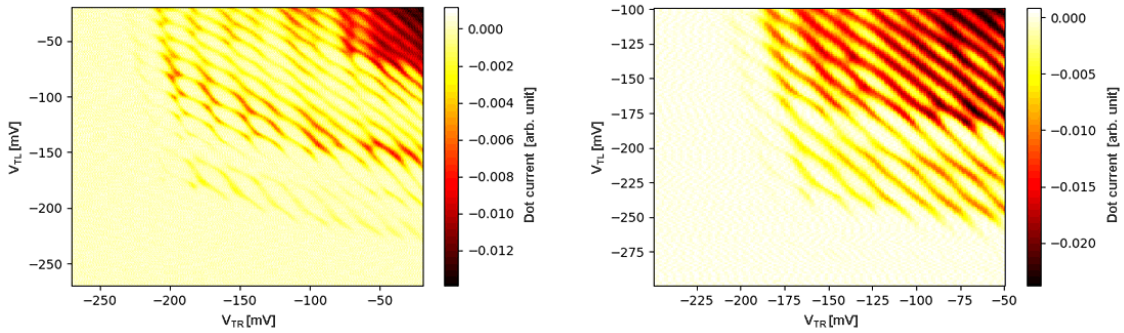

(a) Negative plunger gate.

(b) Positive plunger gate.

Fig. 3.3.1: Charge stability diagram by dot transport.

gate. Intuitively, positive voltages on the electrodes should weaken the confinement. However it is not so simple in actual devices. The deposition of metal patterns (such as Ti or Au) on the surface depletes the carriers beneath, especially in the case of a low carrier density substrate. The (110) QW in this experiment has a relatively low carrier density, due to difficulties of MBE growth. The area where the metal patterns are deposited was expected to be fully depleted at low temperature, so a positive voltage should be applied to the plunger gate to appropriately tune the QD potential.

Compared to Fig. 3.3.1a, the diagram shown in Fig. 3.3.1b has a structure with a series of almost diagonal lines, but still shows bonding/anti-bonding features, even though the plunger gate applied a positive voltage insufficient to split the confinement region around the center. Ideally, the 2DEG sheet is defined by the electrostatic potential of the designed gate patterns, but the practical potential is modified by impurities and defects in the substrate. As mentioned above, small damage to the electrodes (peeling at the edges or slight floating of the metal patterns) could also occur in QD devices unintentionally. No matter how careful the design is, fine tuning of the gate voltages sample-by-sample is needed. As a result, QDs sometimes cannot be controlled in the expected manner.

Those unexpected potential caused by impurities or defects could generate unintentional quantum dots. The unintentional dots behavior can be seen more clearly in the few-electron regime.

3.3.2 QD Operation in the Few-electron Region

A dot current measurement allows the direct observation of the quantum dot state via the electrons tunneling through those states. The electron current is detected by a current amplifier which has measurement limits. In the standard design of the lateral QDs, the gate electrodes that mainly tune the QD confinement potential also change the tunnel barrier. Therefore, as the number of electrons in the dot decreases, the tunneling rate to the reservoirs is lowered, and the current flowing through the dot also decreases. Therefore, it is difficult to reach the few-electron regime solely by monitoring the QD current. Normally the charge sensor method using a nearby QD is employed to explore few-electron states.

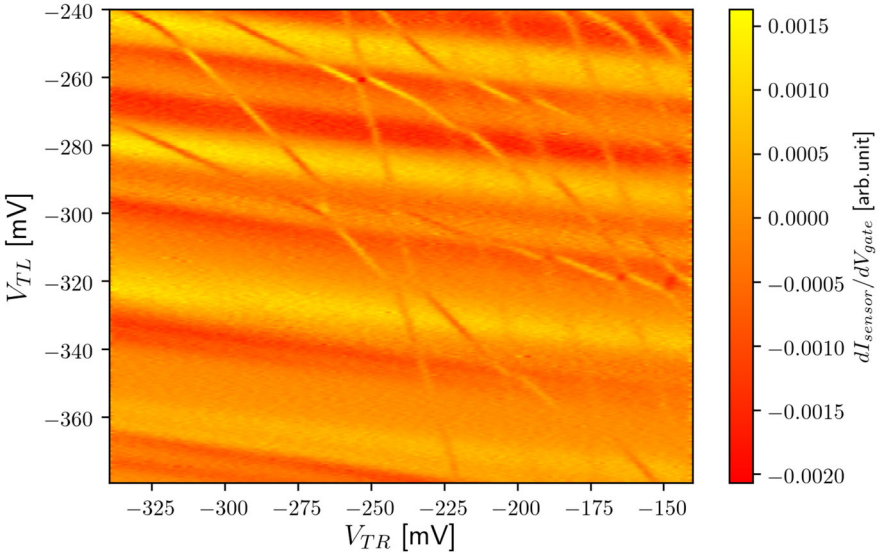

Fig. 3.3.2: Charge stability diagram in few-electron regime.

Figure 3.3.2 is the charge stability diagram in the few-electron regime obtained with the charge sensor method. The charge sensor is the QPC for which the gate voltage was set at just before the pinch off voltage. A small QPC current is so sensitive to the charge environment surrounding the QPC and is affected by charge changes in nearby capacitively coupled QDs. By differentiating the current value of the charge sensor with respect to the gate voltage applied on the target QD, it is possible to detect where the electron number of a QD changes giving rise to the

transition lines in the diagram. A charge sensor plot for an ideal DQDs is shown in Chapter1 Fig. 1.3.4.

Electrons in the confined region are expelled as a more negative voltage is applied. As a more negative voltage is applied, the number of electrons in the dot decreases. Finally, the diagram shows a region where no transition lines appear even when the voltage is made more negative. This region is the zero-electron region for all the dots.

Rise-time dependence of current amplifier and Signal-to-noise Ratio

The "rise time" is a parameter of the current amplifier (DL1211) used in our measurements and sets the integration time on the signal acquisition. Although the "rise time" is an analog parameter of the current amplifier, it governs the time response of the measurement circuit in a certain condition in our measurement setup. Reducing the "rise time" is needed to detect fast phenomena in the measurements. At the same time, a short rise time also increases the noise in the signal, so noise countermeasures should be carefully taken in advance.

Ingenuity in experimental setup such as noise filtering has already been discussed in Section 3.2. Ground loop removal and protection[3] on BNC cables are usually done after starting measurements. After implementing those noise reduction measures, measurement conditions are optimized to improve the signal-to-noise ratio (SNR).

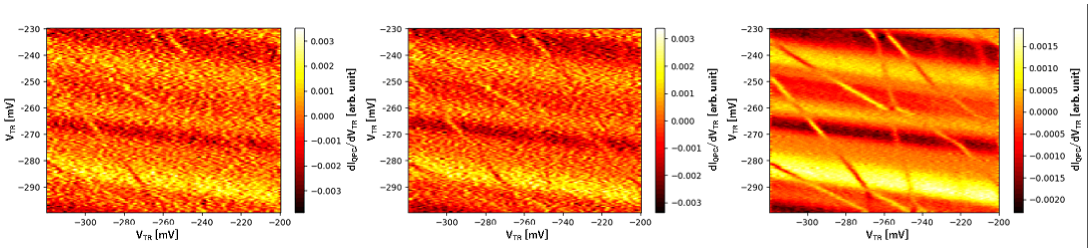

(a) Rise time minimum. (b) Rise time 0.3 msec. (c) Rise time 3 msec.

Fig. 3.3.3: Stability diagrams measured with various rise times.

However, no matter how much the noise is reduced, the shortening of the rise time is limited by other reasons. The factors giving that limit are, 1) processing speed

[3]Enclosing the BNC connectors and cables by Aluminum foil or metal sheet is one of the ways.

of the measurement PC, 2) characteristics of the electric circuit, and 3) detector sensitivity. The former could be improved by using a measurement board integrated with the measurement PC, or FPGA circuit. On the other hand, the latter is mainly determined by stray circuit parameters (capacitance, inductance, etc.). As long as noise filters (RC filters and filters for RF) and long wires are used, the circuit will have an avoidable limitation in the measurement speed.

The "rise time" dependence of the current measurements is shown in Fig. 3.3.3. While even at less than 0.3 msec rise time only a few transition lines can be recognized most of the transition lines are unclear. A "rise time" of 3 msec was used in this experiment in order to have a better SNR which is directory related to the accuracy of dot state detection. Tunneling rates between two dots, (or between dot and reservoir) are tuned much shorter than 3 msec.

Incidental quantum dots

In a stability diagram of a multiple QD, it is possible to identify the dot for which electron number is increasing or decreasing from the slope of the transition line. The slope of the transition lines in the charge stability diagram tells us in which dot[4] the number of electrons has changed. More specifically, by assigning transition lines of a specific slope to a given dot, the absolute number of electrons in the dots under some gate voltage conditions can be known by counting the numbers from the zero-electron region.

More than three slopes can be seen in the diagram of Fig. 3.3.4a unlike a stability diagram expected for a DQD as shown in Fig. 1.3.4, indicating that more than two QDs exist there and response to the gate voltage sweeps. Figure 3.3.4b shows a schematic stability diagram deduced from the measured stability diagram shown in Fig. 3.3.4a. This implies an unintentional triple quantum dot has formed.

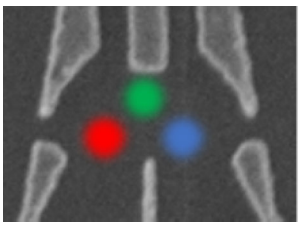

Fig. 3.3.5: Deduced dot configuration.

The electron numbers determined from the schematic diagram (Fig. 3.3.4b), are denoted in parentheses in both figures of Fig. 3.3.4.

[4]Not only series dots but also parallel dots could be generated.

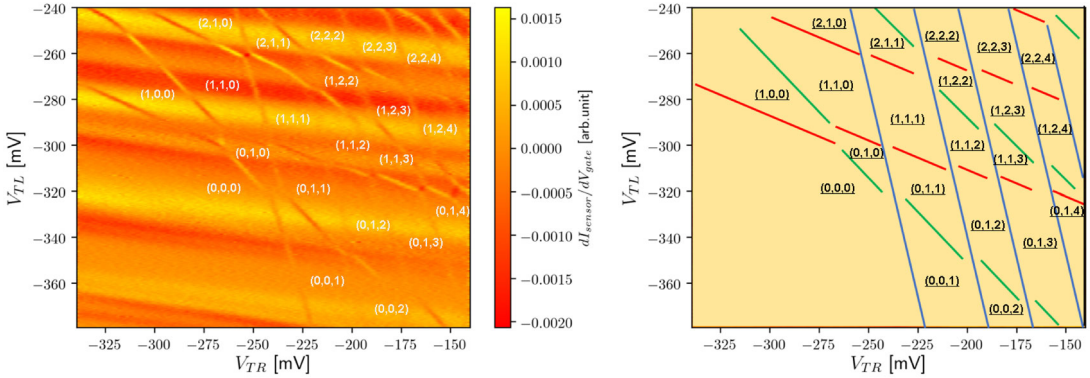

(a) Charge stability diagram with electron numbers.

(b) Schematic illustration of the transition lines and electron numbers.

Fig. 3.3.4: Charge stability diagram in the few-electron regime.

While the gate metal pattern is designed to form a DQD with the center gate separating the left and right QDs that also controls the tunnel coupling between the two dots, a third unintentional QD was formed. This means that the unexpected potential caused by defects or impurities in the substrate traps electrons locally and works as an effective quantum dot. We call such unintentional bound states as 'Incidental Quantum Dots' in this thesis. It is considered that the formation of incidental QDs tends to be suppressed in high mobility 2DEG systems. However, after cooling down the device, the existence of the incidental QDs is taken as an uncontrollable factor. While the design of a DQD shown in Fig. 3.3.5, in which the QD potential is controlled by the laterally spreading electric field, has been used for several preceding works on quantum state conversion from a single photon to a single electron spin, the possibility of the incidental dot formation cannot be excluded.

Transition lines present in Fig. 3.3.4a and illustrated as blue lines in Fig. 3.3.4b become blurry lines as the applied gate voltage V_{TR} becomes more positive. This implies that the incidental dot corresponding to the blue line in Fig. 3.3.4b made impact on the gate voltege V_{TR}. Not only the number of electrons in the dot but also the confinement potential could be distorded by the gate voltage V_{TR}.

3.3.3 "Quasi" DQD operation and Real-Time Measurement

When the DQD design shown in Fig. 3.3.5 is used as a platform for photon-electron spin conversion, the DQD has to be formed at the designed position in a controlled manner. Moreover, tunneling rate tuning, absolute electron number control in each of the dots, and Pauli spin blockade state formation are needed. In the photon-spin quantum state conversion experiments, one of the dots in the DQD works as a photon detector, which traps a single photo-electron generated by an absorbed photon and the other dot detects the excited electron spin state via Pauli spin blockade, which distinguishes spin-up or spin-down of a photo generated electron by monitoring the inter-dot tunneling of the photogenerated electron.

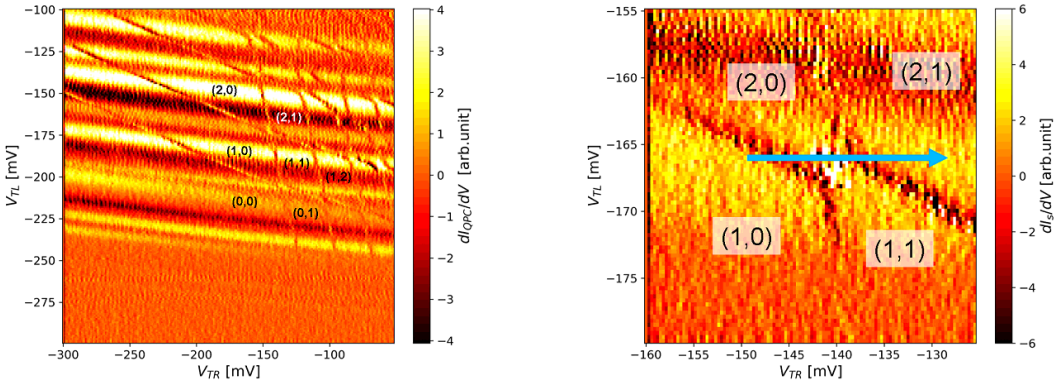

(a) Stability diagram tuned as a DQD by applying asymmetric gate voltages.

(b) Enlarged stability diagram around the (2,0)-(1,1) transition.

Fig. 3.3.6: Stability diagram of DQD formed by tuning the gate voltage.

While suppressing the influence of incidental dots, the voltage of the gate electrodes were adjusted so that only two slopes of the transition lines are visible on the diagram. Since the voltages were applied somewhat asymmetrically to purposely avoid the incidental dot effect, the confinement potential might not be symmetric with respect to the design. However, since the transition lines are invisible in the lower right area, it is presumed that the DQD was formed using an incidental dot rather than a dot formed by the gate-induced potential. Even if the incidental dots was involved, the PSB is expected to be observed in the (2,0)↔(1,0) region because a clear transition line is observed there.

Real-time Charge Sensor Measurements

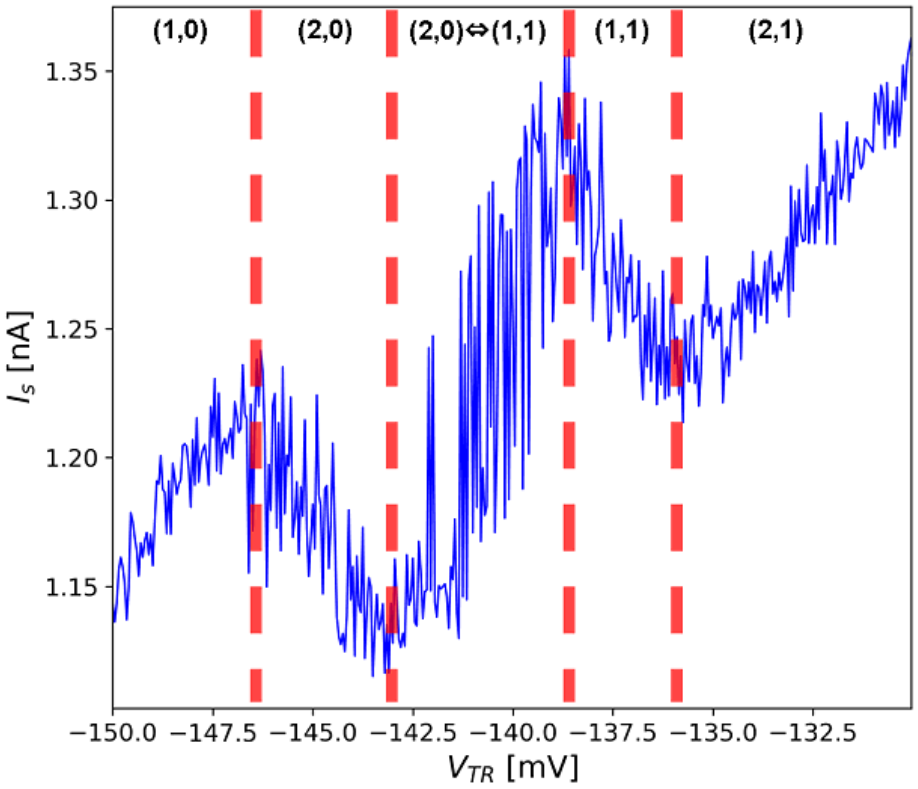

Fig. 3.3.7: Real time charge sensor measurement around the region where PSB is expected. The vertical axis shows the charge sensor current and the horizontal axis is the voltage applied on one of the gate electrodes V_{TR}.

We have also succeeded in detecting the change in the electron numbers in the DQD in the region where electrons tunnel between the two dots. The charge sensor current changes in a binary manner between two levels matching to the (2,0) and (1,1) charge states. A time evolution of the charge sensor current while the gate voltage V_{TR} is -140 mV is shown in Fig. 3.3.8a. This is from a region near the triple point of (2,0)↔(1,0) in the diagram shown in Fig. 3.3.6b. The coupling rate tuned by the gate voltage allows electrons to transit between the two dots probabilistically, which can be seen as a binary distribution of voltage vs time in the

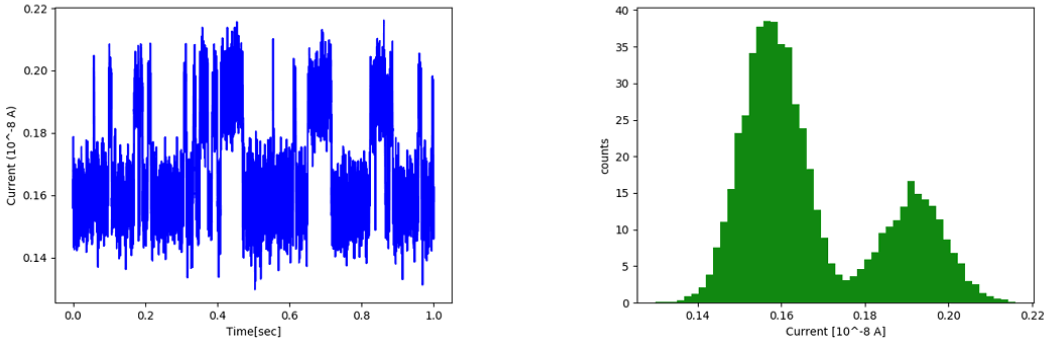

(a) Real time charge sensor measurement. (b) Distribution histogram.

Fig. 3.3.8: (a) Real time charge sensor measurement with the gate voltage V_{TR} fixed at -140 mV where the (2,0)↔(1,0) transition happens. (b) The distribution histogram calculated from the real time measurement. The two peaks clearly show that the charge sensor detects the electron tunneling behavior as binary data.

real time measurements. Figure 3.3.8b is a histogram which shows a distribution of the number of data points obtained from Fig. 3.3.8a. The histogram plot is made by grouping the charge sensor data within a range of current and counting the number of data points in those groups. This binary data demonstrates the real time measurement of dot tunneling behavior. The tunneling rate can be calculated by counting the time distribution on each state of the binary signal. Combination with PSB which induces a tunneling rate difference by electron spin state enables us to detect the real-time spin state.

Chapter 4

Pauli Spin Blockade and g-factor Estimation

In Chapter 3, using the standard micro-fabrication technique, we have fabricated QDs in a (110) QW with a gate electrode design similar to those used in the previous research on the photon-spin quantum state conversion. Then, we have demonstrated QD operation in a few electron regime. While the successful demonstration of QD on a (110) substrate, we are aware of some problems. We could not observe Pauli spin blockade (PSB) effect, which provides a single photoelectron spin detection scheme, in the (110) QD devices. The formation of unintentional dots may disturb the fine tuning of the quantum states to observe PSB. These problems we have may be associated with the difficulties in the high quality 2DEG growth on (110) substrates. In this chapter, to improve the QD operation and observe the PSB effect, the gate pattens are redesigned based on a recent QD patten. In addition, the idea of the device structure to explore spin related phenomena with respect to the crystallographic orientation in (110) plane is explained here.

PSB offers a spin detection method in gate defined lateral DQDs. In the demonstration of the quantum state conversion in a lateral DQD, PSB is used to detect the single photoelectron spin in a DQD in real time. In the DQD with a new design, we observe the PSB both in many electron regime and in a few electron regime by measuring the dot current. Electron g-factor is a fundamental parameter for quantum state conversion [24], electron spin manipulation by EDSR [36, 53], and electron

spin transport [28]. The leakage current in low magnetic fields in the PSB regime provides the magnitude of nuclear spin fluctuation that mixes the two-electron single and triplet states and lifts the PSB at low magnetic field. The values of in-plane g-factor estimated from the PSB leakage current in different electron number regions in a DQD formed in a (110) QW are discussed.

In the conventional photon-to-spin quantum state transfer experiments, a photomask with an aperture has been used to prevent the light illumination in the area other than the QD area. A photon transmits though the aperture fabricated on a target QD. We have established the fabrication of the photomask and the tiny aperture. While the optical fiber scanning experiments will be explained in Chapter 5, the details in the photomask fabrication are discussed together with the fabrication of the redesigned lateral DQD in this chapter.

4.1 New Design of the Electrode Patterns of QD Devices

In the experiment of Chapter 3, we employed the QD design similar to that used in the previous experiments by Morimoto [49], Fujita[20] Kuroyama [41]). The gate design is somewhat old style and needs extending of the electric field laterally to form the confinement potential. Since the QD area in the design is relatively large, the photon absorption area would be wide, preferable for the photon-spin quantum state conversion. However, the spread of the electric field in lateral direction makes it susceptible to local potential disorders due to impurities or defects, resulting in a formation of unintentional dots. Therefore, the narrow pitch between metal electrodes of the QDs should be adapted to suppress the influence of the unintentional dots.

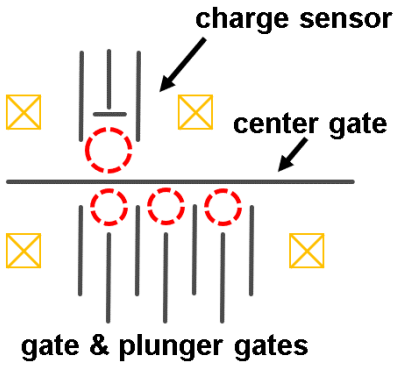

Fig. 4.1.1: Schematic pattern

In recent years, as research on multiple quantum dots more than triple dots has become active for developing quantum computers, simpler QD gate structures with

a smaller area have been reported [57, 19]. Based on these studies, we have come up an improved design of the device in which barrier gates and plunger gates are placed along the center gate as shown in Fig. 4.1.1. Also, QPC or QD for the charge sensor is formed on the opposite side of the multiple QDs across the center gate.

4.1.1 Device Structures for in-plane Anisotropy Studies

As we have discussed in Section 1.2, Dresselhaus spin orbit interaction originated in the bulk-inversion-asymmetry (BIA) depends on the crystallographic orientation. This results in the spin properties depending on the crystallographic orientation. In (110) QWs, specific anisotropic characteristics of spin-orbit interaction [28] and electron g-factor [29, 23] in (110) plane have been reported. Here we will explain the design of (110) QD devices that enables us to study the anisotropic spin related features and their applications to spin manipulation.

In-plane Asymmetry of Electron g-factor

The well-width dependence of the electron g-factor in GaAs (001) QW layers was studied experimentally [14, 65, 24]. J. Hubner *et al.* focused on (110) quantum well and pointed out the specific in-plane anisotropy of the electron g-factor [29]. In the (110) quantum well, the anisotropic feature of the g-factor can be treated as a g tensor which has a diagonal shape for the [110] growth direction [29],

$$g = \begin{pmatrix} g_s & 0 & 0 \\ 0 & g_s + 2g_a & 0 \\ 0 & 0 & g_z \end{pmatrix}, \tag{4.1.1}$$

which implies an in-plane anisotropy of the electron g-factor. This matrix shape was also experimentally obtained and the matrix elements were calculated from the fitted data [23].

Moreover, hole spin g-factor was also investigated and in-plane anisotropy was shown[77, 78, 23]. The values from these studies are summarized in Table 4.1.1 for the well width of 12 nm as same as the (110) substrate used in this thesis. We note that the in-plane g-factor of heavy holes becomes non-zero in (110) QWs due to the subband mixing with light holes.

External field $\vec{B}$ direction	$[00\bar{1}]$	$[\bar{1}10]$
Electron g-factor	-0.21(max)	-0.17(min)
Heavy hole g-factor	larger than $\|0.4\|$	smaller than $\|0.4\|$

Table 4.1.1: g-factor values for in-plane magnetic field with different crystal direction in (110) QW with 12 nm well width.

In-plane g-factor is a significant parameter for quantum state conversion. Also, effective magnetic field from spin-orbit interaction has large asymmetry in (110) QWs. Whichever electron shaking or transport for electric-dipole spin resonance (EDSR), the direction of spin-orbit interaction is important factor. Spin manipulation is an essential technology for spin state tomography. This is why we must construct a device design considering the combination of the substrate crystal orientation, external magnetic field, and direction of series dots.

Gate Design and Photo-mask

As mentioned in Section 4.1, series dot with a simple electrode design is considered as a prerequisite for the new QD devices. To study the effects of the anisotropies of spin-orbit interaction and g-factors on spin relaxation and spin manipulation, two multiple QDs with an identical gate design are placed with their QD array axes orthogonal to each other. Schematic illustrations of the QD configurations are illustrated as shown in Fig. 4.1.2.

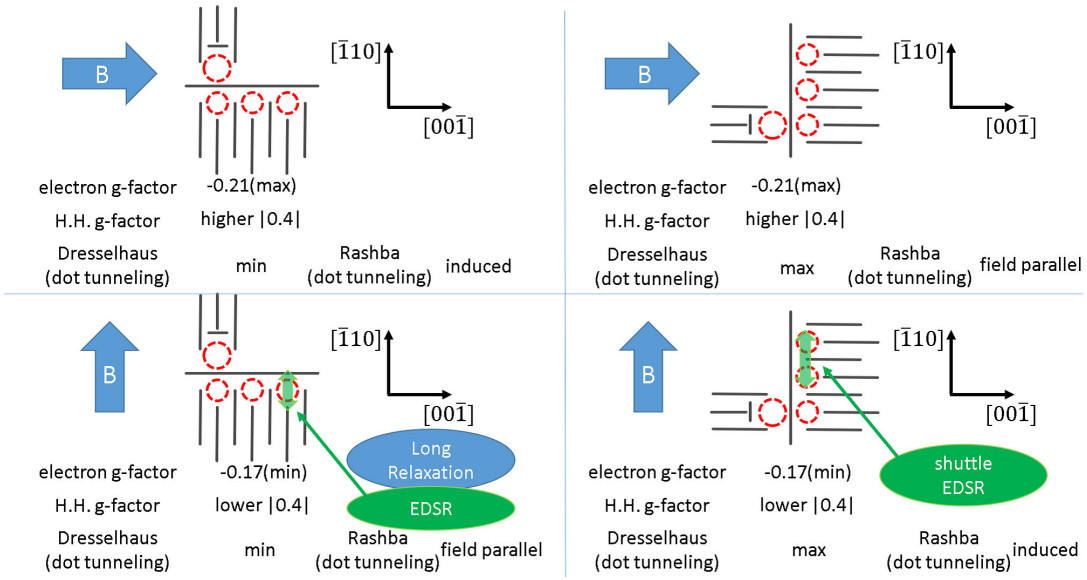

Fig. 4.1.2: Schematic figures of QD electrode designs and QD configurations on a (110) QW

The relations among magnetic field direction, magnitude of spin orbit interaction, and g-factor with respect to the crystal directions are clearly seen in Fig. 4.1.2. The ideal condition of g-factor values for quantum state conversion is the situation with the smallest for electron spins and the largest for hole spins. However, the maximum and minimum directions in the (110) plane are the same for both electron and hole spins.

High fidelity and high speed spin manipulation in GaAs has been demonstrated using a micro-magnet which induces a local magnetic field gradient [67, 57]. However, the design of the micromagnets must satisfy the large magnetic field gradient for fast spin manipulation and large Zeeman field for individual spin controls simultaneously. Robustness against misalignment between the magnets and QDs during the microfabrication processes is required, which may increase the load of device fabrications. On the other hand, spin-orbit interaction induced EDSR could eliminate those issues of the micromagnets, and the magnitude of the dots could be extended[1].

[1]In the case of the micro-magnet, the region of filed gradient is limited for few dots. Independent

In the case of (110) QWs, effective field of the Dresselhaus spin-orbit interaction is induced perpendicular to the substrate. Assuming that the direction of inter-dot tunneling in series dots is determined by the gate pattern design, The spin-orbit induced EDSR could be expected to suppress the spin relaxation mechanism with sustaining the fast spin manipulation capability.

For example, in the case of the lower left panel in Fig. 4.1.2, during dot tunneling, electrons feel an effective magnetic field consisting of a small Dresselhaus field and a Rashba field parallel to the external field. This configuration can minimize a torque on an electron spin disordering the spin phase. Shaking an electron confined in a QD by applying RF electric field, of which frequency matches to the Zeeman splitting energy, on the plunger gate can induce the EDSR with maximizing[2] the spin-orbit field perpendicular to the external field.

On the other hand, in the case of the lower right in Fig. 4.1.2, the total effective field will be maximized during electron tunneling with minimizing the torque on an electron spin, which should be very effective for spin shuttling manipulation [19].

spin manipulation is ensured the difference of Zeeman splitting energy from the stray magnetic field. Then, more strategy is needed to extend the dots structure for spin manipulation in each dots.

[2]Combination of a perpendicular Dresselhaus field and an in-plane Rashba field generates a finite effective field in a direction with a tilted angle from normal to the substrate. This effective field direction is perpendicular to external magnetic field.

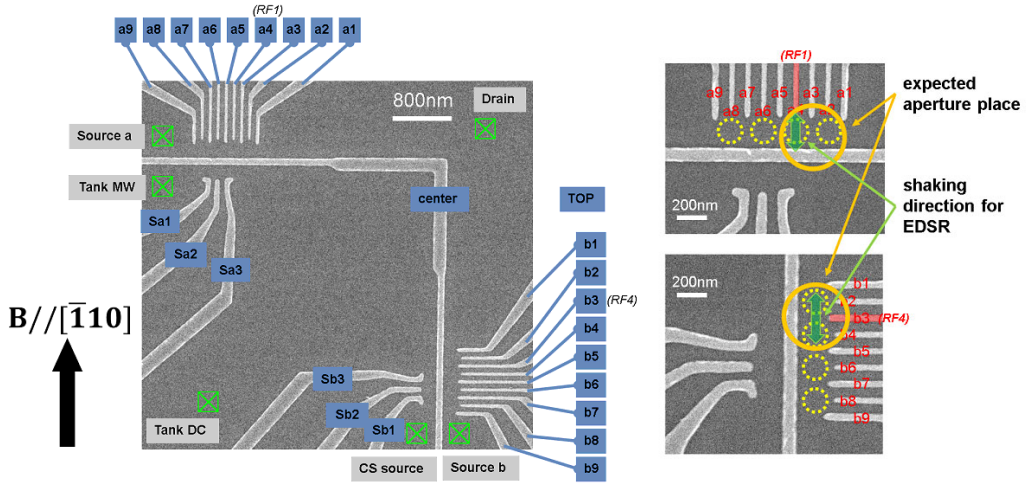

(a) (b)

Fig. 4.1.3: SEM images of quantum dots. (a) Image of a whole device containing two sets of series quantum dots sharing a drain contact. (b) Enlarged image of each series dot. The expected positions of QDs by yellow dotted circles and an aperture in the photomask by orange solid circles. The plunger gate, which is indicated by red color, is connected to an RF source at room temperature via a bias-T.

In order to observe or compare both configurations shown in the lower two figures in Fig. 4.1.2, we installed a center gate with a right angle and set the series dots along the center gate.

For the optical experiments, a photo-mask is fabricated on the dot gate patterns with inserting a "Calixarene" insulating film beneath the photo-mask. Since the thickness of the Au/Ti photo-mask is 200 nm, the incident light passes only through two apertures fabricated on the photo-mask. This allows us to irradiate photons selectively to the confinement area of the quantum dots. However, there is a finite possibility that photons are illuminated on the other region of the dots. These photons may excite the unintentional carriers or may ionize impurities, which disturbs the stable operation of the charge sensor and the dots.

4.2 Measurement Setup

We designed and fabricated the quantum dot devices at SANKEN in Osaka University. The measurements discussed in this and the next chapter were done at National Research Council Canada (NRC) in collaboration with G. Austing, L. Gaudreau, and A. Sachrajda.

4.2.1 Dilution Refrigerator Setup

The dilution refrigerator (Bluefors, BF-LD250) was used for the measurements. The base temperature of the fridge was less than 10 mK at the mixing chamber. Images of the fridge are shown in Fig. 4.2.1. Figure 4.2.1 a) shows the whole fridge after installing the outer covers. Figure 4.2.1 b) shows the inside of the fridge without outer covers. Temperatures denoted in the notes indicate the temperature at each

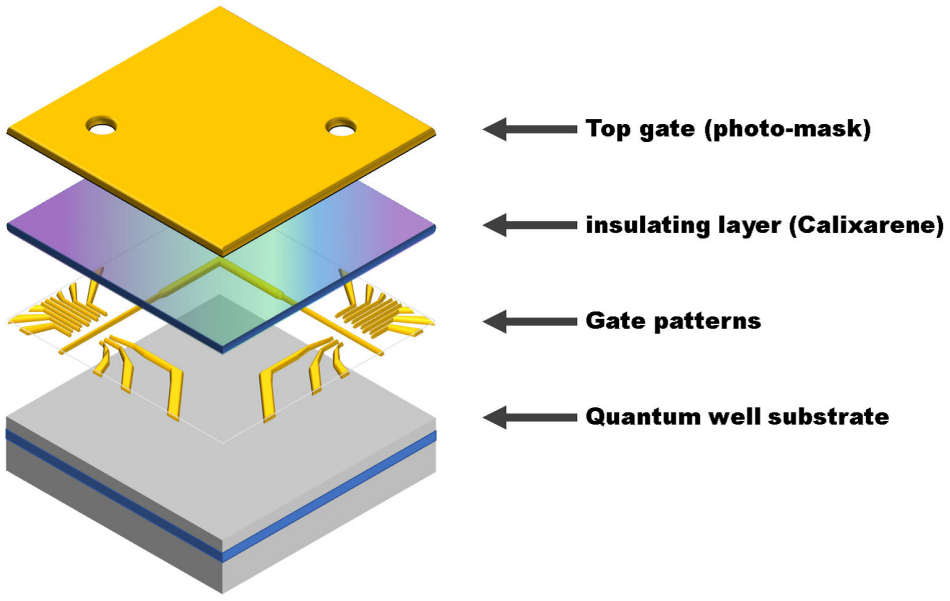

Fig. 4.1.4: Schematic figure of the device structure. On the (110) substrate, fine gate pattern with Ti and Au is deposited, and a *Calixarene* inlulator is formed by electron-beam lithography. Photo-mask with holes working as top gate is finally deposited.

stage during the operation. At the bottom of the fridge, a home-made cold-finger, Cryogenic SPIN Setup, is attached to the mixing chamber plate. The sample on the cold-finger is positioned at the center of an 8T solenoid superconducting magnet. RF and DC lines for electrical controls of the QDs and optical fibers for delivery of light to the sample are installed from the top of the fridge at room temperature to the cold finger at low temperature.

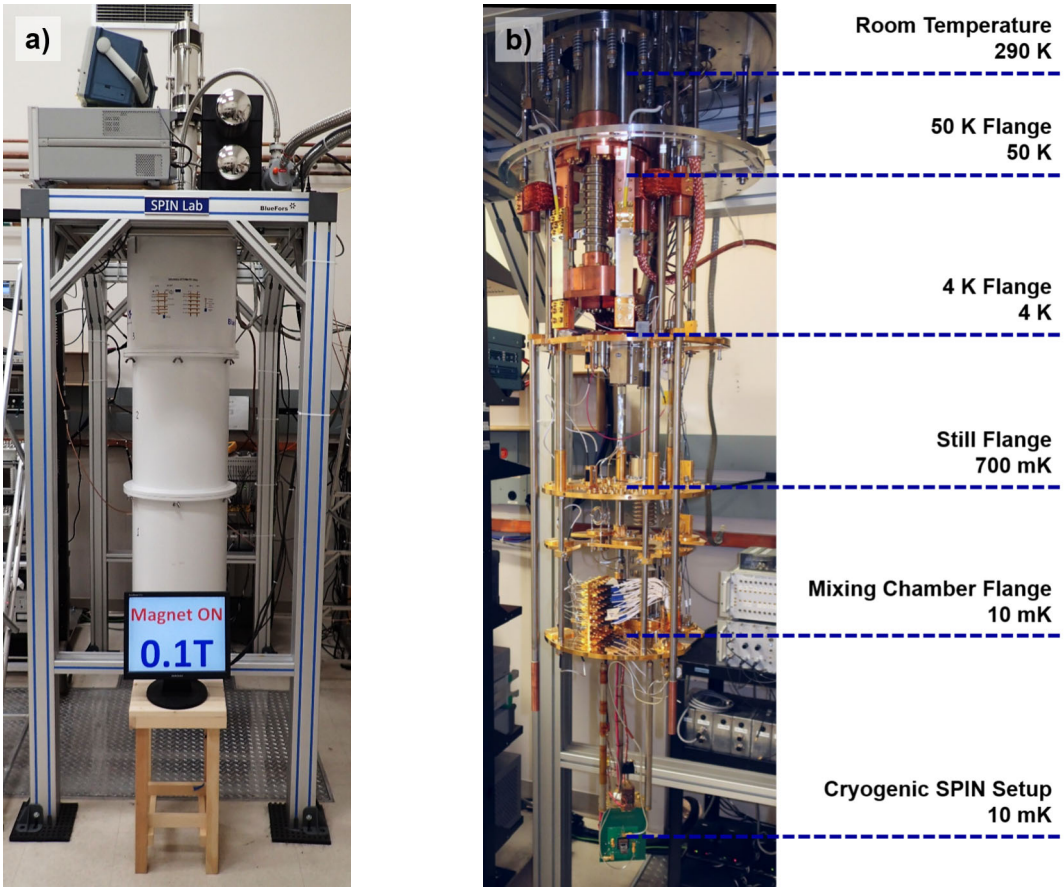

Fig. 4.2.1: Pictures of the dilution refrigerator at NRC(Spin Lab.). a) Whole picture with outer covers. b) Inside of the dilution refrigerator.

4.2.2 Sample Stage Setup

The images of the sample stage are shown at Fig. 4.2.2. The sample for measurement is mounted on the sample holder with a special glue, and Au wires are bonded

between pads on the sample and connectors on the holder. The bonding pads on the sample are fabricated at the same time as the ohmic contacts by AuGe/Ni alloy metals deposition followed by annealing under forming gas ambient. The metal diffusion into the semiconductors induced by the annealing process enhances the adhesion of the bonding pads. However, it is more difficult to bond Au wire on the surface of the annealed AuGe/Ni alloy electrodes due to low adhesion during the wire attachment, compared to usual semiconductor devices. We suspect that the wire bonding without a peeling off the metal pad on the (110) surface is more difficult than conventional (001) surface. After the sample is attached on the sample holder, all the pins of the sample holder are grounded with a conductive sponge until installing on the sample stage. When the holder is installed on the stage, a special stopper is used to carefully insert the holder into the socket to ensure the electrical connection (Fig. 4.2.2 b)). The sample stage has a printed circuit board (PCB) for DC and RF circuits, including filters and bias-Ts that realize the electrical connections between high frequency signal and DC voltage on the same lines.

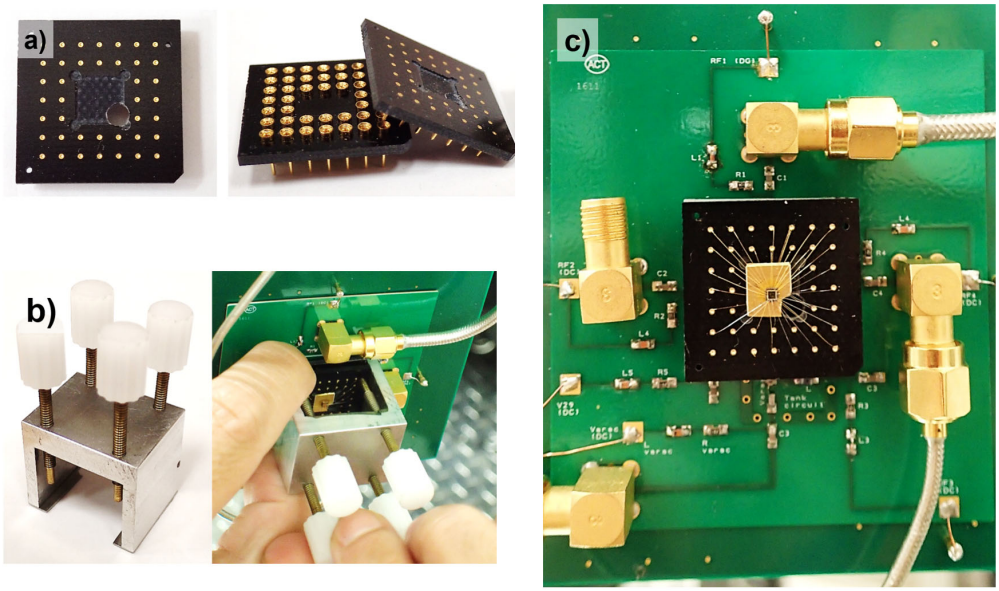

Fig. 4.2.2: a) Sample holder b) Holder stopper c) Wired sample installed with the stage. These pictures are referred from Master thesis of Jason Phoenix (University of Waterloo, 2019)

4.3 Pauli Spin Blockade in Many-electron Region

Here, we study the transport under a finite bias through the DQD in a multi electron regime. Figure 4.3.1 (a) shows the stability diagram where we performed the following bias triangle measurements. While the exact electron numbers in the DQD are not identified, as denoted by (N,M), relatively weak coupled DQD is inferred from the shape of the anti-crossing feature.

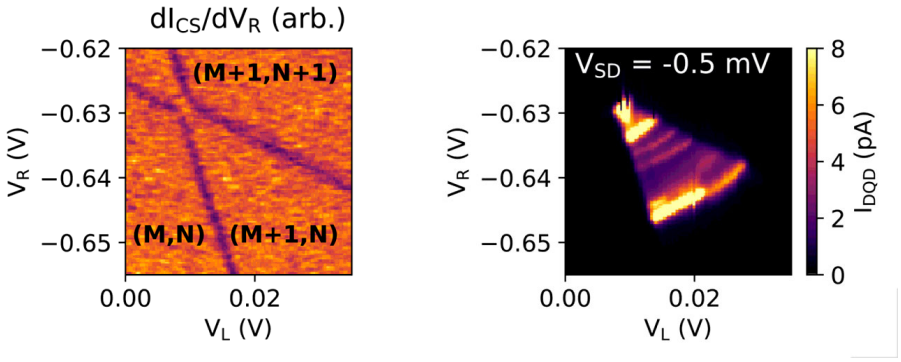

Fig. 4.3.1: (a) Charge stability diagram measured by the charge sensor in a many electron regime. (b) Bias triangle measured by dot current[51].

Transport though the DQD under a finite bias appears as bias triangles (4.3.1 (b)) as shown in Section1.4. The occurrence of Pauli spin blockade (PSB) can by identified by measuring the baseline behavior of the bias triangles at various magnetic fields[37]. Figures 4.3.2 (a), (b), and (c) show the bias triangles for forward bias of V_{SD} = +0.5 mV. As marked by the red asterisk in Fig. 4.3.2 (a), the finite conductance observed in the vicinity of the base line in the triangle at 0 T is a leakage current. With increasing magnetic field, the conductance disappears. On the other hand, when the revere bias of V_{SD} = -0.5 mV is applied, the conductance is almost unchanged with changing magnetic field up to 4 T. This asymmetric feature (rectification) on the applied bias can be attributed to the PSB. Hence, we successfully demonstrated the PSB in a GaAs DQD formed in a (110) QW, which is one of the crucial achievements for the investigation of efficient photon-spin quantum state conversion. The suppression of the conductance in the vicinity of zero magnetic field, indicating the lifting of PSB near zero magnetic field, can be explained

in terms of the mixing of single and triplet states by the statistical fluctuation of unpolarized nuclear spins of Ga and As atoms [27, 37, 32]. Electrons in QDs couple to nuclear spins of the constituent atoms of the host semiconductor materials via the hyperfine interaction. The inhomogeneous magnetic field due to the fluctuating magnetic field by nuclear spins causes evolutions of three (1,1) triplet states into (1,1) singlet state. When Zeeman splitting energy between the singlet state and the triplet states exceeds the energy of the fluctuation of unpolarized nuclear spins, the PSB is restored at finite magnetic fields.

Though GaAs is known as a material with a weak spin-orbit interaction, the influence of the spin-orbit interaction on the inter-dot tunneling, which has been reported in GaAs[47, 21], is suppressed in our device configuration. Since the DQD measured is aligned along the $[00\bar{1}]$ direction and the magnetic field is applied along the $[\bar{1}10]$ direction perpendicular to $[00\bar{1}]$ direction, the Dresselhaus spin-orbit effective field is zero and the Rashba field is parallel to the magnetic field. In this configuration, the spin flip process induced during the inter-dot tunneling becomes ineffective.

The magnetic field dependence of the leakage current can provide the magnitude of nuclear spin fluctuation. Figure 4.3.3 (a) shows the detuning dependence of I_{DQD} along a section through the bias triangles as a function of a magnetic field at $V_{SD} = +0.5$ mV. The bottom of this figure is closer to the resonance transport on the base line of the bias triangles where the states in each dot are aligned energetically (zero detuning). Despite no significant broadening of the leakage current peak observed at zero detuning, the peak of the leakage current at zero detuning may contain a contribution of the spin-flip co-tunneling process, which has been discussed at zero detuning point in silicon DQD containing less nuclear spins [44]. Note that the co-tunneling process was not considered in the previous work on GaAs DQDs [37]. Therefore, in the following discussion for the evaluation of nuclear spin fluctuation, we focus on the inelastic transport regime at finite detuning.

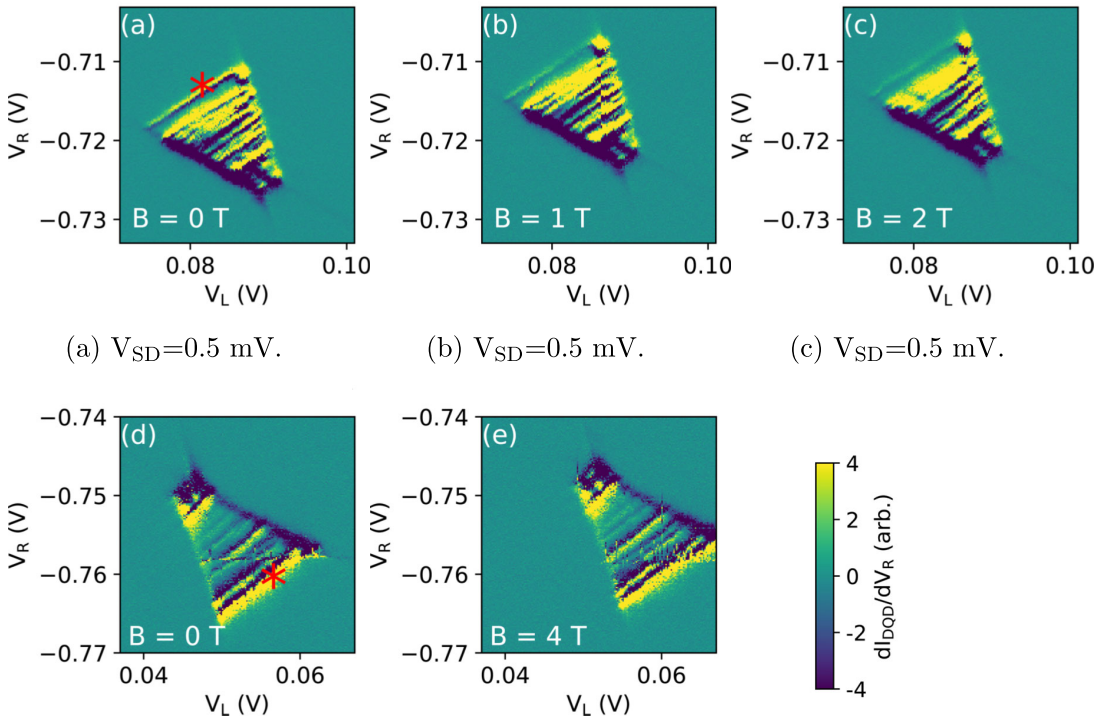

(a) V_{SD}=0.5 mV. (b) V_{SD}=0.5 mV. (c) V_{SD}=0.5 mV.

(d) V_{SD}=-0.5 mV. (e) V_{SD}=-0.5 mV.

Fig. 4.3.2: (a)-(c) Transport triangles plotted as dI_{QPC}/dV_{a6}, in arbitrary units, in forward bias (V_{SD} = +0.5 mV) showing a clear current feature along the base (indicated by an asterisk) at 0 T (spin blockade is lifted due to mixing with nuclear spin), and a suppressed current feature due to spin blockade along the base at 1 and 2 T. (d) and (e) Corresponding transport triangles in reverse bias (V_{SD} = -0.5 mV) showing clear current feature along base at 0 and 4 T (spin blockade is absent). The transport triangles in some of the panels are impacted by telegraph noise and jump in the charge stability diagram due to random charge trapping events in the material[51].

g-factor estimation from leakage current

The statistically fluctuating magnetic field caused by an ensemble of unpolarized nuclear spins is subject to an electron spin in a QD via the hyperfine interaction. The magnitude of this fluctuating magnetic field is described as $\sim A/\sqrt{N}g^*\mu_B$. A is the hyperfine constant ($\sim$130 μeV for GaAs [70, 10]). N is the number of nuclei that are coupled to an electron spin in the QD. g^* and μ_B are the effective electron g-factor and the Bohr magneton, respectively. By fitting a simple Gaussian curve to the leakage current peak, we obtain the standard dispersion σ, instead of using the functions in Ref. [10]. While a flat-top of the peak shape is expected in Ref [10], we could not resolve the feature.

From the fit to the data shown in Fig. 4.3.3 (b), we obtained $\sigma = 19 \pm 1$ mT. As shown in Fig. 4.3.3 (c), σ changes within 20 % in the measured detuning range, inferring that σ is almost independent of the detuning and determined not by inter-dot tunnel coupling [10] but by the nuclear spin fluctuation. Koppens *et al.* reported $\sigma \sim$ 5 mT in a DQD formed in a GaAs/AlGaAs heterostructure on a standard (001) GaAs substrate, which is four times smaller than that obtained in our measurements, suggesting a reduced effective g-factor in the DQD fabricated in the (110) QW compared to those obtained in DQDs on (001) substrate. Assuming that the typical number of nuclei within the extension of the electron wavefunction in the QD is $N \sim 10^6$ and the full polarization of nuclear spins in GaAs is 5 T and effective electron g-factor of GaAs is $\sim$0.4, the corresponding effective electron g-factor to the σ value obtained in this measurement can be determined as $g^* \sim 0.1$ in a GaAs/AlGaAs QW on a (110) substrate. As discussed in Section 4.1.1, this value reasonably agrees with the value of 0.16 measured by photoluminescence in a 12-nm (110) GaAs QW [29].

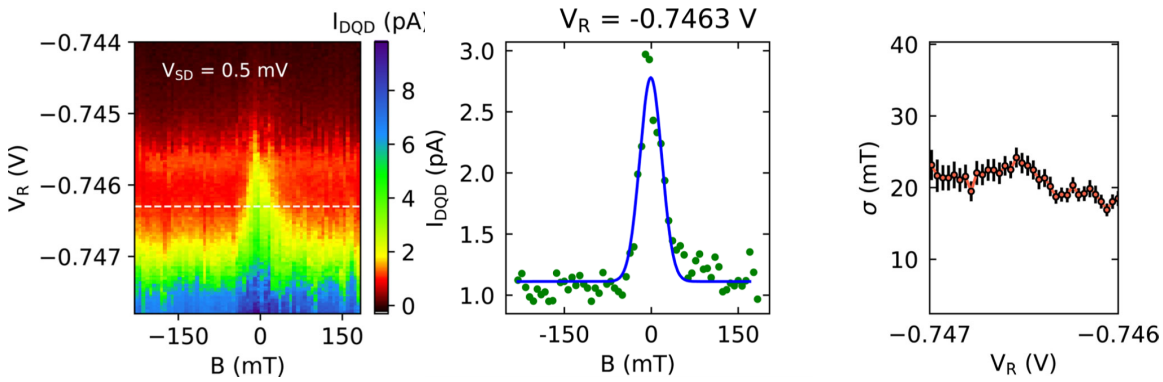

(a) (b) (c)

Fig. 4.3.3: (a) Detuning dependence of I_{DQD} along a section through the transport triangles (at the center of, and perpendicular to, the base of the triangles) in forward bias ($V_{SD} = +0.5$ mV) for a B-field stepped in small increments through zero fields. (b) Typical I_{DQD} vs B cross section, indicated by a dashed line in (a). (c) σ vs detuning throughout the inelastic tunneling regime [51].

4.4 Pauli Spin Blockade in a Few Electron Region

In the end of the previous section, we investigated the QD transport in a many electron region even though we were able to reach the few electron regime and count absolute value of electrons in the DQD, because we were worried about impact by potential fluctuations leading to the formation of incidental QDs that couple to the DQD of interest. However, demonstration of quantum state conversion from single photons to single electron spins requires control of a small number of electrons in QDs. We explored transport and Pauli spin blockade in the case of few electron regime.

Figure 4.4.1 shows the stability diagram around a few electron regime. Figure 4.4.1 (a) and (b), respectively, are obtained by charge sensor and dot current. It can be seen clearly that the zero electron region has been reached in Fig. 4.4.1 (a).

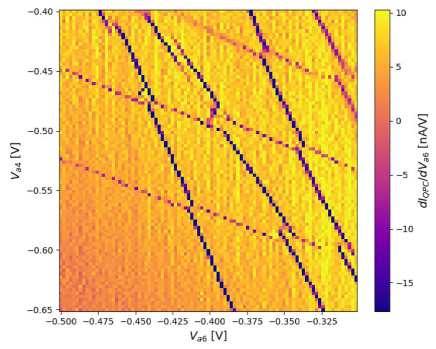

(a) Charge sensor, (V_{SD}=0.5mV)

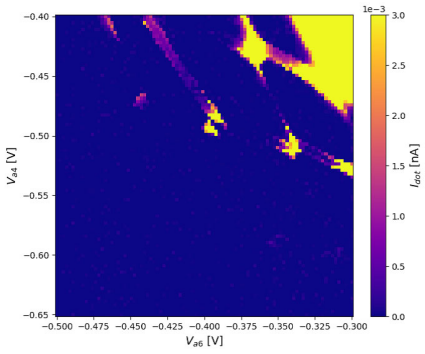

(b) Dot current, (V_{SD}=0.5mV)

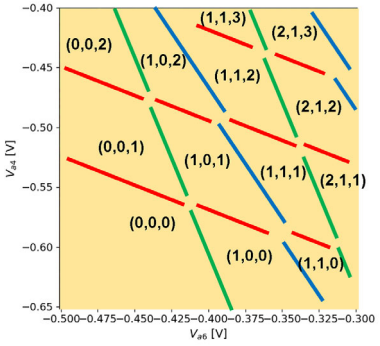

(c) Schematic as TQD

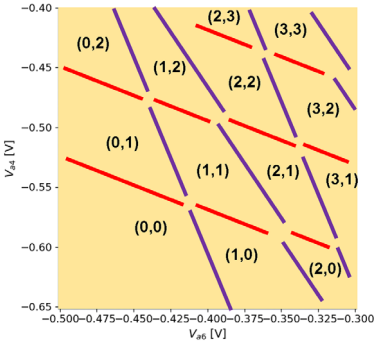

(d) Schematic as DQD

Fig. 4.4.1: (a) Stability diagram by differentiation of the charge sensor current dI_{QPC}/dV_{a6} with bias $V_{SD} = 0.5$ mV. (b) Stability diagram by dot current I_{dot} with bias $V_{SD} = 0.5$ mV obtained at the same time when the charge sensor detection for (a). (c)-(d) Schematic emphasizing the transition lines assuming triple quantum dot (TQD) or DQD formation. Since the vertical lines shown by green lines and blue lines have slightly different slopes, which imply the separated dot formation, it could be regarded as formation of TQD including dot implied by red lines. Electron numbers counted from zero-electron regime is shown in the diagram too. On the other hand, the difference in the slopes is not very large between green lines and blue lines, thus, it could also be considered that green and blue lines indicate a single dot formation. The schematic diagram assuming a DQD is shown in (d) combining the green and blue lines into purple lines from (c).

Asymmetric current of the bias triangle by PSB

To make the interpretation simpler, we assume a DQD formation here at first. Since we are able to count the absolute number of electrons in each region, we can easily verify the triple points where the PSB occurs. Figure 4.4.2 shows the diagram which tells us the correspondence of electron number region and the blockade direction by PSB. Because of the assumption of DQD formation as Fig. 4.4.1 (d), PSB behavior is expected at the triple points of (0,2) $\leftrightarrow$ (1,1) and (1,1) $\leftrightarrow$ (2,0).

Figure 4.4.3 shows the clear transport triangles obtained by enlarging the conduction point of (1,1) $\leftrightarrow$ (2,0) from Fig. 4.4.1. Comparison of 4.4.1 (d) and 4.4.1 (e) shows the different size of transport triangle, which is clarified by the white-dotted triangles. Transport blockade under magnetic field can be seen only in the direction corresponding to (1,1) $\leftrightarrow$ (2,0) at the bottom of the transport triangles.

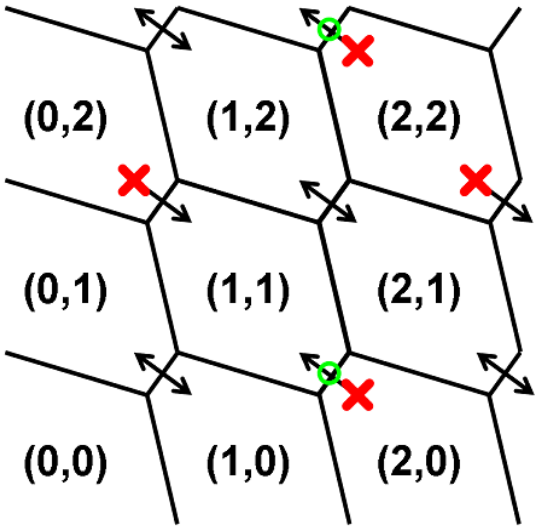

Fig. 4.4.2: Schematic of PSB directions in a few electron region

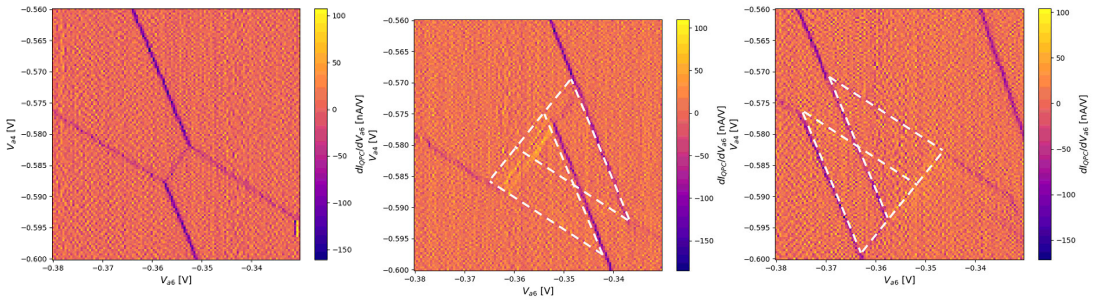

(a) dI_{QPC}/dV_{a6}, V_{SD}=0mV (b) dI_{QPC}/dV_{a6},V_{SD}=1mV (c) dI_{QPC}/dV_{a6},V_{SD}=-1mV

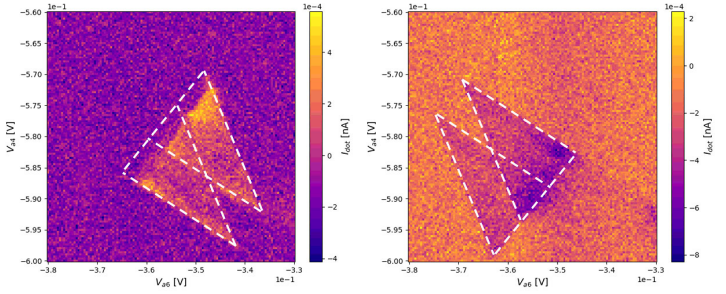

(d) I_{dot},V_{SD}=1mV (e) I_{dot},V_{SD}=-1mV

Fig. 4.4.3: (a)-(c) Transport triangles plotted as dI_{QPC}/dV_{a6}. (d), (e) Transport triangles plotted as dot current I_{dot}. External magnetic field is B = 0.1 T. 1 mV bias is applied in (b) and (d), and an opposite -1 mV is applied in (c) and (e). Triangles denoted by white-dotted lines in (b)-(e) are the same size.

It can be confirmed that the size of the bias triangle is reduced in the charge sensor in Fig. 4.4.3 (d) as well as in the case of the dot current, and the transport to one side is suppressed. The base shift of the triangles shows singlet-triplet splitting as discussed in Ref.[52].

4.4.1 g-factor Evaluation in a Few Electron Regime

Triple Dot Behavior

At the (1,1) ↔ (0,2) point, transport of DQD was confirmed by PSB from the singlet-triplet splitting behavior as Fig. 4.4.3. However, larger bias as V_{SD}=3mV

induces the triple dot transport, which may be caused by the incidental potential. Figure 4.4.4 shows the bias triangle plotted as dot current with V_{SD}=3 mV bias.

g-factor estimation by PSB leakage current

At the (1,1) $\leftrightarrow$ (0,2) point with V_{SD} = 3 mV bias, we investigate the detuning behavior for sweeping the gate voltage of V_{a4} vs magnetic field at 6 points.

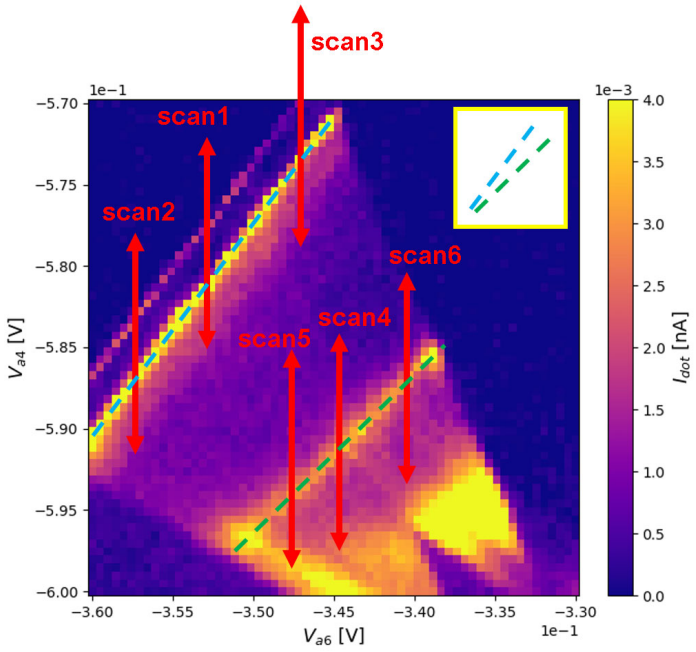

Fig. 4.4.4: Bias triangle plotted by dot current at (1,1) $\leftrightarrow$ (0,2). Bias is applied of V_{SD} = 3 mV under no external magnetic field. At the base of the triangle, singlet-triplet splitting area and current as the narrow lines along the base can be seen. This leakage current under zero magnetic filed is induced by the electron spin flipping contacting to nuclear spins even though the base of triangle is in a PSB region. Moreover, thicker resonance lines are observed around the center of the triangle. Such lines could be generated when an excited level appears as an electron transport path if the slope of this line is the same as the base of the triangle. The green dashed line along the center and the blue dashed line along the base are drawn for eye-guide. The parallel displaced lines are shown in the upper right inset to identify the difference of the slopes, which implies the triple dot formation. External magnetic field decreases the conductivity lines both at the base of triangle and at the center due to PSB.

During the B-filed sweep, the mapping of the diagram sometimes slides as a telegraphic jump occurs during the gate voltage steps, which is considered to be caused by the unintentional and unstable trap potential near the dot or the charge sensor QPC. By moving part of the diagram parallel along the misaligned borders to match the resonance peak, we were able to infer the original dot current behavior with suppressing the telegraphic jump effects. In addition, Figure 4.4.5 shows the vicinity of the area where the dot current is plotted against the magnetic field sweep. Leakage current caused by the lifting of PSB can be fit by a Gaussian function, which can be seen around zero B-filed and near the gate voltage of the resonance peaks.

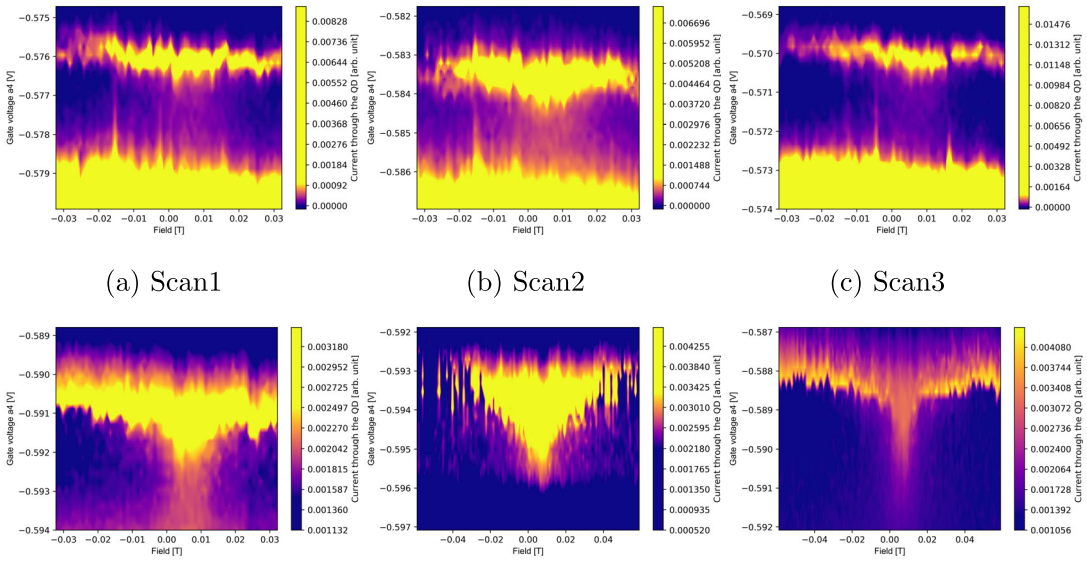

(a) Scan1 (b) Scan2 (c) Scan3

(d) Scan4 (e) Scan5 (f) Scan6

Fig. 4.4.5: The detuning vs B-filed around the region where Gaussian fitting is applied(contrast is adjusted). The captions of each label as Scan 1 to 6 are corresponding to the label in Fig. 4.4.4. The images of Scan 1, 2, 6 are modified by the parallel shift, and the images of Scan 5, 4 are re-plotted by the removal of partial noise jumps.

g-factor plot on each scan

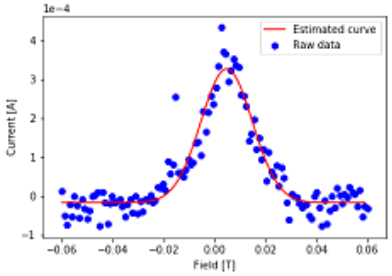

Fig. 4.4.6: Typical I_{DQD} vs B near the resonance lines as blue dots, and Gaussian fitting curve plotted by a solid red curve. Gaussian fitting is calculated by Python analysis using the Scipy package.

Figure 4.4.7 shows the result of g-factor estimation. The g-factor estimation method is discussed in Section 4.3. It can be seen that the g-factor values estimated in each scan point change very sensitively to the detuning gate voltage compared with the values estimated in the multi-electron region. Moreover, the value around 0.2 is higher than the value of 0.1 in the case of many electron region in Section 4.3. The strength of confinement with the gate voltage is different due to the different electron number regions under investigation. In the multi-electron regime, the conduction associated with PSB is induced through high-energy excited states. On the other hand, in a few electron region, we see the conduction through the ground state energy level. This result is reasonable from the fact that the values of electron g-factor have dependence on the energy level occupying the state. However, further analysis is needed to explain this difference from a quantitative point of view. Additionally, the bias triangle corresponding to this analysis indicates the triple quantum dot conduction caused by the unintentional potential. The existence of unintentional third dot could imply not only simple increase of the number of dots, but formation of very localized confinement or strong tunnel coupling that cannot be normally produced by the electric field from the gate voltage. We can consider the possibility of that such a local potential strongly distorts the spread of electron wavefunction and induces large fluctuations or the bigger absolute values compared to the result in the case of the many electron regime.

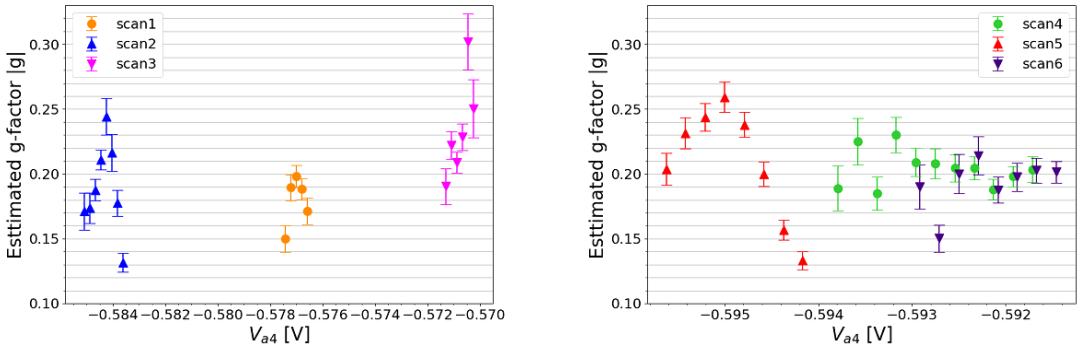

Fig. 4.4.7: Estimated g-factor in the few electron regime. The numbers of Scan 1 to 6 corresponds to Fig. 4.4.4 and Fig. 4.4.5. Horizontal axis is the detuning gate voltage of V_{a4}.

g-factor for quantum state conversion

It was suggested that the g-factor value of electrons in dots may vary depending on the number of electrons and confinement conditions. However, most of the values were smaller than 0.25 or less. In order to realize quantum state conversion, it is necessary to design the g-factor so that the Zeeman splitting energy of the electron spin is sufficiently smaller than the Zeeman splitting energy of the hole state to be excited, and these must be smaller than the energy spectrum width of excitation laser. It is necessary to actually evaluate the behavior in the dots, but in the (110) QW, which has the same well width with the substrate used in this experiment, the g-factor of heavy holes is reported as around 0.4 [22, 23]. This heavy hole value as around 0.4 is bigger than the electron g-factor estimated here, so we consider that the results in this work show that the (110) substrate used in this study is suitable as a platform for realizing quantum state conversion between single-photon and single-electron spin by exciting a heavy hole state.

Chapter 5

Optical Fiber Scanning Over the Device in Dilution Refrigerator

In this chapter, we discuss efficient and precise photon irradiation methods for quantum dots, which are essential for experiments on photon-spin quantum state conversion and future quantum repeaters. In the previous studies, line-of-sight optical delivery systems have been developed, in which a laser beam is controlled at room temperature and introduced into a dilution refrigerator through a window at room temperature on the dilution refrigerator and directed to the quantum dots at low temperature. However, because the positions of the objective lens and quantum dots fixed at low temperature cannot be controlled at low temperatures, the optical alignment cannot be precisely adjusted only by controlling the laser beam at room temperature, leading to reduced efficiency and deviation from ideal light irradiation.

In contrast, NRC in Canada is constructing a system that enables precise position control by introducing an optical fiber into a dilution refrigerator and driving the tip of the fiber mounted on piezo stages at low temperature. However, precise alignment and light irradiation on quantum dots for photon-spin quantum interface has not yet been realized.

Establishing precise positioning and photon irradiation at low temperature will be a major breakthrough as a fundamental technology for the development of quantum repeaters based on photon-spin quantum state conversion.
I stayed at the NRC for three months and tried to realize precise positioning and

control of light irradiation of quantum dots using the optical fiber delivery system at NRC.

5.1 Setup

5.1.1 Sample Holder

Figure 5.1.1 shows the setup on the cold finger with the sample holder and the piezo stage with an optical fiber. As shown in Fig. 5.1.1 a), samples are mounted on a specially-designed printed circuit board (PCB). On the PCB, there are DC channels for electrical control of the QDs and an RF reflectometry circuit used for fast charge detection of QDs.

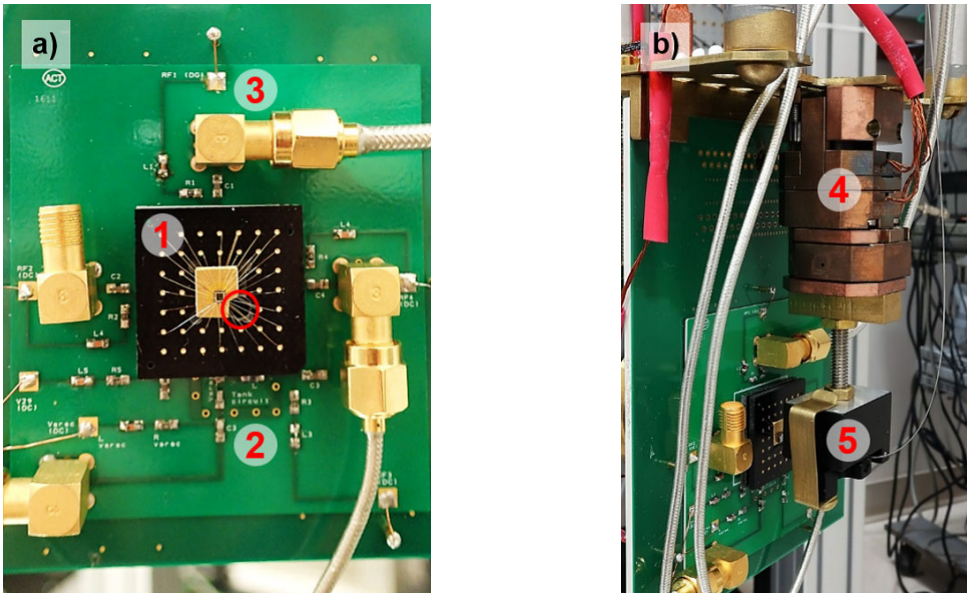

Fig. 5.1.1: The cryogenic setup has several components to allow many different types samples to be tested. a) Sample mounted on circuit board: 1. mounted sample on wire-bonded chip carrier, 2. RF reflectometry circuit, 3. one of the RF lines. b) Fiber positioning system: 4. piezoelectric XYZ nano-positioners, 5. fiber clamp and lensed fiber. These pictures are from the Master's thesis of Jason Phoenix (Waterloo, 2019).

5.1.2 Optical Setup

The light delivery system into the dilution refrigerator consisting of an optical fiber and piezoelectric stages has been developed by Jason Phoenix from the University of Waterloo and his colleague at NRC.

Figure 5.1.1 b) shows the fiber positioning system. Nano-positioning stages for XYZ axes consisting of an Attocube system (two ANPx101/RES, and an ANPz101/RES) are mounted on the cold finger as shown in Fig. 5.1.1 b) labeled by ④. Moving along the X and Z axes gives 2D scanned images, and tuning the Y axis corresponds to adjusting the light focus. The jig clamping the lensed fiber, labeled by ⑤ in Fig. 5.1.1 b), is fixed to the piezo-stage and so moves with the stage. This mechanism enables high definition scanning of the sample at low temperature in the fridge.

Light is guided from the top of the refrigerator at room temperature to the mixing chamber (MC) plate through a single mode 750 nm fiber. A lensed fiber delivers the light from the MC plate to the sample mounted on the PCB. The total length of the fridge fibers is $\sim$ 2.5 m. The expected focal length and a calculated spot size for the lensed fiber from previous experiments are about 8 μm and about 0.75 μm in diameter, respectively.

The light source is located at room temperature in the nearby NRC optics lab. The optical setup at room temperature is shown schematically in Fig. 5.1.2. The light sources used in our experiments are laser diodes of wavelength at 985 nm or 635 nm.

A directional fiber coupler and power meter are used to monitor the intensity of the light entering the fiber connected to the dilution refrigerator. The light is then transmitted from the NRC optics lab to the refrigerator in the NRC cryogenics lab through a 30-m-long, 780HP, single mode fiber.

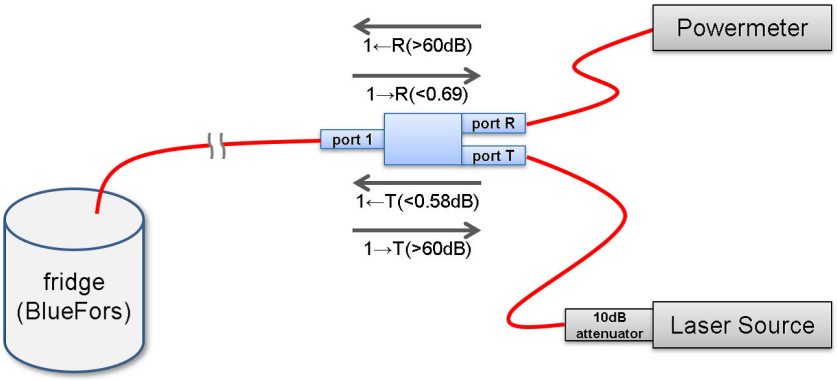

Fig. 5.1.2: Schematic of the optical path from the laser source to the fridge, and to a powermeter. Laser sources can be exchanged dependent on the desired wavelength.

5.1.3 Photo-mask and Aperture

We fabricated a metal mask over the gate pattern with an insulating layer between the two to prevent undesired photon illumination in the area except at the dot confinement area for photon detection. The charge sensor constructed with a QPC is very sensitive to charge around it. During the detection of the photo-excited electron spin state, undesired carriers generated by photon illumination around the QD would disturb the accuracy of the measurements.

Figure 5.1.3 shows optical microscope images with low magnification (left) and high magnification (right). The square pattern is the photo-mask. The faint narrow metal patterns spreading radially outwards are the gate electrodes connected to the QD gate electrodes beneath the photo-mask. The right picture shows the photo-mask with area of $\sim$ 30 μm^2. Since the photo-mask covers the two DQDs shown in Fig. 4.1.3, each aperture is placed above one of two QDs in each of the DQD devices. Figure 5.1.4b shows SEM images of the aperture. The diameter of the aperture is about 500 nm. The aperture is fabricated by a standard lift-off process following various design ideas[1].

[1]explained in the text of Fig. 5.1.4.

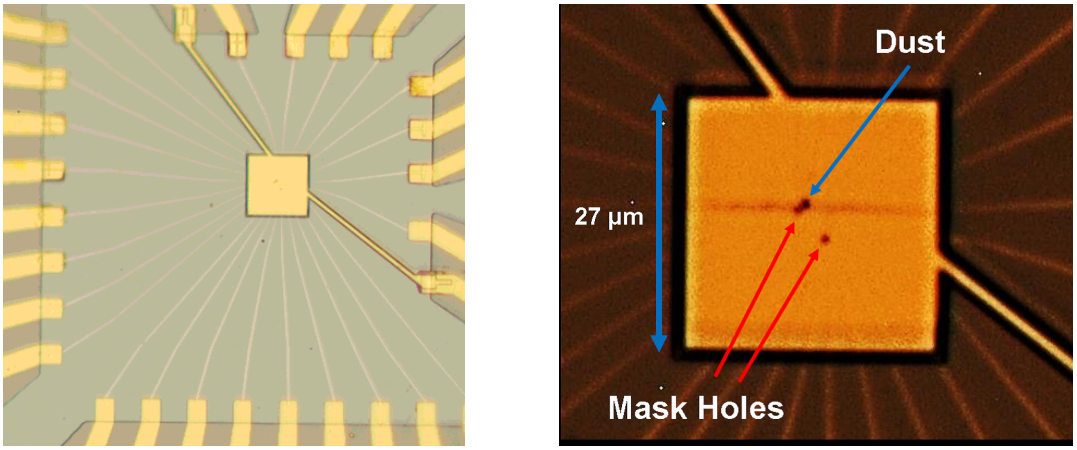

Fig. 5.1.3: Images of the sample taken by an optical microscope. The left image shows the mesa region including the wiring pattern and photo-mask. The right image shows the enlarged photo-mask. This sample is measured at low temperature, and a speck of dust next to one of the apertures can be observed.

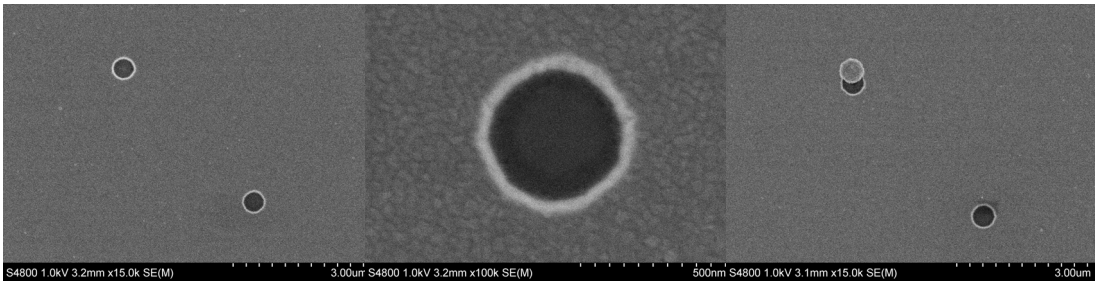

(a) Both apertures. (b) Enlarged aperture. (c) Process failed.

Fig. 5.1.4: SEM image of apertures in a photo-mask. These pictures are taken from a dummy sample when optimizing the fabrication recipe. During photo-mask fabrication it is necessary to leave a small disc-shaped region of resist in place just before metal deposition in order to make the aperture through the metal film of thickness about 200 nm. Considering the proximity effect, sophisticated CAD design of the photo-mask pattern and the condition of optimized e-beam dose time in EB lithography are necessary to obtain the desired aperture. Furthermore, during lift-off of the resist and metal residue, extreme caution is required so that the disc-shaped metal from the aperture region does not block the aperture. The substrate is flipped over and shaken in an organic solvent during lift-off to avoid this issue. Without this simple procedure the disk-shaped metal frequently blocks the aperture as shown in (c).

5.1.4 Measurement Procedure

Here we describe the procedure for fiber scanning. Attocube piezo nano-positioning stages operate on the "slip-stick" principle. A sawtooth waveform voltages is applied to the piezostack. During the initial voltage ramping stage, the piezostack expands and the stage moves due to friction between them. Then, the voltage suddenly drops to zero, and the piezostack quickly shrinks, pulling the piezostack from under the stage. While scanning the lensed fiber, photocurrent and reflectance are measured simultaneously with a current amplifier and powermeter in the optical setup at room temperature, respectively. Focusing of the lensed fiber is performed by monitoring the change in the reflectance at the focal point by changing the piezo positioner along the direction perpendicular to the sample plane.

5.2 Scanning at Room Temperature

After cooling down, it is troublesome to exchange samples to determine reasons why the scanning system may fail. Therefore, we tested first the light delivery system with the sample set at room temperature in the sample holder and without the fridge outer cans in place.

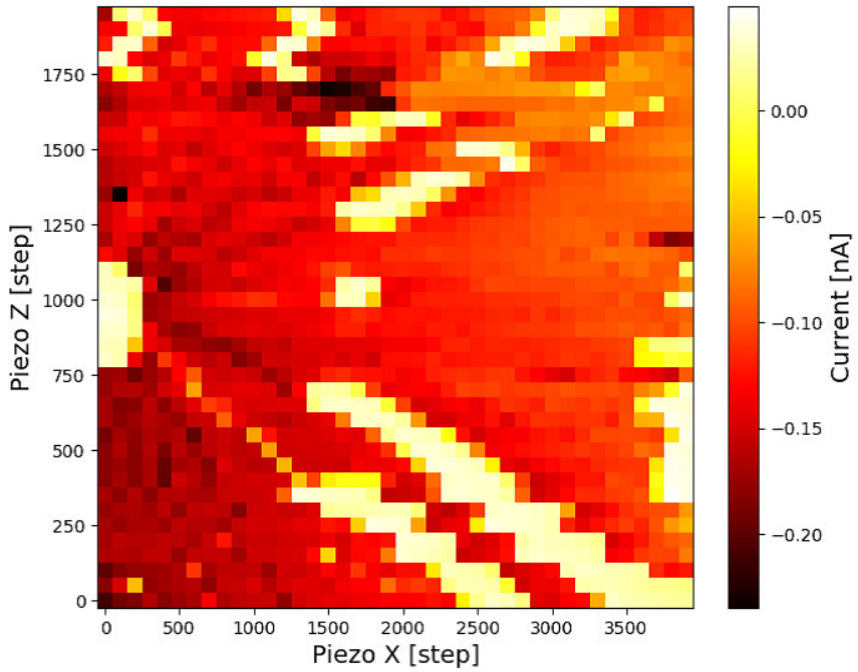

Fig. 5.2.1: Scanned image of the device pattern at room temperature. The initial fiber position is set manually at the jig by hand so that the tip is near the sample. After rough focus adjustment using the reflection signal intensity, coarse scanning is tried to find the location of the photo-mask.

5.2.1 Imaging by Different Wavelength

By exchanging the laser light source connected to the fiber, it is possible to measure or scan the sample at different wavelengths. Figure 5.2.2 shows the result of mapping the photo-mask region at different wavelengths. The relationship between laser

wavelength and energy translates to 1.95 eV at 635 nm and 1.26 eV at 985 nm, respectively. Also, at room temperature, the energy gap is 1.42 eV (870 nm) for GaAs and 1.57 eV (790 nm) for 12 nm well width QW. Focusing on this energy relationship, a long wavelength 985 nm laser should not excite GaAs and the QW layer.

Figure 5.2.2 (a) shows mapping by photo-current with the 985 nm laser. The wiring surrounding the mesa area patterned by optical lithography, and photo-mask covering the QD gate patterns are made of 200nm thick gold, and appear as white regions in the images. According to the reflectance spectrum of gold, which is used for the electrodes and photo-mask, it is known that at longer wavelength, the reflectance is higher. The white regions indicate that there is no transmission of 985 nm light through the thick metal layer and no carriers are excited beneath the metal pattern.

In other regions, the excitation of electrons by thermal energy is possible. It is considered that the 985 nm light in the infrared region is absorbed by the substrate as thermal energy at the spot position, causing instantaneous electron excitation. Around the fine gate pattern area, it is thought that the 985 nm laser light is still partially transmitted through the fine gate electrodes, which are of thickness 10 nm or less, and reaches the substrate. Doped substrates with a low carrier density can be depleted simply by evaporating metal on the surface. During scanning, the transmitted 985 nm laser light induces carriers beneath the fine gate pattern, which causes a relatively large change in the photo-current, resulting in the gate pattern appearing as dark lines in the image.

On the other hand, a very different mapping image can be seen in Fig. 5.2.2 (d), which is obtained with the 635 nm laser. The energy of 635 nm laser is larger than the energy gap of bulk GaAs and GaAs QW structure with 12 nm width. Therefore, it is considered that carrier electrons are generated by absorption of the laser light over the entire substrate including the underlying layer as well as the QW layer in the mesa pattern, and the photo-current is detected all over the sample.

The narrow black lines spreading radially on the mesa pattern, corresponding to the wiring of fine gate patterns, show the same phenomena as discussed above,

where stimulated photo-current are seen in the depletion area. Local photo-current is induced appearing as a black boundary along the mesa pattern and is especially dark on the left side of the image. Since the scan goes from left to right, it is thought that the larger current fluctuations are induced mainly at the moment when the laser spot climbs onto the mesa structure incorporating the QW layer. The reason why more photo-current is seen in the upper right of the mesa is that the detecting pad (ohmic contact) may catch more current through the 2DEG layer of the conduction path.

The most important point here is that laser light with wavelength from 635 nm to 938 nm, which is needed for photo-excited electrons in a GaAs QW, can be transmitted sufficiently well through the fiber system. After setting the sample one can finely tune the wavelength of a Ti:sapphire laser in order to excite the hole state selectively to realize the quantum state conversion without re-establishing the optical setup.

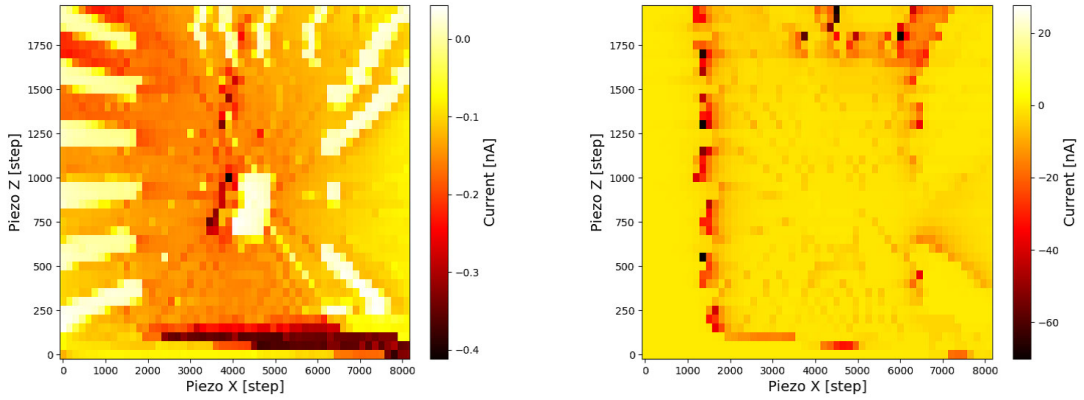

(a) Imaging by 985nm laser light.

(b) Imaging by 635nm laser light.

Fig. 5.2.2: Device pattern imaging with different wavelengths at room temperature.

5.2.2 Imaging by Reflection and Photo-induced Current

A comparison of images taken one after the other under the same conditions with photo-current and reflected light is shown in Fig. 5.2.3. Very similar images are seen from the two consecutive scans, which means that the piezo-stage motion in a narrow

region in a short period of time gives reasonably good reproducibility. When a high-resolution scan is performed at room temperature, the phenomenon of blurry lines in the image due to noise derived from the piezoelectric stage driving is observed. The difference of noise can be seen by comparing the two images. Moreover other noise can be caused from the ambient environment because the outer fridge cans are not in place.

Comparison between images can provide more important information in the low temperature scans discussed below.

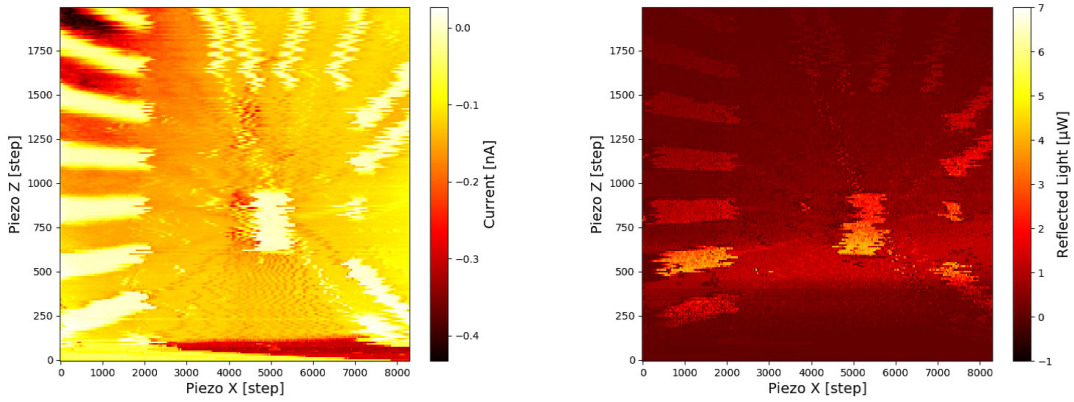

(a) Imaging by photo-current at room temperature.

(b) Imaging by reflection at room temperature.

Fig. 5.2.3: Images of photo-current in (a) and reflection in (b) obtained with 985 nm laser. The step size to image the same region is smaller than in the case of Fig. 5.2.2 (a) so the resolution is higher. The fine gates appearing as black lines are more clear but noise or unintentional jumps still happen.

Figure 5.2.4 shows a high resolution image with optimized conditions at room temperature. If one looks closely at the image, the two apertures in the mask are just visible[2]. It took over 3 hours to take this high-resolution image. During the imaging the focused laser light was continuously irradiated on the sample in the very narrow region around the photo-mask, and on the left side of the photo-mask, damage to the substrate surface and the photo-mask is clear.

[2]Around the center of the photo-mask, two yellowish dots can be seen in the white mask area.

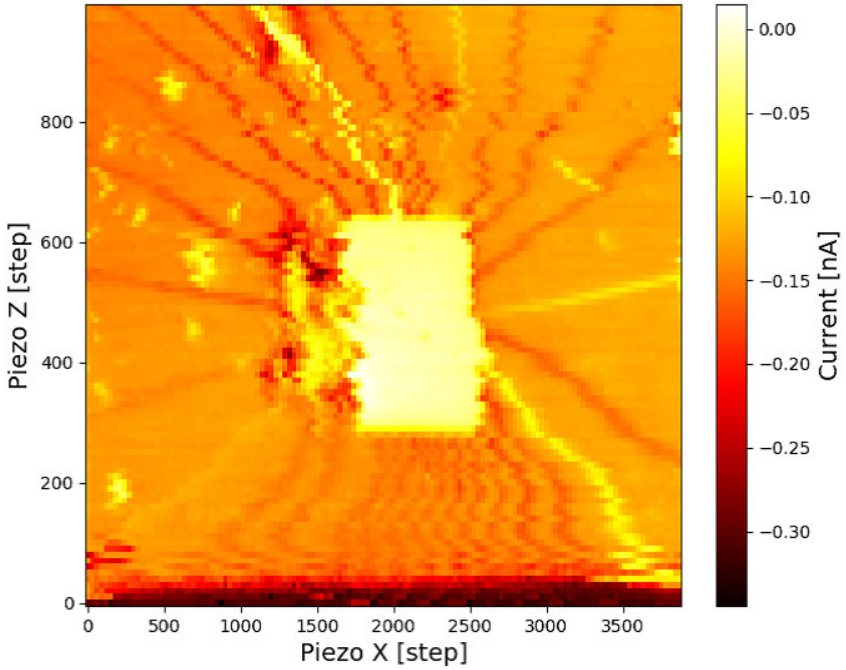

Fig. 5.2.4: High resolution imaging at room temperature with 985 nm laser light. Part of the photo-mask on the left side is damaged likely due to impact from the tip of the fiber.

Damage to the device

We continued the scanning measurements after obtained the image in Fig. 5.2.4. We could not see the clear image with an accurate aspect ratio. Figure 5.2.3 shows the best clear images where we can still see the wiring structure and photo-mask after the image in Fig. 5.2.4 was taken despite the distorted aspect ratio and damage to the surface. The image in Fig. 5.2.3 shows particularly well the damage to the device that occurred during room temperature scanning. It is conceivable that thermal energy damage or localized laser ablation may have occurred as a result of increasing the power of the laser to increase the signal-to-noise ratio. Additionally, the tip of fiber could have touched the surface of substrate physically.

A scanning test at room temperature provides useful informative about the sample status and the optical setup, but we found that focused laser light irradiation by

lensed fiber at room temperature may also damage the device structure. Through room temperature scanning, we confirmed that the software and detectors work. For the next scanning experiment, we irradiated the sample after cooling down the sample to milli-kelvin temperature.

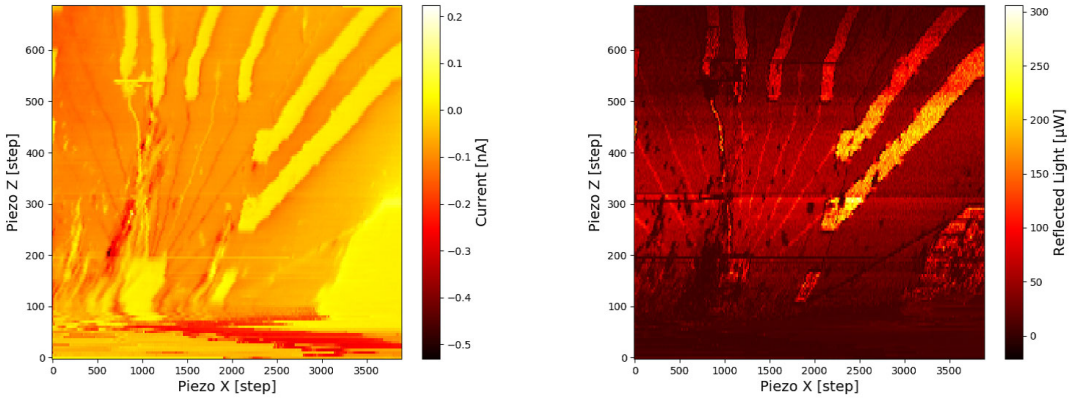

(a) Photo-current image.

(b) Reflection image.

Fig. 5.2.5: Images of damaged device obtained during the scanning experiments at room temperature with 985 nm laser light.

5.3 Scanning at Low Temperature

Given our experience of sample damage during room temperature scanning, we did not irradiate laser on the device before cooling down[3]. When fixing the fiber at room temperature to the jig after setting the sample on the stage, we made sure that there was sufficient distance between the fiber tip and the substrate so that the tip would not touch the surface of the substrate while attaching the outer cans to the fridge and cooling the system down.

[3]Quantum dot formation and PSB observation and so on.

5.3.1 Finding the Target Area on the Sample

Photo-current is very sensitive to the laser light at low temperature. A steep rise in the signal was confirmed just by turning on the power of the laser source and putting it in the standby state. It is considered that a small amount of leaked light reached the sample and induced carriers[4].

Therefore, the focus of the lensed fiber was adjusted by checking the reflected light signal. First, we moved the y-axis direction of the piezo-stage to better focus by changing the distance between the tip of the fiber and the sample based on the reflection peak intensity detected by the powermeter. If the tip of fiber is brought too close to the substrate during this adjustment, it leads to physical damage of the sample, and we have to stop the rise of reflection signal on the way. When we saw some increase or decrease in the reflected signal, we tried to scan the pattern.

The reflection image allows us to identify the scanning region even if the lensed fiber is still out of focus. Figure 5.3.1 (a) shows the coarse image of reflection. Using the wider parts of the wiring in the image as a guide, we can guess the location of the fiber, and set the piezo-stage position of the tip of the fiber near the photo-mask. In the initial scan near the photo-mask, the reflection image was clear, but the photo-current image measured at the same time showed no pattern at all. It is thought that the photo-current could not capture the pattern because the scattered light excited carriers in a wide range until the laser light is focused.

[4]Persistent photo carries should be induced by exciting DX center.

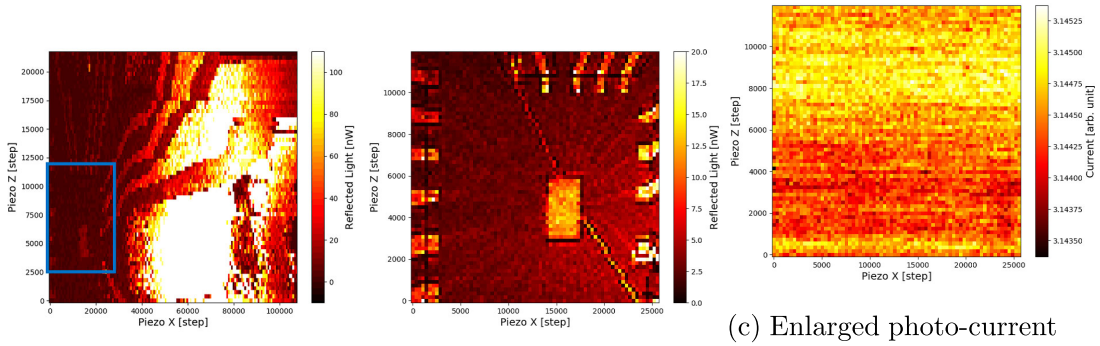

(a) Reflection image at low temperature.

(b) Enlarged reflection image near the photo-mask.

(c) Enlarged photo-current image near the photo-mask.

Fig. 5.3.1: (a) Coarse reflection image of the electrode pattern obtained using the 985 nm semiconductor laser. (b), (c) Images examine the area enclosed by the blue solid line rectangle in (a) which are plotted by reflection signal and photo-current respectively. Only in the case of reflection, clear photo-mask mapping is obtained.

5.3.2 Device Pattern Focusing

Figure 5.3.2 shows the process of narrowing the scanning range to the periphery of the photo-mask and adjusting the focus. As seen in the optical microscope images (Fig. 5.1.3), the sample has two apertures (with a diameter of about 500 nm) on the photo-mask, but dust adheres to one of them. Observing the reflection image in Fig. 5.3.2 (b), one can quickly identify the presence of dust on the photo-mask before improving the focus. After adjusting the focus, it can be seen that the blurred photo-current image has become very clear. It can be seen that there is a difference in appearance of the fine gate wiring- most appearing as black lines and some as yellow lines. It can be considered that the difference caused from the ratio of transmission and reflection light against the wiring patterns.

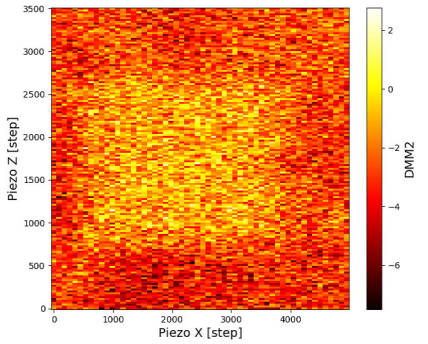

(a) Photo-current before focusing.

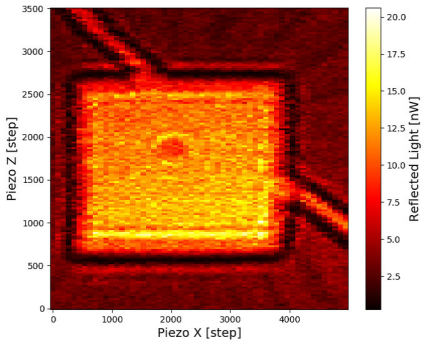

(b) Reflection before focusing.

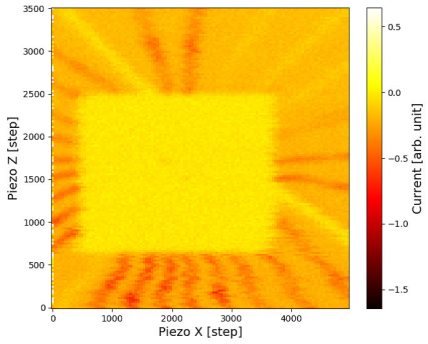

(c) Photo-current after focusing.

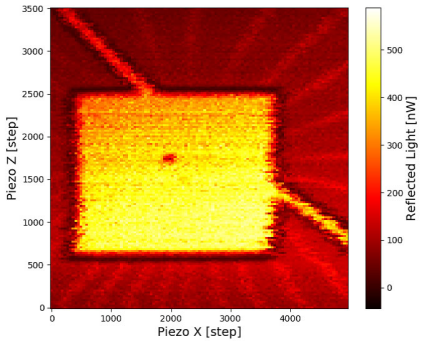

(d) Reflection after focusing.

Fig. 5.3.2: Photo-mask images at low temperature before and after focusing the photo-mask. The photo-current image of (a) became the particularly clear image as (b) by adjusting the focus.

Figure 5.3.3 shows images with further focus and contrast adjustment. In the photo-current image, black dots where the apertures are located are now clearly visible near the center of the photo-mask, and it is confirmed that even laser light of 985 nm can pass through 500 nm diameter apertures and excites carriers.

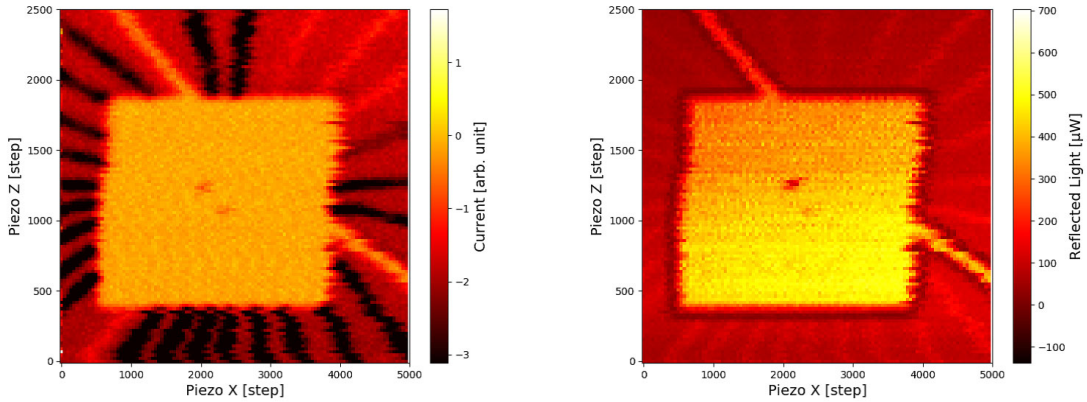

(a) Photo-current image.

(b) Reflection image.

Fig. 5.3.3: High resolution images by photo-current and reflection with optimized focus. Two apertures can be clearly seen in both of the images. The current change at the aperture places in the photo-current image is expected to show that the light transmitted through the apertures and reached on the 2DEG layer.

5.3.3 High Resolution Scan of the Aperture

One of the difficulties in scanning with the piezo-stages is placing the laser spot at specific coordinates. When scanning a certain range with the same resolution, if we can find the conditions for stabilizing the stage, we can obtain very high-definition images like the images shown so far. However, it is not easy to stop the stage while scanning with the stepping mode so that the laser spot is a specific location on the sample, for example, the small apertures on the photo-mask. The number of steps taken by the piezo-stage plotted on the horizontal and vertical axes of the images is not absolute position. Also there is variation in the step distance. Over a limited distance (0.5 microns at low temperature), the stage position can be finely adjusted with voltages (DC voltage mode) applied to the piezo-stage. In a wider scanning range, the actual scan rate or absolute position may vary depending on the stepping resolution (stepping mode) or sweeping distance. This makes it difficult to fix a target location on the sample to take images over a wider range. The simplest method is to reduce the scanning speed and stop after scanning to a predetermined

position. We are then able to scan the aperture with high resolution and estimate the approximate aperture diameter.

In eventual measurements for quantum state conversion, the most important thing about the optical set up is that it can deliver a small laser light spot to the QD region below an aperture. Scanning the sample is required to find the target position to illuminate the sample and then focus to reduce the spot size for high efficiency. The piezo-stage can move with stepping mode to scan a wide range, or DC voltage mode for high-resolution scan over a small area. Scanning over the same area, sweeping the same distance repeatedly, can give good reproducibility only when a good scanning condition is found. On the other hand, it is not easy to place the fiber spot at the target position with an accuracy of 100 nm or less.

Focusing on the dust-free aperture on the lower-right part of the photo-mask, we were able to position the laser spot almost on top of the aperture. After scanning near the aperture, we could constructed a "composite-image" in Fig. 5.3.4 of the small aperture.

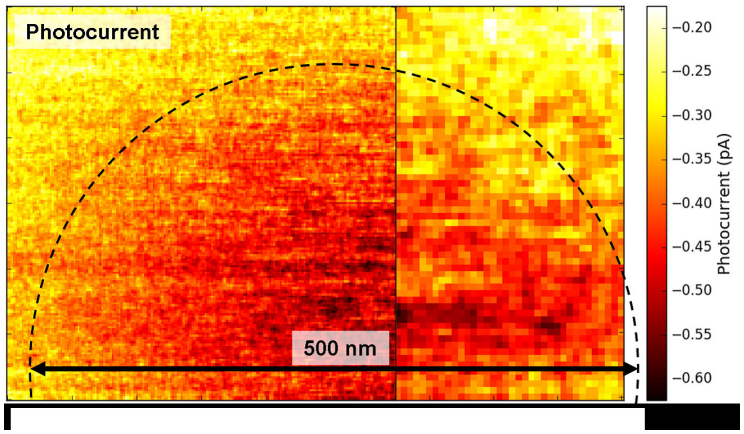

Fig. 5.3.4: Composite image of photo-mask aperture using DC voltage mode for the piezo- stage. The image is obtained by photo-current measurement with 985 nm laser. It is difficult to identify and set the laser spot position by scanning over a very narrow region less than 1 μm because no landmark can be seen during the scan. Hence two different images are combined in order to cover part of the aperture.

Chapter 6

Summary

The development of the fundamental technology for quantum state conversion between single photons and single electron spins in (110) QD devices

This thesis describes the results of the experiments we have consistently performed using (110) QW substrates, aiming to realize gate-defined quantum dots as a platform of an quantum interface between single photon polarization states to single electron spin states and development accurate low-temperature nano-scale laser scanning system.

The primal motivation dedicated to (110) QDs derived on the idea to improve the efficiency of excitation for quantum state conversion using a heavy hole state. The heterostructure and QW structure on (110) substrates have a long history in spintronics and many achievements of spin physics and spin controls in low temperature transport experiments for two-dimensional systems including quantum Hall effect have been reported. In particular, in (110) QWs, many results on optical spin injection have been reported that the DP relaxation mechanism is suppressed in the (110) plane, and the spin transport behavior is dependent on the crystal orientations. Despite these intriguing spin related physics, no extensive works on realization of low dimensional transport in particular QDs in (110) GaAs two-dimensional systems have been yet demonstrated.

In this work, the first obstacle to overcome was to obtain the high quality (110) QW substrates that were capable for ballistic and coherent transport at low temperatures. In the earlier (110) QW wafers, the transports could not be measured without illumination due to low electron density in dark. However, after tremendous efforts on improving the growths in molecular beam epitaxy and optimization of the growth temperature, we could obtain a moderately high mobility two dimensional electron gas in 12-nm well width (110) GaAs/AlGaAs QWs, in which we could measure the magneto-transport at low temperature without illuminations.

Considering the experimentally and theoretically reported in-plane g-factors of electron and heavy hole for (110) plane, it has been found that a 12-nm well width (110) QW satisfies the condition of photon-spin quantum state conversion using a heavy hole state instead of a light hole state conventionally used in (001) QWs. Quantum Hall measurements provide the carrier density and mobility are 9.3×10^{10} cm^{-2} and 8.5×10^{4} cm^2/V·s, respectively. Realization of high mobility (110) GaAs/AlGaAs QWs was a significant progress.

We fabricated the DQD gate patterns, which imitate the pattern successfully used in the previous experiments on photon-spin quantum state conversion, on the (110) QWs. To perform the quantum transport measurements on the (110) GaAs QDs, we set up the newly delivered dilution refrigerator provided from Bluefors. We designed and setup the high frequency eccosorb filter and RC low pass filters on the mixing chamber plate. Finally, we performed the transport measurements for the DQDs formed in the (110) QW and could observed clear charge stability diagrams with relatively less charge noise. This is the first demonstration of zero-dimensional confinement of electrons in gate-defined QDs formed in a (110) QWs to reaching to a few electron regime to our best knowledge. Unintentional potentials probably induced by disorders and impurities in the substrate create “incidental dots”, and therefore, multiple dots rather than intended ideal DQD were accidentally formed. As external in-plane magnetic field was applied on the sample for observing the signatures of PSB from the features of the inter-dot tunneling. However, the inter-dot tunneling rate changes indicating the occurrence of PSB could not be clearly seen while the clear binary behaviors indicating the inter-dot tunneling in the real time charge sensing measurements were observed by tuning the inter-dot tunnel rate. It

seems that the existence of unintended potentials could not be sufficiently avoided.

Next, we further focused on the observation of PSB. To reduce the influence of incidental dots, which might disturb the observation of the PSB in the conventional DQD design. We employed the device design scheme that the QD sizes were reduced in design to form the QDs at the desired position without using a laterally-spreading electric field and fabricated the DQD devices. We performed the measurements of these DQDs in a dilution refrigerator at NRC, Canada. We successfully formed QDs. Although we could not completely remove incidental dots, we could reduce their effects and confirm behaviors nearly ideal DQDs. In weak tunnel coupled DQD, we could confirm the transport thorough the DQD specific to Pauli spin blockade in many electron and a few electron regimes under an external magnetic field. Furthermore, by sweeping the applied magnetic field, we observed a leakage current peak around zero magnetic filed, which can be attributed to the mixing of singlet-triplet states due to hyperfine interaction of electron spin in the QDs with nuclear spins. The electron in-plane g-factor values were estimated from a Gaussian curve fit to the leakage current peak in the inelastic transport regime. The estimated electron in-plane g-factors are almost consistent with values reported in the 12-nm width (110) QW . The estimated g-factor values were changed depending on region of the number of electrons, which was considered to be due to the difference in the confinement potential affected by unintended potential effects.

In NRC, the setup to deliver light through an optical fiber to the device in the dilution refrigerator had been already constructed. However, the capability of the optical fiber delivery system for the experiments of photon-spin quantum state conversion using gate-defined QDs had not yet verified. We performed the laser scanning experiments on the gate-defined DQDs by measuring photo-current and reflectance both at room temperature and low temperature. The QD device which showed PSB phenomena had a photo-mask with two apertures with 500-nm diameter locating above the target QDs for selective photon illumination to the QDs. We succeeded in obtaining high-resolution laser scanning images of the device by driving the xyz piezo-stages at room temperature and low temperature. We could obtain the photo-current mapping images of the apertures, indicating the laser beam transmission through the apertures. We also demonstrated that a laser beam in the

wavelength range expected for the quantum state conversion using a GaAs well substrate can be precisely delivered to the device at low temperature.

Outlook

By the construction of the experimental system for low-dimensional transport experiments and the fabrication of devices using (110)QWs, we demonstrated the formation of quantum dots in (110) QWs for the first time to our best knowledge. In addition, we observed the spin related transport useful for detecting the electron spin state. Furthermore, we have successfully demonstrated the precise delivery of light to the QD device in a dilution refrigerator using the optical fiber delivery system at NRC. We achieved a solid improvement of the fundamental technology on each aspect in order to demonstrate more efficient quantum state conversion using (110) QWs. We believe that the achievement will contribute to the future advanced experiments on quantum state conversion for verifications of basic quantum mechanical phenomena and development of quantum repeaters for quantum networks.

On the other hand, the (110) QDs is expected to give us a deep insight into the anisotropy of spin orbit interaction and spin manipulations. The QD devices measured in NRC were designed based on the spin-orbit interaction anisotropy peculiar to (110) plane as discussed in Section 4.1.1. Therefore, it is expected that EDSR and shuttle EDSR can be performed by reproducing the same design concept, and that it will lead to the exploration of new physical properties for enhancing the spin manipulation speed and preserving the spin states in the multiple (110) QDs. We believe that the our achievements will greatly contribute to efficient quantum state conversion by exciting a heavy hole state and quantum state tomography by photoexcited electron spin manipulation.

Appendix

The additional data and discussion related to this thesis are described here.

PSB Leakage Current Analysis

We estimated the electron g-factor in a few electron regime by analyzing the PSB leakage current at the (1,1) $\leftrightarrow$ (2,0) point. During sweeping the detuning gate voltage and magnetic field, telegraphic jump sometimes happened. We modified the image by shifting the data to align the resonance line straight. .

Data Modification for Detuning with Field Sweep

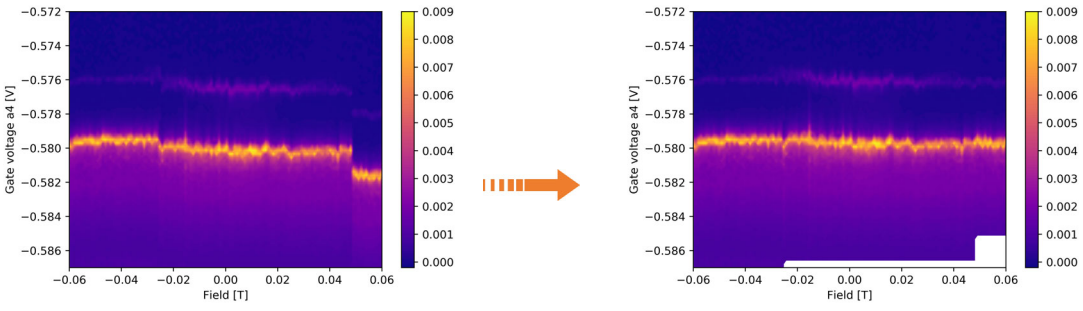

(a) Original data (b) Modified data

Fig. 7.1.1: Detuning plot for field at scan1

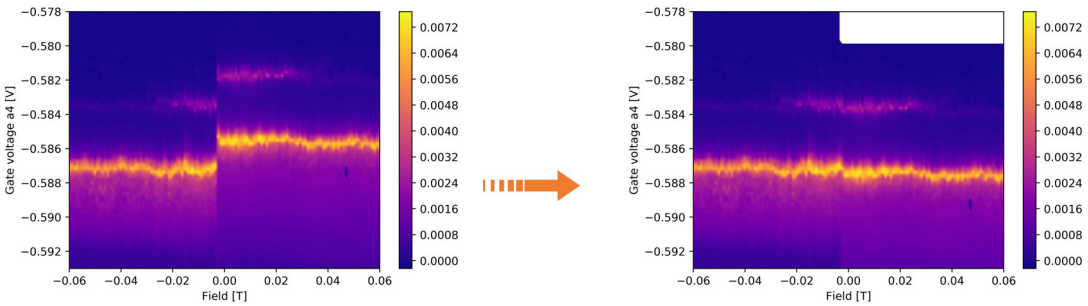

(a) Original data (b) Modified data

Fig. 7.1.2: Detuning plot for field at scan2

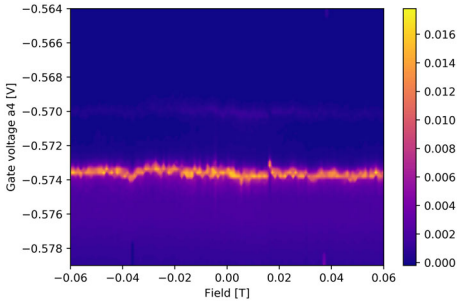

(a) Original data

(b) Detuning scan at point3

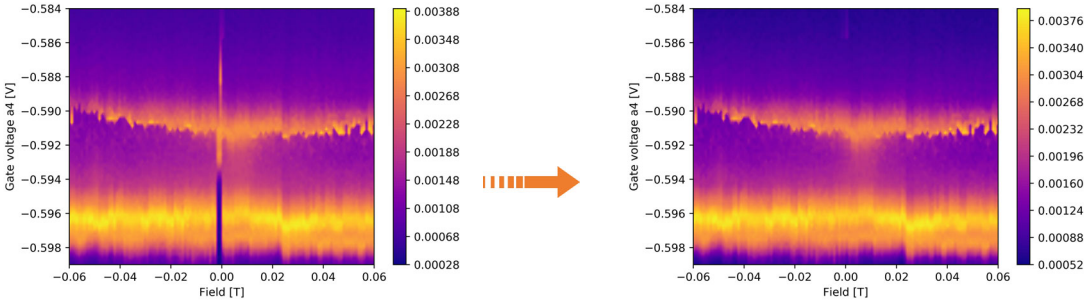

(a) Original data (b) Modified data

Fig. 7.1.4: Detuning plot for field at scan4

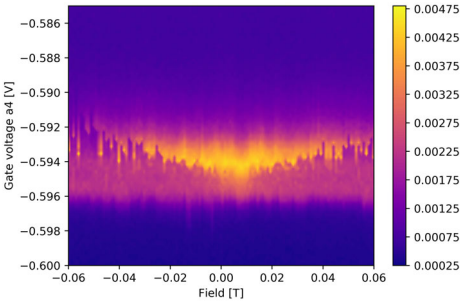

(a) Original data

(b) Detuning scan at point5

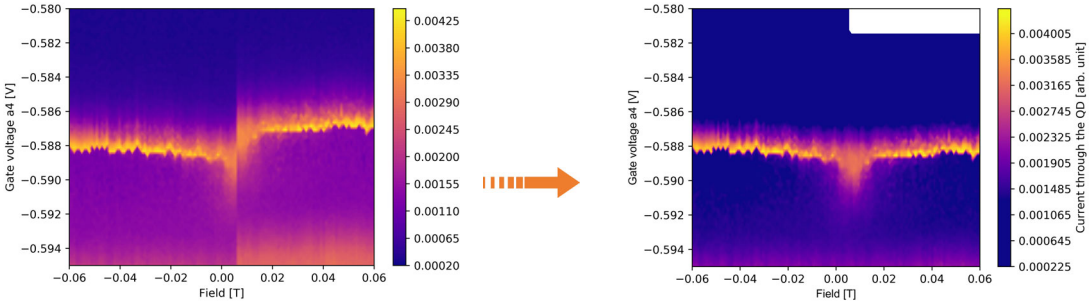

(a) Original data

(b) Modified data

Fig. 7.1.6: Detuning plot for field at scan6

(0,2) ↔ (1,1) charge transitions

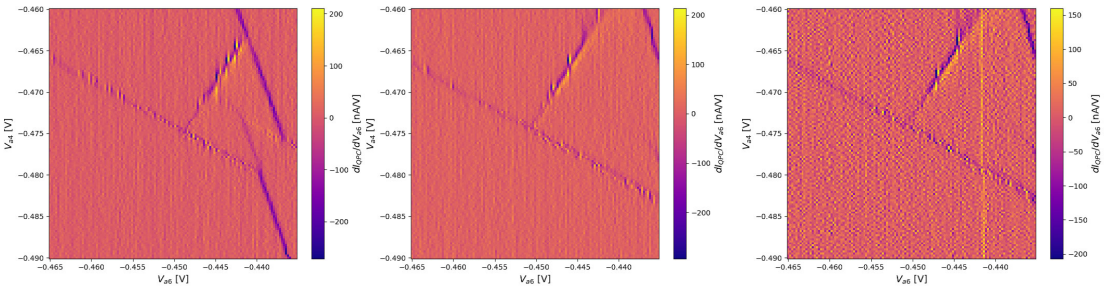

(a) V_{sd}=0.5 mV, B=0 T (b) V_{sd}=1 mV, B=0 T (c) V_{sd}=1 mV, **B=0.1 T**

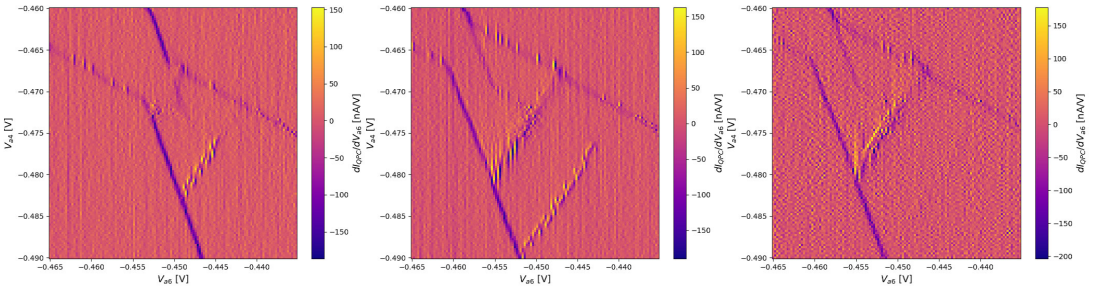

(d) V_{sd}=-0.5 mV, B=0 T (e) V_{sd}=-1 mV, B=0 T (f) V_{sd}=-1 mV, **B=0.1 T**

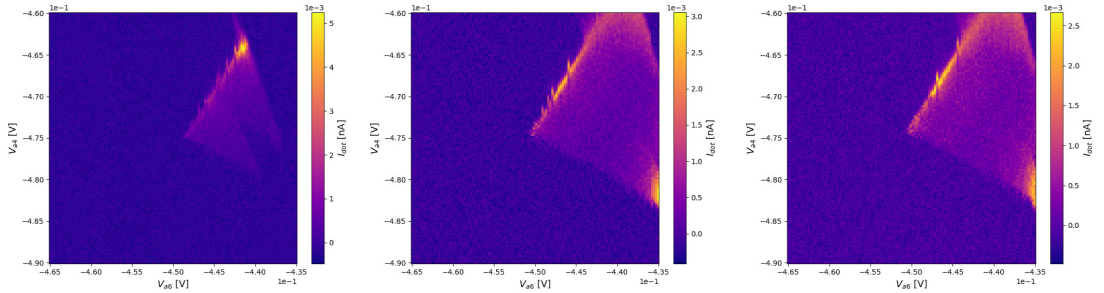

(g) V_{sd}=0.5 mV, B=0 T (h) V_{sd}=1 mV, B=0 T (i) V_{sd}=1 mV, **B=0.1 T**

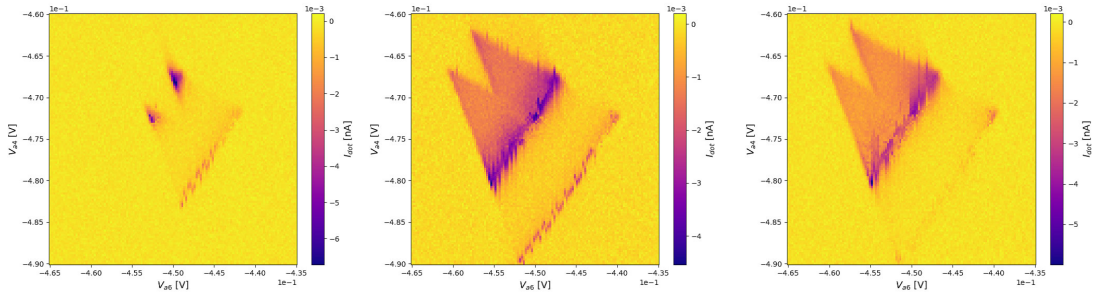

(j) V_{sd}=-0.5 mV, B=0 T (k) V_{sd}=-1 mV, B=0 T (l) V_{sd}=-1 mV, **B=0.1 T**

Fig. 7.1.7: Transport triangle plotted as dI_{QPC}/dV_{a6} and I_{dot} at (0,2) ↔ (1,1).

We observed the clear PSB behavior at the (0,2) ↔ (1,1) transition. The singlet-triplet splitting energy at (0,2) ↔ (1,1) was larger than the point of the (1,1) ↔ (2,0) transition. The dot current and the charge sensor show the bias triangle in the PSB state. The difference of singlet-triplet energy corresponds to the coupling rate between the dots.

PSB Dip Current

At the other point the (2,2) ↔ (3,1) transition, where PSB is expected, PSB leakage current showed a different behavior on magnetic filed from those observed at other transition points. The current is suppressed at zero-field, and is sharply increased at B=0.1 T in Fig. 7.1.7l, which is observed in the region bounded by green dotted rectangle.

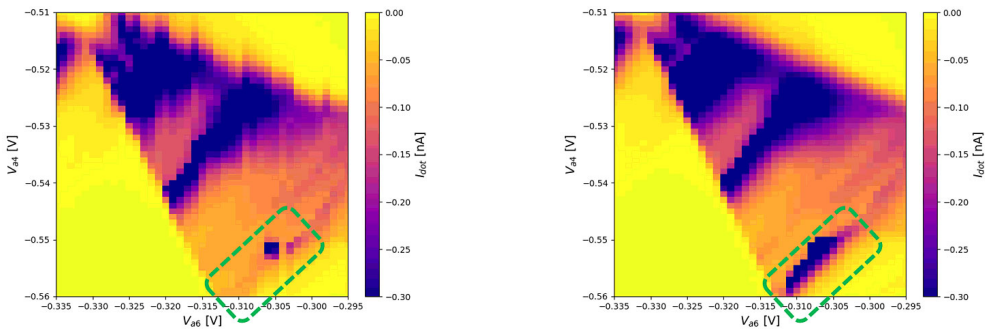

(a) B=0 T (b) B=0.1 T

Fig. 7.1.8: Dot current plotted in triangle at the (2,2) ↔ (3,1) point with a bias of -2.4 mV.

Figure 7.1.9 shows the diagram of the detuning vs. magnetic field. Gate voltage V_{a4} is swept at each field, and the field changed step by step from 0.1T. Figure 7.1.9 (c) plots the cross-sectional trace at V_{a4}=-0.556 V. Similar but small dip-like behavior of the leakage current around zero magnetic field has been reported in a strongly coupled GaAs DQD, where the tunnel coupling is larger than the nuclear spin fluctuation energy[37]. More predominant leakage current dips have been observed in InAs nanowire QDs[59, 58]. GaAs hole nanowore QDs [74], Silicon QD[80],

carbon nanotube QDs[9], and Ge hut wire hole QD[46]. However, the line shape of the dip current shown in Fig. 7.1.9 (c) does not simply match to a Lorentzian shape as theoretically predicted in terms of strong spin-orbit interaction[13]. Further experimental and theoretical understandings are needed.

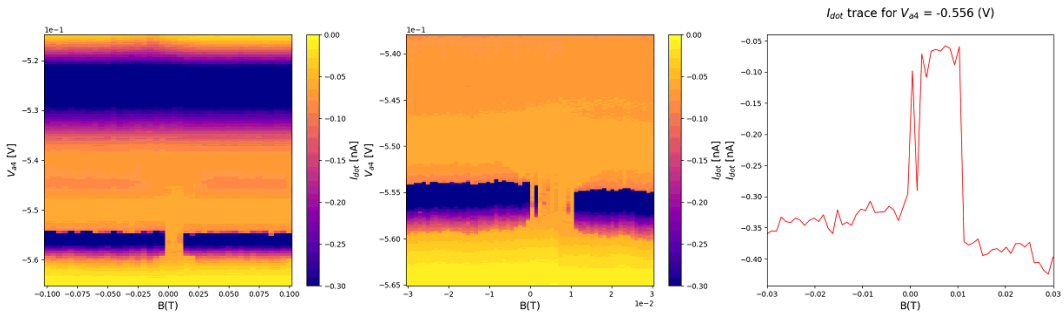

(a) V_{sd}=0.5 mV, B=0 T (b) V_{sd}=1 mV, B=0 T (c) V_{sd}=1 mV, B=0.1 T

Fig. 7.1.9: B field sweeping for the gate V_{a4} detuning.

Additionally, the current dependences on a field sweep directions at a fixed gate voltage V_{a4}=-0.556 V in the dip current region are shown in Fig. 7.1.10. The magnetic field was swept back and forth talking about 2 minutes per a way. The different current behavior depending on the sweep direction of the magnetic field is thought to reflect the polarization of the nuclear spins[37, 56].

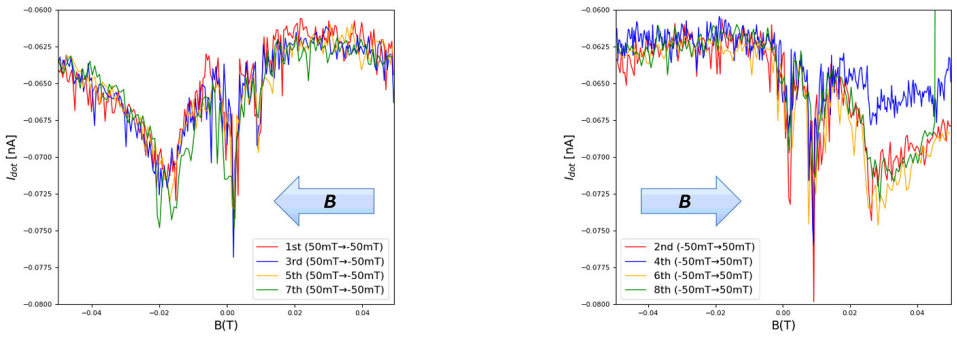

(a) B field sweep in negative direction (b) B field sweep in positive direction

Fig. 7.1.10: Current for B field sweep.

References

[1] T. Adachi, Y. Ohno, F. Matsukura, and H. Ohno. Spin relaxation in n-modulation doped GaAs/AlGaAs (110) quantum wells. *Physica E: Low-dimensional Systems and Nanostructures*, 10(1):36–39, 2001.

[2] H. Akera, H. Suzuura, and Y. Egami. Spin relaxation in a zinc-blende (110) symmetric quantum well with δ doping. *Phys. Rev. B*, 89:075314, 2014.

[3] D. E. Aspnes. Gaas lower conduction-band minima: Ordering and properties. *Phys. Rev. B*, 14:5331–5343, Dec 1976.

[4] S. Bandyopadhyay and M. Cahay. *Introduction to SPINTRONICS*. CRC Press Taylor & Francis Group, 2016.

[5] G. Bastard and R. Ferreira. Spin-flip scattering times in semiconductor quantum wells. *Surface Science*, 267(1-3):335–341, 1992.

[6] H. Bluhm, S. Foletti, I. Neder, M. Rudner, D. Mahalu, V. Umansky, and A. Yacoby. Dephasing time of GaAs electron-spin qubits coupled to a nuclear bath exceeding 200μs. *Nature Physics*, 7(2):109–113, 2011.

[7] R. S. Britton, T. Grevatt, A. Malinowski, R. T. Harley, P. Perozzo, A. R. Cameron, and A. Miller. Room temperature spin relaxation in GaAs/AlGaAs multiple quantum wells. *Applied Physics Letters*, 73(15):2140–2142, 1998.

[8] Y. S. Chen, S. Fält, W. Wegscheider, and G. Salis. Unidirectional spin-orbit interaction and spin-helix state in a (110)-oriented gaas/(al,ga)as quantum well. *Phys. Rev. B*, 90:121304, Sep 2014.

[9] H. O. H. Churchill, F. Kuemmeth, J. W. Harlow, A. J. Bestwick, E. I. Rashba, K. Flensberg, C. H. Stwertka, T. Taychatanapat, S. K. Watson, and C. M. Marcus. Relaxation and dephasing in a two-electron $^{13}\mathbf{C}$ nanotube double quantum dot. *Phys. Rev. Lett.*, 102:166802, Apr 2009.

[10] W. A. Coish and J. Baugh. Nuclear spins in nanostructures. *physica status solidi (b)*, 246(10):2203–2215, 2009.

[11] O. D. Couto, F. Iikawa, J. Rudolph, R. Hey, and P. V. Santos. Anisotropic spin transport in (110) GaAs Quantum wells. *Physical Review Letters*, 98(3):1–4, 2007.

[12] O. D. D. Couto. Acoustically induced transport in (110) GaAs quantum wells. *Fach Physik*, Dr. rer. n(September 2008):XVII, 131 S.: Ill., 2008.

[13] J. Danon and Y. V. Nazarov. Pauli spin blockade in the presence of strong spin-orbit coupling. *Phys. Rev. B*, 80:041301, Jul 2009.

[14] M. De Dios-Leyva, N. Porras-Montenegro, H. S. Brandi, and L. E. Oliveira. Electron g-factor and cyclotron effective mass in semiconductor quantum wells under growth-direction applied magnetic fields. *Brazilian Journal of Physics*, 36(3 B):854–857, 2006.

[15] M. I. D'yakonov and V. Y. Kachorovskii. Spin relaxation of two-dimensional electrons in noncentrosymmetric semiconductors. *Sov. Phys. Semicond.*, 20(July):110–112, 1986.

[16] M. I. D ' yakonov and V. I. Perel. Spin relaxation of conduction electrons in noncentrosymmetric semiconductors. *Soviet Physics*, 13:3023–3026, 1972.

[17] J. M. Elzerman, R. Hanson, J. S. Greidanus, L. H. van Beveren, S. De Franceschi, L. M. K. Vandersypen, S. Tarucha, and L. P. Kouwenhoven. Few-electron quantum dot circuit with integrated charge read out. *Phys. Rev. B*, 67(16):161308, 2003.

[18] J. Fabian and S. Das Sarma. Spin relaxation of conduction electrons. *Journal of Vacuum Science and Technology B: Microelectronics and Nanometer Structures*, 17(4):1708–1715, 1999.

[19] T. Fujita, T. A. Baart, C. Reichl, W. Wegscheider, and L. M. K. Vandersypen. Coherent shuttle of electron-spin states. *npj Quantum Information*, 3(1), 2017.

[20] T. Fujita, K. Morimoto, H. Kiyama, G. Allison, M. Larsson, A. Ludwig, S. R. Valentin, A. D. Wieck, A. Oiwa, and S. Tarucha. Angular momentum transfer from photon polarization to an electron spin in a gate-defined quantum dot. *Nature Communications*, 10(1), 2019.

[21] T. Fujita, P. Stano, G. Allison, K. Morimoto, Y. Sato, M. Larsson, J.-H. Park, A. Ludwig, A. D. Wieck, A. Oiwa, and S. Tarucha. Signatures of Hyperfine, Spin-Orbit, and Decoherence Effects in a Pauli Spin Blockade. *Physical Review Letters*, 117(20):206802, nov 2016.

[22] C. Gradl, M. Kempf, D. Schuh, D. Bougeard, R. Winkler, C. Schüller, and T. Korn. Hole-spin dynamics and hole g-factor anisotropy in coupled quantum well systems. *Phys. Rev. B*, 90:165439, Oct 2014.

[23] C. Gradl, R. Winkler, M. Kempf, J. Holler, D. Schuh, D. Bougeard, A. Hernández-Mínguez, K. Biermann, P. V. Santos, C. Schüller, and T. Korn. Asymmetric g Tensor in Low-Symmetry Two-Dimensional Hole Systems. *Physical Review X*, 8(2):21068, 2018.

[24] K. H, A. A. Kiselev, F. A. Baron, K. W. Kim, E. Yavlonovich, H. Kosaka, A. A. Kiselev, F. A. Baron, Ki Wook Kim, and E. Yablonovitch. Electron g factor engineering in IlI-V semiconductors for quantum communications. *Electronics Letters*, 37(7):464–465, 2001.

[25] M. B. P. H. C. Casey Jr. *Heterostructure lasers: Part A - Materials and operating characteristics.* Academic Press, 1978.

[26] M. B. P. H. C. Casey Jr. *Heterostructure lasers: Part B - Materials and operating characteristics.* Academic Press, 1978.

[27] R. Hanson, L. P. Kouwenhoven, J. R. Petta, S. Tarucha, and L. M. K. Vandersypen. Spins in few-electron quantum dots. *Reviews of Modern Physics*, 79(4):1217–1265, 2007.

[28] A. Hernández-Mínguez, K. Biermann, R. Hey, and P. V. Santos. Spin transport and spin manipulation in GaAs (110) and (111) quantum wells. *Physica Status Solidi (B) Basic Research*, 251(9):1736–1752, 2014.

[29] J. Hübner, S. Kunz, S. Oertel, D. Schuh, M. Pochwała, H. T. Duc, J. Förstner, T. Meier, and M. Oestreich. Electron g-factor anisotropy in symmetric (110)-oriented GaAs quantum wells. *Physical Review B - Condensed Matter and Materials Physics*, 84(4):2–5, 2011.

[30] S. Iba, H. Saito, K. Watanabe, Y. Ohno, and S. Yuasa. Systematic study of surface morphology, photoluminescence efficiency, and spin-detection sensitivity in (110)-oriented GaAs/AlGaAs quantum wells. *Japanese Journal of Applied Physics*, 55(11), 2016.

[31] A. C. Johnson, J. R. Petta, C. M. Marcus, M. P. Hanson, and A. C. Gossard. Singlet-triplet spin blockade and charge sensing in a few-electron double quantum dot. *Physical Review B*, 72(16):165308, oct 2005.

[32] A. C. Johnson, J. R. Petta, J. M. Taylor, A. Yacoby, M. D. Lukin, C. M. Marcus, M. P. Hanson, and A. C. Gossard. Triplet-singlet spin relaxation via nuclei in a double quantum dot. *Nature*, 435(7044):925–928, 2005.

[33] S. Katsumoto. Lecture on fundamental solid state physics: Electron transport and electronic states of quantum dot systems (part 1). *SOLID STATE PHYSICS*, 44(10), 2009.

[34] S. Katsumoto. Lecture on fundamental solid state physics: Electron transport and electronic states of quantum dot systems (part 2). *SOLID STATE PHYSICS*, 45(5), 2010.

[35] A. A. Kiselev, K. W. Kim, and E. Yablonovitch. In-plane light-hole g factor in strained cubic heterostructures. *Phys. Rev. B*, 64:125303, Sep 2001.

[36] F. H. L. Koppens, C. Buizert, K. J. Tielrooij, I. T. Vink, K. C. Nowack, T. Meunier, L. P. Kouwenhoven, and L. M. K. Vandersypen. Driven coherent oscillations of a single electron spin in a quantum dot. *Nature*, 442(7104):766–771, 2006.

[37] F. H. L. Koppens, J. A. Folk, J. M. Elzerman, R. Hanson, L. H. W. van Beveren, I. T. Vink, H. P. Tranitz, W. Wegscheider, L. P. Kouwenhoven, and L. M. K. Vandersypen. Control and detection of singlet-triplet mixing in a random nuclear field. *Science*, 309(5739):1346–1350, 2005.

[38] H. Kosaka, T. Inagaki, Y. Rikitake, H. Imamura, Y. Mitsumori, and K. Edamatsu. Spin state tomography of optically injected electrons in a semiconductor. *Nature*, 457(7230):702–705, 2009.

[39] H. Kosaka, H. Shigyou, Y. Mitsumori, Y. Rikitake, H. Imamura, T. Kutsuwa, K. Arai, and K. Edamatsu. Coherent Transfer of Light Polarization to Electron Spins in a Semiconductor. *Physical Review Letters*, 100(9):096602, 2008.

[40] H. Kosaka, H. Shigyou, Y. Mitsumori, Y. Rikitake, H. Imamura, T. Kutsuwa, K. Arai, and K. Edamatsu. Coherent transfer of light polarization to electron spins in a semiconductor. *Phys. Rev. Lett.*, 100:096602, Mar 2008.

[41] K. Kuroyama, M. Larsson, C. Y. Chang, J. Muramoto, K. Heya, T. Fujita, G. Allison, S. R. Valentin, A. Ludwig, A. D. Wieck, S. Matsuo, A. Oiwa, and S. Tarucha. Photogeneration of a single electron from a single Zeeman-resolved light-hole exciton with preserved angular momentum. *Physical Review B*, 99(8):1–5, 2019.

[42] T. Kutsuwa, K. Arai, H. Shigyo, H. Kinjo, K. Ono, Y. Mitsumori, H. Kosaka, and K. Edamatsu. Single photon response in GaAs quantum transport devices for photon-spin quantum state transfer. *Physica Status Solidi (C) Current Topics in Solid State Physics*, 3(12):4326–4329, 2006.

[43] R. T. L. Esaki. Superlattice and negative differential conductivity in semiconductors. *IBM Journal of Research and Development*, 14, 1970.

[44] N. S. Lai, W. H. Lim, C. H. Yang, F. A. Zwanenburg, W. A. Coish, F. Qassemi, A. Morello, and A. S. Dzurak. Pauli spin blockade in a highly tunable silicon double quantum dot. *Scientific Reports*, 1(1):110, 2011.

[45] M. Levinstein, M. Levinstein, S. Rumyantsev, and M. Shur. Nsm archive - aluminium gallium arsenide (algaas) - band structure and carrier concentration.

[46] H. Liu, T. Zhang, K. Wang, F. Gao, G. Xu, X. Zhang, S.-X. Li, G. Cao, T. Wang, J. Zhang, X. Hu, H.-O. Li, and G.-P. Guo. Gate-tunable spin-orbit coupling in a germanium hole double quantum dot. *Phys. Rev. Appl.*, 17:044052, Apr 2022.

[47] V. F. Maisi, A. Hofmann, M. Röösli, J. Basset, C. Reichl, W. Wegscheider, T. Ihn, and K. Ensslin. Spin-orbit coupling at the level of a single electron. *Phys. Rev. Lett.*, 116:136803, Mar 2016.

[48] A. Malinowski, R. S. Britton, T. Grevatt, R. T. Harley, D. A. Ritchie, and M. Y. Simmons. Spin relaxation in GaAs/AlxGa1-xAs quantum wells. *Phys. Rev. B*, 62(19):13034–13039, 2000.

[49] K. Morimoto, T. Fujita, G. Allison, S. Teraoka, M. Larsson, H. Kiyama, S. Haffouz, D. G. Austing, A. Ludwig, A. D. Wieck, A. Oiwa, and S. Tarucha. Single photoelectron detection after selective excitation of electron heavy-hole and electron light-hole pairs in double quantum dots. *Physical Review B - Condensed Matter and Materials Physics*, 90(8):2–6, 2014.

[50] G. M. Müller, M. Römer, D. Schuh, W. Wegscheider, J. Hübner, and M. Oestreich. Spin Noise Spectroscopy in GaAs (110) Quantum Wells: Access to Intrinsic Spin Lifetimes and Equilibrium Electron Dynamics. *Physical Review Letters*, 101(20):206601, nov 2008.

[51] T. Nakagawa, S. Lamoureux, T. Fujita, J. Ritzmann, A. Ludwig, A. D. Wieck, A. Oiwa, M. Korkusinski, A. Sachrajda, D. G. Austing, and L. Gaudreau. Electron g-factor determined for quantum dot circuit fabricated from (110)-oriented gaas quantum well. *Journal of Applied Physics*, 131(13):134305, 2022.

[52] K. T. Nguyen, M. P. Lilly, E. Nielsen, N. Bishop, R. Rahman, R. Young, J. Wendt, J. Dominguez, T. Pluym, J. Stevens, T. M. Lu, R. Muller, and M. S. Carroll. Charge sensed Pauli blockade in a metal-oxide-semiconductor lateral double quantum dot. *Nano Letters*, 13(12):5785–5790, 2013.

[53] K. C. Nowack, F. H. L. Koppens, Y. V. Nazarov, and L. M. K. Vandersypen. Coherent control of a single electron spin with electric fields. *Science*, 318(5855):1430–1433, 2007.

[54] Y. Ohno, R. Terauchi, T. Adachi, F. Matsukura, and H. Ohno. Spin Relaxation in GaAs(110) Quantum Wells. *Phys. Rev. Lett.*, 83(20):4196–4199, 1999.

[55] K. Ono, D. G. Austing, Y. Tokura, and S. Tarucha. Current rectification by Pauli exclusion in a weakly coupled double quantum dot system. *Science*, 297(5585):1313–1317, 2002.

[56] K. Ono and S. Tarucha. Nuclear-spin-induced oscillatory current in spin-blockaded quantum dots. *Phys. Rev. Lett.*, 92:256803, Jun 2004.

[57] T. Otsuka, T. Nakajima, M. R. Delbecq, S. Amaha, J. Yoneda, K. Takeda, G. Allison, T. Ito, R. Sugawara, A. Noiri, A. Ludwig, A. D. Wieck, and S. Tarucha. Single-electron Spin Resonance in a Quadruple Quantum Dot. *Scientific Reports*, 6(31820):1–6, 2016.

[58] A. Pfund, I. Shorubalko, K. Ensslin, and R. Leturcq. Spin-state mixing in inas double quantum dots. *Phys. Rev. B*, 76:161308, Oct 2007.

[59] A. Pfund, I. Shorubalko, K. Ensslin, and R. Leturcq. Suppression of spin relaxation in an inas nanowire double quantum dot. *Phys. Rev. Lett.*, 99:036801, Jul 2007.

[60] Y. Rikitake, H. Imamura, and H. Kosaka. Effect of the electron-hole exchange interaction on the photon-spin quantum state transfer. *AIP Conference Proceedings*, 893:1103–1104, 2007.

[61] J. S. Sandhu, A. P. Heberle, J. J. Baumberg, and J. R. A. Cleaver. Gateable Suppression of Spin Relaxation in Semiconductors. *Phys. Rev. Lett.*, 86(10):2150–2153, 2001.

[62] E. F. Schubert. *Doping in III-V Semiconductors*. Cambridge Studies in Semiconductor Physics and Microelectronic Engineering. Cambridge University Press, 2005.

[63] E. F. Schubert. *Light-Emitting Diodes*. Cambridge University Press, 2 edition, 2006.

[64] F. Sedgwick, S. Crankshaw, M. Moewe, C. J. Chang-Hasnain, H. Wang, and S.-L. Chuang. Electron spin coherence in (110) gaas quantum well waveguides. In *Conference on Lasers and Electro-Optics/Quantum Electronics and Laser Science Conference and Photonic Applications Systems Technologies*, page QME7. Optica Publishing Group, 2006.

[65] A. V. Shchepetilnikov, Y. A. Nefyodov, I. V. Kukushkin, and W. Dietsche. Electron g-factor in gaas/algaas quantum wells of different width and barrier al concentrations. *Journal of Physics: Conference Series*, 456(1):012035, aug 2013.

[66] E. Y. Sherman. Random spin orbit coupling and spin relaxation in symmetric quantum wells. *Applied Physics Letters*, 82(2):209–211, jan 2003.

[67] Y. S. Shin, T. Obata, M. Pioro-Ladrière, Y. Tokura, R. Brunner, T. Kubo, K. Yoshida, and S. Tarucha. Single electron spin addressing by using photon-assisted-tunneling in a double quantum dot including a micro-magnet. *Physica E: Low-Dimensional Systems and Nanostructures*, 42(4):825–829, 2010.

[68] A. Shlykevich, T. Bystricky, and T. Blecha. High frequency properties of RF planar passive components. *Periodica polytechnica Electrical engineering and computer science*, 61(1):48–53, 2017.

[69] A. Tackeuchi, Y. Nishikawa, and O. Wada. Room-temperature electron spin dynamics in GaAs/AlGaAs quantum wells. *Applied Physics Letters*, 68(6):797–799, feb 1996.

[70] J. M. Taylor, J. R. Petta, A. C. Johnson, A. Yacoby, C. M. Marcus, and M. D. Lukin. Relaxation, dephasing, and quantum control of electron spins in double quantum dots. *Phys. Rev. B*, 76:035315, Jul 2007.

[71] W. G. van der Wiel, S. De Franceschi, J. M. Elzerman, T. Fujisawa, S. Tarucha, L. P. Kouwenhoven, S. Toné, T. Kubo, T. Ohyama, T. Kusakabe, and Y. Minatogawa. Electron transport through double quantum dots. *Rev. Mod. Phys.*, 75(1):1–22, 2002.

[72] R. Völkl, M. Schwemmer, M. Griesbeck, S. A. Tarasenko, D. Schuh, W. Wegscheider, C. Schüller, and T. Korn. Spin polarization, dephasing, and photoinduced spin diffusion in (110)-grown two-dimensional electron systems. *Physical Review B - Condensed Matter and Materials Physics*, 89(7):1–9, 2014.

[73] R. Vrijen and E. Yablonovitch. A spin-coherent semiconductor photo-detector for quantum communication. *Physica E: Low-Dimensional Systems and Nanostructures*, 10(4):569–575, 2001.

[74] D. Q. Wang, O. Klochan, J. T. Hung, D. Culcer, I. Farrer, D. A. Ritchie, and A. R. Hamilton. Anisotropic Pauli Spin Blockade of Holes in a GaAs Double Quantum Dot. *Nano Letters*, 16(12):7685–7689, 2016.

[75] K. Wang, H. O. Li, M. Xiao, G. Cao, and G. P. Guo. Spin manipulation in semiconductor quantum dots qubit. *Chinese Physics B*, 27(9), 2018.

[76] X. R. Wang, Y. S. Zheng, and S. Yin. Spin relaxation and decoherence of two-level systems. *Physical Review B - Condensed Matter and Materials Physics*, 72(12):1–4, 2005.

[77] R. Winkler and A. Nesvizhskii. Anisotropic hole subband states and interband optical absorption in [mmn]-oriented quantum wells. *Physical Review B - Condensed Matter and Materials Physics*, 53(15):9984–9992, 1996.

[78] R. Winkler, S. J. Papadakis, E. P. De Poortere, and M. Shayegan. Highly anisotropic g-factor of two-dimensional hole systems. *Physical Review Letters*, 85(21):4574–4577, 2000.

[79] M. Wu, J. Jiang, and M. Weng. Spin dynamics in semiconductors. *Physics Reports*, 493(2-4):61–236, aug 2010.

[80] G. Yamahata, T. Kodera, H. O. Churchill, K. Uchida, C. M. Marcus, and S. Oda. Magnetic field dependence of Pauli spin blockade: A window into the sources of spin relaxation in silicon quantum dots. *Physical Review B - Condensed Matter and Materials Physics*, 86(11):1–5, 2012.

[81] N. Yokota. *Studies on Relaxation and Transport of Electron Spins for Spin-Controlled Photonic Devices*. PhD thesis, Nara Institute of Science and Technology, 2013.

[82] A. You, M. A. Y. Be, I. In, A. Tackeuchi, O. Wada, and Y. Nishikawa. Electron spin relaxation in InGaAs/InP multiple-quantum wells. *Applied Physics Letters*, 70(9):1131–1133, 1997.